

STUDY OF VERTICAL COUPLED-CAVITY LASER STRUCTURES

THÈSE N° 3118 (2004)

PRÉSENTÉE À LA FACULTÉ SCIENCES DE BASE

Institut de photonique et d'électronique quantiques

SECTION DE PHYSIQUE

ÉCOLE POLYTECHNIQUE FÉDÉRALE DE LAUSANNE

POUR L'OBTENTION DU GRADE DE DOCTEUR ÈS SCIENCES

PAR

Vlad BADILITA

DEA en physique, Université de Bucarest, Roumanie
et de nationalité roumaine

acceptée sur proposition du jury:

Prof. M. Illegems, directeur de thèse
Dr J.-F. Carlin, rapporteur
Prof. A. Fiore, rapporteur
Prof. K. Panajotov rapporteur
Dr R. Stanley, rapporteur

Lausanne, EPFL
2004

Abstract

This thesis addresses general aspects of the operation of a coupled-cavity vertical surface-emitting laser (CC-VCSEL) which consists of two active cavities optically coupled and independently electrically pumped.

The first two chapters of the thesis deal with a general introduction to the VCSEL field, including some historical aspects and a summary of the theory of semiconductor lasers. We also provide with an introduction in the theory of semiconductor lasers with special emphasis on VCSELs.

In the following three chapters we present our experimental characterization results on CC-VCSELs and their theoretical interpretation. Two models are developed which together provide a powerful toolbox for the design and characterization of CC-VCSELs. The **lumped-mirror model** has as a starting point only the optical characteristics of the CC-VCSEL structure. Considering these input parameters, i.e. the reflectivity of the coupling mirror and the detuning between the two cavities, the model provides two important results: the position of the resonant modes of the structure and the confinement coefficients that characterize the degree of localization of each mode in each cavity respectively. The lumped-mirror model is a reliable way to determine these parameters, which are specific to coupled-cavity VCSELs, as these results are in a good agreement with the ones provided by the well-established calculation procedure based on the matrix transfer method.

The **rate-equation model** completes the previously exposed lumped-mirror model considering also the electrical injection, independent for each cavity. The operation of the coupled-cavity device is described starting from simple, intuitive arguments, developing the rate-equations for both the number of carriers in each cavity, and the number of photons in each of the two optical modes. Analyzing the resulting system in steady-state conditions, we identify the different working regimes of the device, in an excellent agreement with the experimental data. We introduce a notion specific to the CC-VCSEL, i.e. the “double-threshold point” where both optical modes start lasing. In analogy with the classical one-cavity device, we show that, in the case of the CC-VCSEL, the complete clamping of carrier densities and gain coefficients takes place only in the regime where the device emits two modes simultaneously, i.e. the “dual-wavelength lasing mode”, while in the regime where the device lases on only one mode, i.e. the “single-wavelength lasing mode”, the carrier densities in the two cavities, and consequently the gain coefficients, may vary, the only constraint being the need to satisfy the threshold equation for the corresponding lasing mode.

In the characterization of the CC-VCSEL, we also address the polarization behavior under special bias conditions. We investigate the state of polarization of the light emitted from the top cavity under direct bias while the bottom cavity is reverse biased. Also, the effect of the reverse bias of one cavity on the light output from the other cavity is examined. For this purpose, the quantum confined Stark effect is evaluated and we show how the modification of the absorption as a result of the reverse applied electric field is integrated in the rate-equation model.

The field of multisection optoelectronic devices is already well-established if we refer to edge-emitting lasers (EELs) where new functionalities and performance improvements have been achieved by using the concept of multicavity devices. At present, the application of these concepts to multicavity VCSELs as described in this work is just emerging but should prove equally interesting and challenging.

The coupled-cavity VCSEL structure not only exhibits an interesting and rich physics making it interesting from the academic point of view, but we believe that CC-VCSELs capable of wavelength selection and/or wavelength tuning will be indispensable component for the emerging dense wavelength multiplexing data communication systems, while an emerging application of polarization switching is the data routing in optical data communication systems, therefore attributing to the CC-VCSEL device an important role in the photonics revolution.

Version abrégée

Cette thèse présente les aspects généraux du fonctionnement d'un laser à cavités verticales couplées (CC-VCSEL). Ce type de laser à cavité verticale (VCSEL) comprend deux cavités actives couplées optiquement, chacune d'elles étant pompée électriquement et de manière indépendante.

Les deux premiers chapitres du mémoire sont une introduction générale aux VCSELs, incluant des aspects historiques et un résumé bref de la théorie des lasers à semi-conducteurs mettant en avant les particularités des VCSELs.

Les trois chapitres suivants présentent des mesures expérimentales sur des CC-VCSELs avec leur interprétation théorique. Nous avons développé deux modèles complémentaires qui fournissent un ensemble d'outils bien adaptés pour la conception et la caractérisation de CC-VCSELs. Le **modèle des miroirs virtuels** décrit les caractéristiques purement optiques d'une structure CC-VCSEL. A partir de deux valeurs d'entrée, à savoir la réflectivité du miroir de couplage et l'écart d'épaisseur entre les cavités, ce modèle calcule deux paramètres importants : la longueur d'onde des modes résonants dans la structure et les coefficients de confinement qui évaluent les degrés de localisation de chaque mode dans chaque cavité. Le modèle des miroirs virtuels est fiable pour déterminer ces paramètres qui sont spécifiques aux VCSEL à cavités couplées. Ses prédictions sont en accord avec celles qui sont obtenues par les méthodes bien établies basées sur la technique des matrices de transfert.

Le **modèle des équations de bilan** complète celui des miroirs virtuels, et prend en compte l'injection électrique, indépendante pour chaque cavité. Le fonctionnement du VCSEL à cavités couplées est décrit à partir d'arguments simples et intuitifs, en écrivant des équations de bilan pour le nombre des porteurs dans chaque cavité et pour le nombre des photons pour chaque mode optique. En analysant le système résultant dans des conditions stationnaires, on identifie les différents régimes de fonctionnement du composant, ceci en très bon accord avec les données expérimentales. Nous introduisons une notion spécifique au CC-VCSEL: le «point de double seuil» pour lequel les deux modes optiques commencent à laser. En comparaison avec le comportement d'un laser classique, nous montrons que dans le cas d'un CC-VCSEL le verrouillage des densités de porteurs et des gains n'a lieu que dans un régime où le dispositif émet deux longueurs d'onde en même temps, le régime d'«émission stimulée double». Par contre, quand le dispositif émet une seule longueur d'onde, dans un régime d'«émission stimulée unique», les densités de porteurs et les gains peuvent varier, mais de manière non indépendante, la contrainte étant qu'une équation de seuil soit satisfaite.

Nous avons aussi observé expérimentalement que certains régimes d'injection électrique affectent l'état de polarisation de la lumière émise par les CC-VCSELs. Un changement de polarisation a lieu lorsque le courant est injecté en direct dans la diode de la cavité supérieure et qu'une tension en inverse est appliquée sur la diode inférieure. L'effet d'une tension en inverse n'étant pas prise en compte par les modèles précédents, nous nous penchons sur ce cas. Nous évaluons en particulier l'effet Stark quantique et montrons comment intégrer une variation d'absorption due au champ électrique appliqué en inverse dans le modèle des équations de bilan.

Le domaine des dispositifs optoélectroniques à sections multiples est déjà bien établi dans le cadre des lasers à émission latérale, où ce type de conception permet des fonctions nouvelles et des performances accrues. L'application de ce concept aux VCSELs à cavités multiples, comme nous l'avons abordé dans ce travail, n'en est encore qu'à ses débuts, mais on peut prévoir des applications tout aussi intéressantes.

L'intérêt dans les VCSELs à cavités couplées n'est pas seulement académique et dû à la richesse de la physique mise en oeuvre. Les CC-VCSELs ont un potentiel pratique dans le domaine des systèmes de communication optique, pour la sélection et le réglage des longueurs d'onde dans les systèmes optiques multiplexés en longueur d'onde, ainsi que pour le routage et la commutation de données codées par polarisation.

Contents

Abstract	3
Version abrégée	5
1. VCSELs – a history	9
1.1. Historical overview	9
1.2. General VCSEL structure	11
1.3. Optical cavity and mirrors	13
1.4. Gain region	16
1.5. The choice VCSEL design	18
1.6. VCSELs for wavelength engineering	23
Bibliography CHAPTER 1	25
2. VCSELs – theory of operation	29
2.1. Introduction	29
2.2. Energy levels and bands in solids	30
2.3. Spontaneous and stimulated transitions: the creation of light	31
2.4. Confinement of carriers and photons in diode lasers	38
2.5. Carrier generation and recombination in active regions	40
2.6. Photon generation and loss in laser cavities	43
2.7. Threshold or steady-state gain in lasers	45
2.8. Relative confinement factor	48
2.9. Distributed Bragg reflectors	50
Bibliography CHAPTER 2	52

3.	The coupled-cavity VCSEL (CC-VCSEL)	53
3.1.	State of the art of CC-VCSELs	53
3.2.	Device structure and operating principles	58
3.3.	CC-VCSEL processing	59
3.4.	The lumped-mirror model	60
3.5.	Results of the lumped-mirror model	64
3.6.	Design of the CC-VCSEL structures	67
3.7.	Conclusions	71
	Bibliography CHAPTER 3	71
4.	Rate-equation model for CC-VCSELs	73
4.1.	Rate equations – general form	73
4.2.	Solutions for different operating regimes	75
4.3.	Experiment and theory – comparison	82
4.4.	CC-VCSEL behavior for high-injection currents	90
4.5.	Conclusions	91
	Bibliography CHAPTER 4	92
5.	Polarization switching in CC-VCSELs	93
5.1.	Introduction: Experimental data on PS in VCSELs	93
5.2.	Different approaches to explain PS in VCSELs	98
5.3.	Designs for polarization stabilization and control in VCSELs	106
5.4.	Control of polarization switching in CC-VCSEL	111
5.5.	Conclusions	118
	Bibliography CHAPTER 5	118
6.	Conclusions	121
	Appendix A	125
	Appendix B	129
	Acknowledgements	137
	Curriculum vitae	139

Chapter 1

VCSELs – a history

1.1 Historical overview

The first semiconductor p-n junction laser was reported in early sixties (1962) [1] and continuous improvements have been achieved since then, significantly increasing the performances. These first lasers consisting of a single p-n junction were operated only at low temperatures and very high current densities, due to the lack of optical and electrical confinement. A major advance was realised in 1969-1970 with the development of the double heterojunction laser allowing reaching room temperature operation for the first time. The basic device structure of the edge-emitting laser (EEL) has since remained unchanged. Typically, there is a waveguide formed to guide light parallel to the surface. This waveguide is defined vertically by epitaxial growth, and laterally by etching and/or regrowth. The bandgap of the waveguide is lower than that of the adjoining regions, providing simultaneously electrical and optical confinement. Cleaved facets then form the laser cavity, and light is emitted from the edge of the chip. Usually facet coatings are required for reliability and testing must be done at the individual chip level. This is basically the structure of edge-emitting lasers and this type of structure limits the possibilities of integration onto chip since the mirrors must be individually cleaved or, alternatively, defined by facet etching. Another limitation is that only one-dimensional (1D) arrays may be formed with these structures.

Surface-emitting lasers (SEL) overcome these limitations by extracting the light perpendicular to the wafer surface. With such a laser, testing is possible at the wafer level with a considerable simplification of the testing process. SELs naturally lend themselves for two-dimensional arrays enabling applications for optical interconnections. Basically, there are two ways to achieve a SEL: form a normal in-plane laser and deflect the light up with a mirror or a grating, or turn the active cavity 90° so that the cavity is vertical and the mirrors are parallel to the wafer surface. This last geometry corresponds to the structure of a vertical-cavity SEL or VCSEL. VCSELs, using the cavity configuration described above, totally different from the traditional cleaved cavity, exhibit high-coupling efficiencies in single-mode optical fibres, and have progressed significantly owing to

continuous refinements in epitaxial technologies. Advances in cavity schemes for frequency control and linewidth reduction have yielded lasers with extremely low (kHz) linewidths and wide tuning ranges. Many of these recent developments have been driven by the information revolution requiring dense arrays of high-speed, low-power diode lasers serving as light sources in computer data links or other mass-information transmission systems.

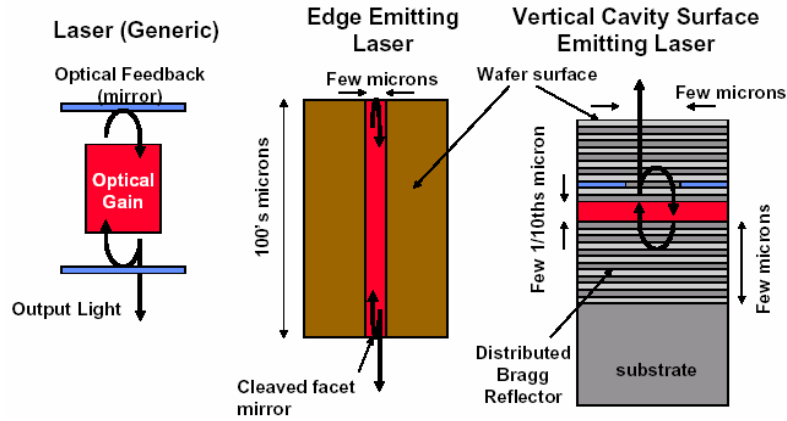


Figure 1.1: A laser needs a cavity with optical gain, delimited by two mirrors that assure the optical feedback; EELs vs. VCSELS.

The possibility to realise such a device was suggested in 1979 by Iga [2] and Soda et al. [3] pioneered this revolutionary approach in 1979. Initial devices had metallic mirrors and operated at very high currents (900 mA threshold current) at liquid nitrogen temperatures (77 K) under pulsed conditions. Slow improvements have been made in the next decade with the same group pursuing the possibility of VCSELS in the GaInAsP/InP and AlGaAs/GaAs materials systems. The real boom took place when VCSELS took advantage of advances in epitaxial growth techniques of molecular-beam epitaxy (MBE) and metal-organic chemical-vapour deposition (MOCVD). These techniques drastically improved the characteristics of the mirrors and it is due to the apparition of the distributed Bragg reflectors (DBRs) [4] providing high reflectivity and low absorption, that continuous-wave (CW), room-temperature (RT) operation has been achieved at low threshold currents. The first RT pulse operated VCSEL with GaAs active region was demonstrated in 1984 [5]. The threshold current density of the initial surface-emitting lasers was rather high in comparison with conventional stripe lasers due to the short gain path because of the poor reflectivity of the mirrors. This prevented RT e CW operation until 1988 [6,7]. Since then rapid progress has been made resulting in a decrease in RT cw threshold current from 32 to $\approx 10^{-1}$ mA [8]. New gain materials – InGaAs QWs – have been introduced and a systematic study of such a VCSEL was undertaken starting in 1991 in Coldren’s group [9]. Further improvements in VCSELS’ technology such as the introduction of Al oxide confinement [10] have led to even lower threshold values [11] and high-frequency modulation [12].

As any other laser, a VCSEL (Figure 1.1) should have a resonant cavity with a region of optical gain and two mirrors that delimitate the cavity and assure the optical feedback. In this chapter

each element will be described from the point of view of VCSELs design and performances. Basic device properties and generally applicable cavity design rules are introduced.

This chapter is intended to provide the basic knowledge necessary to understand VCSELs' benefits and limitations and at the same time to give an overview of some state-of-the-art performance data obtained experimentally. We start with basic studies of the laser cavity, such as active region and reflector properties, where essential differences to edge-emitting laser operation are underlined.

1.2 General VCSEL structure

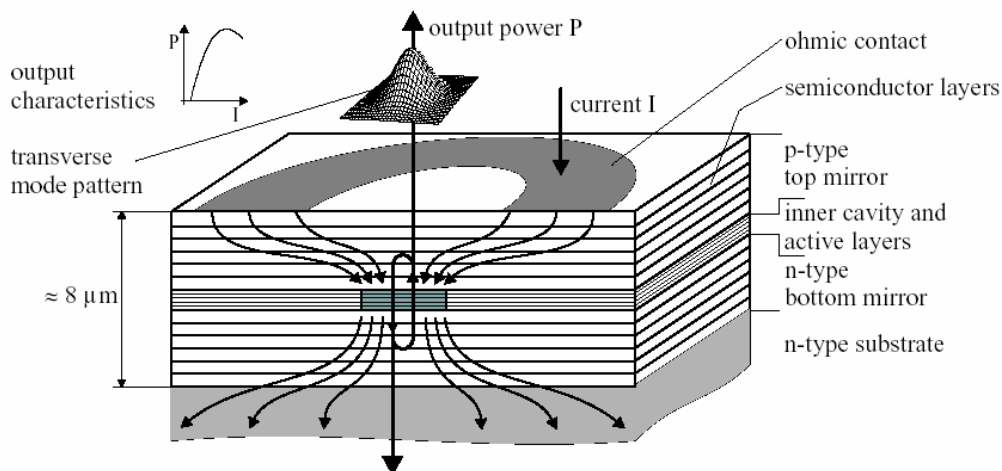


Figure 1.2: General VCSEL layer structure [13].

Figure 1.2 illustrates the typical layout of a VCSEL. The inner cavity containing the amplifying layers is surrounded by electrically conductive layer stacks that form the laser mirrors which provide optical feedback. GaAs/AlGaAs VCSELs require about $8 \mu\text{m}$ of epitaxially grown material, whereas the active region is composed of just a few quantum wells (QWs) of a few nanometer thickness each. The p-i-n type doping configuration is similar to conventional edge-emitting lasers (EELs). In the most simple device layouts, electric current is injected from ohmic contacts on the top epitaxial side and on the backside of the substrate. Several methods have been successfully employed to achieve current confinement to a predefined active area. These methods will be discussed later on in this chapter.

One of the main advantages of a VCSEL is that due to its short cavity length – typically of the order of magnitude of the resonant wavelength – the longitudinal cavity mode spacing is very large. Actually it is possible to have the mode spacing larger than the gain bandwidth of the active material. This is clearly shown in Figure 1.3 where for the EEL there are a few modes favoured by the gain curve while in the VCSEL there is only a single mode within the gain region due to higher free spectral range. Therefore a VCSEL is inherently single longitudinal mode. Also, since the cavity is vertical, the device needs to be not much larger than the desired spot size. Thus, the chip area required

for a VCSEL is not much larger than that commonly used for electronic devices. The device can be designed with a low aperture, circular output beam to match the optical mode of a fibre, permitting efficient coupling without extensive additional optics.

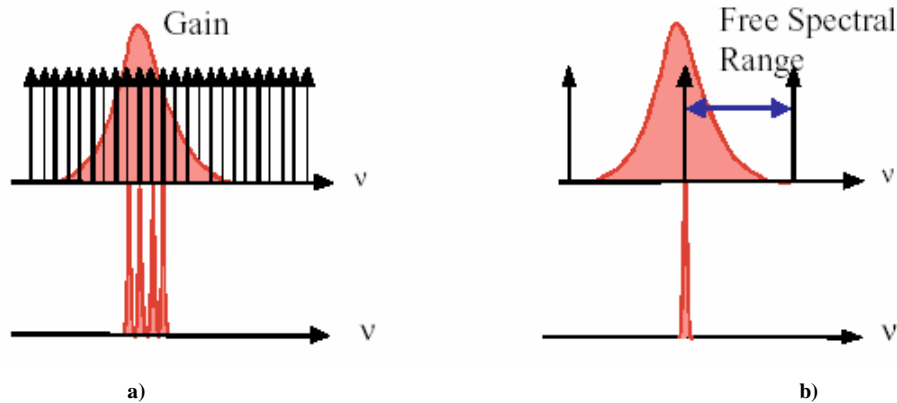


Figure 1.3: Due to the larger free spectral range VCSELS are inherently single longitudinal mode in contrast to their edge-emitting counterparts.

One can see that the short cavity length of the VCSEL constitutes the main physical difference between a VCSEL and an EEL with multiple implications on lasing mechanism. It was shown above that in VCSELS, the length of the order of a wavelength determines that only a single longitudinal mode to be supported in the cavity. Therefore, the length of the cavity and the reflection phase of the mirrors determine the emission wavelength while in an EEL this is given by the gain maximum of the quantum wells (QW). So it is mandatory for the VCSEL that the gain spectrum of the QWs coincides with the cavity mode.

Another implication of the different geometry concerns the maximum gain. Because a VCSEL has an extremely short gain-path length of $\sim 10\text{-}30$ nm, four orders of magnitude shorter than an EEL, the single pass gain in a VCSEL is typically as small as a fraction of 1%. Thus, to make a VCSEL, it is imperative to fabricate mirrors with very high reflectivities, an active region with high optical gain, and a cavity with very low optical losses. A simple calculation shows that for a VCSEL with a single-pass gain of 0.2% and no losses, the reflectivity product for the two mirrors needs to be as high as 99.6%. It is interesting to note that, even today, the mirrors remain the most critical part of VCSEL fabrication. A typical VCSEL mirror contains 20-40 pairs of semiconductors with different composition (e.g., AlGaAs/GaAs), whose thickness precision is required to be within a fraction of a percent.

Therefore, a typical VCSEL design should take into account the following issues:

- highly reflective and transparent DBRs;
- minimization of optical losses;
- maximization of optical field and gain overlap;
- electrode formation to reduce the resistivity for high-efficiency operation;
- heat-sinking for high-temperature and high-power operation.

1.3 Optical cavity and mirrors

The breakthrough in VCSELs evolution came together with the development of advanced growth methods such as molecular beam epitaxy (MBE), metal organic vapour phase epitaxy (MOVPE) and chemical beam epitaxy (CBE) that can provide superlattice structures achieving DBRs with reflectivities that exceed 99%. The principle used in the construction of DBRs is that of constructive interference since the reflectors are designed for a certain (resonant) wavelength. Basically a DBR consists in many quarter wavelength ($\lambda/4$) alternative layers of low-index and high-index materials. Field distribution and spectral dependencies of the reflectivity are suitably calculated by the transfer matrix method.

The main three materials systems used for distributed Bragg reflectors are: 1) GaAs/AlGaAs; 2) InP/InGaAsP; 3) AlGaInAs-based DBRs; 4) AlGaAsSb with different compositions.

1) By far the most used material system is the GaAs/AlGaAs system. It offers a good index contrast because of the relatively large difference between the AlAs index of 2.95 and the GaAs index of 3.52. This allows a relative small number of pairs to be grown in order to achieve high reflectivity DBRs. To obtain reflectivities above 99%, typically between 15 and 40 mirrors are used. Moreover, this system has the advantage that it can be grown lattice matched with the GaAs substrate to yield high-quality mirrors with a very good reproducibility. But multiple interfaces in DBRs introduce high electrical resistance with unwanted electrical power dissipation in the mirrors. Graded interfaces between the layers have been introduced to minimize the series resistance.

Figure 1.4 shows top and bottom GaAs/AlAs mirror reflectivities as a function of the number of layer pairs. Waves are incident from $\text{Al}_{0.3}\text{Ga}_{0.7}\text{As}$ and transmitted to air or GaAs in case of the top or bottom mirror, respectively, the latter having an additional AlAs quarter-wave layer. It can be seen that in case of a lossless top mirror, peak reflectivities exceeding 99.9% are to be expected for more than 21 mirror pairs. Lower reflectivities of the bottom mirror arise from the smaller index contrast at the output interface. The right-hand vertical axes shows the penetration depth which proves to be very similar for all three reflectors.

2) InP/GaInAsP distributed Bragg reflectors have also been grown with high values for the reflectivity: 99.9% [14]. The main problem in this materials system is that, because of the low index contrast between the two materials, a large number of periods (typically over 45 pairs) is necessary in order reach reflectivities suitable for VCSEL manufacturing. A major difficulty in using these DBRs arises from their poor thermal conductivity, which is the limiting factor for increasing the output power, especially at high temperature. However, all-epitaxial lattice matched InP-based $1.55\mu\text{m}$ VCSELs have been demonstrated to operate up to 88°C under cw conditions exploiting several imaginative designs: double intra-cavity contacted structure to circumvent the poor electrical and thermal conductivity of the mirrors, and current and optical confinement provided by an undercut aperture [15,16].

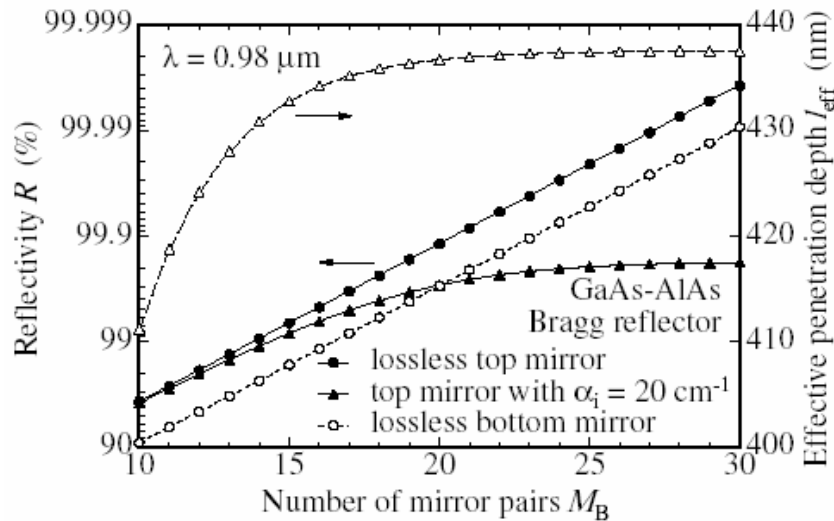


Figure 1.4: Peak reflectivities for a 980nm GaAs/AlGaAs DBR vs. the number of mirror pairs; The effective penetration depth proves to be very similar for all three detectors considered [13].

3) The AlGaInAs material have been used in combination with InP [17] or InAlAs [18] but if these materials are quite well-known, there is the same problem with the quite small optical index step at these wavelengths thus implying the need for very thick structures to obtain high reflectivity Bragg mirrors.

Two materials have been selected to be lattice matched with InP substrate and demonstrating the largest contrast between their refractive indices. $\text{Al}_{0.05}\text{Ga}_{0.42}\text{In}_{0.53}\text{As}$ and InP alloys have refractive indices of 3.8 and 3.17, respectively, resulting in refractive index difference of 0.63. Mirror reflectivity for 16 pairs of $\text{Al}_{0.05}\text{Ga}_{0.42}\text{In}_{0.53}\text{As}/\text{InP}$ alternating layers is 97% and for 22 pairs is 99.9% [19].

An alternative approach is to grow AlGaInAs/InAlAs DBRs which has the advantage that contains a single V element, thus allowing better control of the interfaces [20]. An all-epitaxial, optically pumped VCSEL has been demonstrated with 41 pairs for the bottom DBR (99.9% reflectivity) and 30 pairs for the top DBR (99.1%).

4) The material system based on AlGaAsSb is targeting the 1.3 μm and 1.55 μm wavelength ranges [21,22]. Important advances have been made once it had been discovered that the oxidation rate of highly reactive AlAsSb ternary reduces drastically by adding small amount of Ga. High contrast layers for VCSEL fabrication have been found to be $\text{Al}_{0.3}\text{Ga}_{0.7}\text{AsSb}/\text{Al}_{0.95}\text{Ga}_{0.05}\text{AsSb}$ and $\text{Al}_{0.15}\text{Ga}_{0.85}\text{AsSb}/\text{Al}_{0.95}\text{Ga}_{0.05}\text{AsSb}$ for 1.3 μm and 1.55 μm , respectively. Typically 20 pairs are needed to reach 99% reflectivity. But these structures suffer from interface roughness near the top layers and from thickness variations greater than 10%.

Figure 1.5 shows the reflectivity versus wavelength curves for 1.3 μm and 1.55 μm VCSEL structures with InP cavity and epitaxial lattice matched AlGaAsSb-based DBRs showing the typical Fabry-Pérot cavity mode near the center of the stop-band with a large stop-band of 90 and 150 nm respectively, making them ideal for WDM applications.

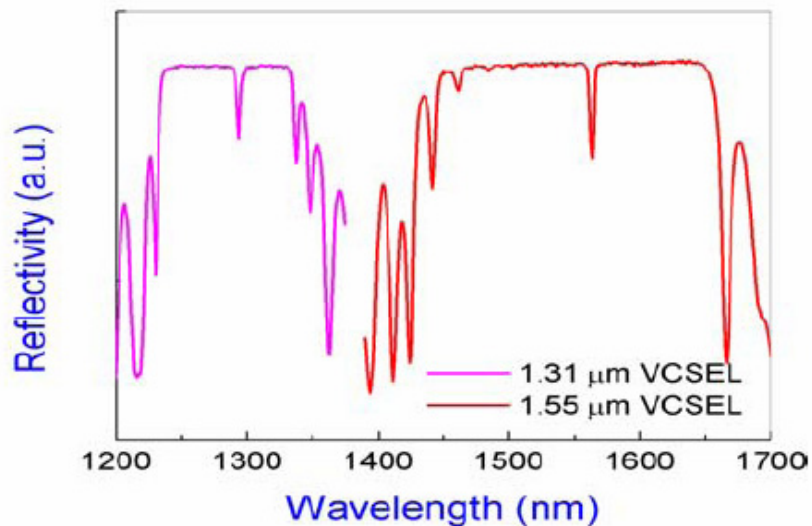


Figure 1.5: Reflectivity spectra of 1.3 μm and 1.55 μm VCSEL structures [21].

For the resonant cavity of the VCSELs, basically two materials have been used: AlGaAs and InP. The choice for the cavity material is closely related to the DBRs used. For the AlGaAs based cavities, the things are clear since the GaAs/AlGaAs mirrors are grown monolithically, lattice matched with the cavity. On the contrary, for the InP-based cavities several alternative approaches have been proposed and successfully demonstrated. The wafer fusion technique helps integrating the high-quality AlGaAs-based DBRs to active regions that provide long wavelength lasing. Initial results [23] were unsatisfactory because of the carrier injection problems since the quality of the fused surfaces is relatively poor. Continuous improvements have been reported in the last years in the performances of 1.5 μm VCSELs [24]. Recently, 1.5 mW single mode emission of a wafer fused 1.5 μm VCSEL has been demonstrated for a device that is able to operate up to 70° C [25].

A similar idea to combine the well established AlGaAs-based mirrors with long-wavelength material is the metamorphic growth of the mirror stack on the cavity material. This alternative approach has been shown to result in a good performance [26] by growing an n-type GaAs/AlAs top DBR directly on an InP based cavity where the current is injected from the p-side through a tunnel junction.

Quite often, the InP-based cavities are used in a combined design: together with an epitaxial, lattice matched Bragg stack and with a dielectric mirror. A 1.55 μm VCSEL has been demonstrated with output power up to 7 mW at room temperature, CW having a top mirror realized with AlGaInAs/InAlAs and the bottom mirror with $\text{CaF}_2/a\text{-Si/Au}$ (99.75% reflectivity) [27]. 6 pairs of ZnSe/MgF layers have been used together with AlGaAs-based DBRs bonded on an InP resonant cavity [28]. Also, an InGaAsP/InP DBR was used together with a 4 period multilayer reflector of Si/Al₂O₃ deposited by ion-assisted evaporation to complete an InP-based optical cavity [29,30].

1.4 Gain region

Using a proper combination of materials for the gain region it is possible to construct devices emitting over a very broad range of wavelengths (Figure 1.6). The choice of the material system for VCSEL design not only determines the emission wavelength, but it also influences many fabrication steps. A large number of III-V and II-VI material systems are of potential use in VCSELS. A direct band-gap for active layer material is a prerequisite and a close lattice match is an important requirement for obtaining a high crystal quality. But it is also possible to grow very thin high-quality pseudomorphically strained layers even if there is an important lattice mismatch. Such layers are very useful for making QW active layers at particular wavelengths and proved to be very reliable despite the very large strains in the lattice.

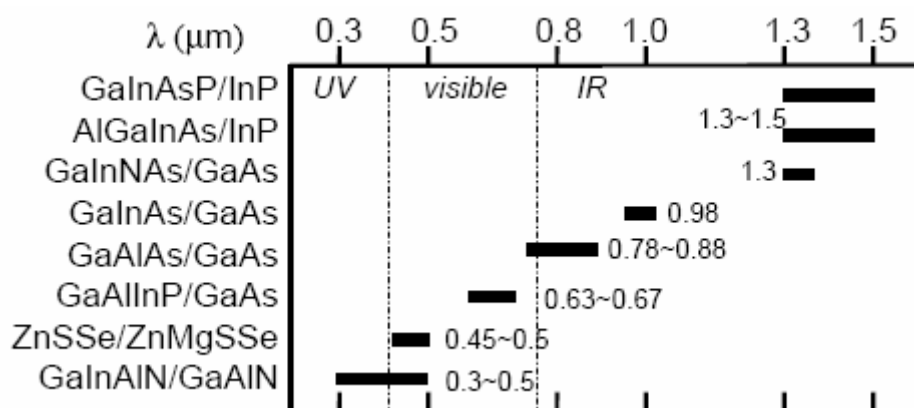


Figure 1.6: Materials for VCSELS in a wide spectral band [31].

The importance of surface-emitting lasers at 1.3 μm and 1.55 μm is increasing because of their applications in parallel lightwave systems and parallel optical interconnects. These two wavelengths correspond respectively to zero dispersion and minimum absorption in single mode silica fibers. As shown in the figure above, GaInAsP/InP and AlGaInAs/InP are two possible solutions for this wavelength range. The quaternary $Ga_xIn_{1-x}As_yP_{1-y}$ is lattice matched to InP substrates for $x=0.47y$. In the previous paragraph, a few problems appearing in this material system have already been mentioned as well as different approaches to circumvent them, especially regarding the growth of lattice matched high reflectivity DBRs.

The development of GaInNAs/GaAs VCSELS emitting at 1.3 μm [32] is very important for short distance optical links due to the low-cost chip and well-established processing technology for GaAs substrates. Such a device may readily replace edge-emitters for optical interconnects and links, if 1mW output power can be achieved. In 1997, the first RT CW photopumped laser oscillation of a VCSEL employing a GaInNAs–GaAs MQW active layer was reported [33]. Laser emission over an extremely broad 110 nm wavelength range, from 1.146–1.256 μm was obtained. At present, an intense research effort is focused on GaInAsN-based VCSELS at Infineon Technologies AG, demonstrating 700 μW CW single mode operation output power at room temperature for a VCSEL with GaInAsN

active region emitting at 1.3 μm [34] as well as data transmission up to 10 Gb/s at the telecom wavelength 1.3 μm [35]. More specific issues are investigated in-depth in the same group: insights into carrier recombination processes [36] or determination of band offsets in semiconductor QW structures [37].

While GaInNAs QWs can provide a larger modal gain [38], defects associated with N incorporation still limit the carrier lifetime [39] and, hence, the threshold current. On the contrary, QDs have the potential for a very low threshold current, due to the small transparency current associated with the low density of states. InAs/GaAs quantum dots have been proposed to be used in the active region [40] in order to get 1.3 μm emission in the AlGaAs/GaAs material system, opening a new research field that is still a hot topic today. The QD approach also has the potential to generate new and interesting device physics that stem from the atomic-like electronic density of states. Due to the high local In concentration in the dots, the emission wavelength can be tuned in the 1.1-1.7 μm wavelength region by varying the growth conditions [41,42], while the total strain is kept below the critical limit. Oxide-confined electrically pumped QD VCSELs operating at 1.154 μm have first been reported [40] in 1998. A QD VCSEL has also been demonstrated in 2000 [43] emitting at 1.3 μm .

The InGaAs/GaAs strained pseudomorphic system grown on a GaAs substrate emitting at 0.98 μm exhibits a high laser gain and has been introduced into surface-emitting lasers using GaAs/AlGaAs multi-layer reflectors. The use of compressively strained InGaAs/GaAs QWs in the active region results in lower threshold current and higher differential gain due to the increased splitting of the light and heavy-hole bands and the reduced effective mass of the heavy holes. Since these QWs emit at 0.98 μm , i.e below the GaAs bandgap, both top and bottom emitting geometries are possible. Wavelengths longer than 1.1 μm are not possible because of the limited critical thickness of the InGaAs/GaAs QWs, while wavelengths shorter than 0.93 μm are limited due to the loss of the carrier confinement in the QWs [44].

The GaAs/AlGaAs material system is the most studied for the fabrication of VCSELs and offers the most mature technology. As shown before, high crystal qualities can readily be obtained since the lattice constants of GaAs and AlAs are almost the same as well as high reflectivity DBR stacks can be made with only 20-30 quarter-wave pairs. Unstrained GaAs/AlGaAs QWs can be made to emit light in the wavelength range from 780 to 850 nm. Because GaAs is not transparent for these wavelengths, the devices should be either top emitting or the substrate should be etched.

Visible VCSELs are important for display applications. AlGaInP/GaAs surface-emitting lasers for 650-670 nm have been developed and RT operation exhibiting submilliamperes threshold and a few mW power output have been obtained [45,46]. The best application of red VCSELs may be laser printers and plastic optical fiber systems.

For the 555 nm range the ZnSe system is still the only material to provide cw operation of green-blue semiconductor lasers operating beyond 1000 hours. Some trials for green VCSELs were attempted.

GaN and related materials including Al, In and B can cover wide spectral ranges from green to UV. To date no GaN-based VCSEL have been reported due to the difficulty to achieve high reflectivity mirrors. However, the reported performance and reliability of GaN-based LEDs and LDs [47] indicates a good material potential for VCSELS as well.

1.5 The choice of VCSEL design

In order to effectively confine carriers in the active region and efficiently extract light from the device, different confinement schemes should be considered in the VCSELS' design. The most important technological approaches to achieve electrical and optical confinement will be presented in this paragraph.

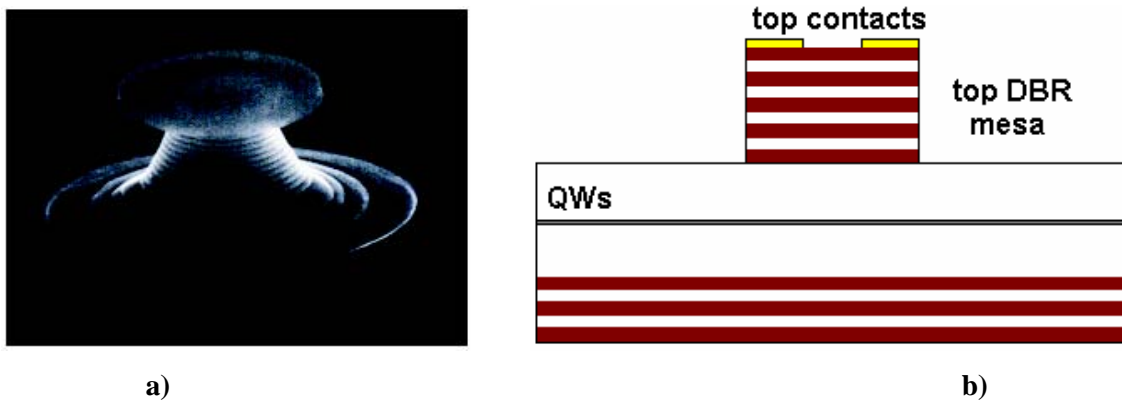


Figure 1.7: SEM photo [48] (a) and schematic view (b) of an air-post VCSEL.

A confinement solution that takes advantage of the index guiding is that of air-post VCSELS (Figure 1.7). To introduce lateral optical confinement plasma etch processing can readily make small area, deeply etched pillars with large index confinement due to the high contrast between the semiconductor and the air, but at the expense of increasing lateral losses due to optical scattering or surface recombination.

Gain guiding is used in devices that employ proton implant (Figure 1.8) for confinement. The principle is the electrical isolation of the device by ion implantation. The optical confinement is achieved exploiting the gain-guiding mechanism, i.e. the increase in refractive index in the presence of a high density of free carriers but this is a drawback for small device sizes. Therefore the proton implantation solution is reserved only for large devices, which require high threshold currents and have inherent multi-transverse mode operation. Also a special concern is to prevent damaging the active layer. The certain advantage of this structure is the planar configuration that allows a quite easy growth and processing. Actually, the most commercially available VCSELS are proton-implanted devices with multi-transverse mode behaviour. Proton implantation has already been brought to perfection to fabricate commercial VCSELS of outstanding producibility and reliability.

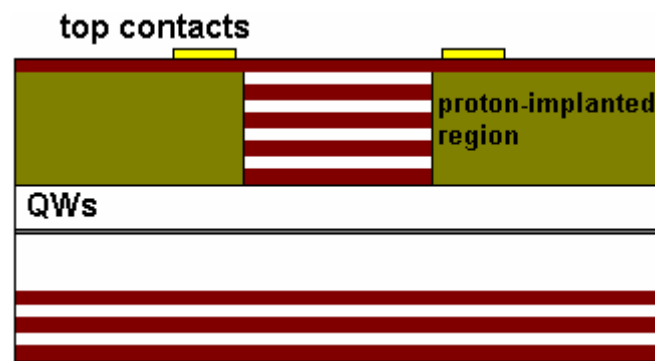


Figure 1.8: Schematic view of a proton-implanted VCSEL.

In contrast to strong index confinement along the entire cavity length, a somewhat surprising result is achieved by introducing the index-confinement into the cavity in only a strategically placed thin layer, thus forming an intracavity dielectric aperture. The dielectric aperture within the low loss planar microcavity introduces a small area, low loss optical mode. And by using the aperture to also confine the injected carriers a very low threshold current VCSEL can be achieved. An attractive means of introducing the dielectric aperture exists in the selective oxidation of AlAs. The introduction of **oxide-confinement** (Figure 1.9) marked a real revolution in VCSELs technology. This procedure is based on the extremely high oxidation selectivity, i.e. the rapidly increasing oxidation speed with Al content in the AlGaAs layer. The selective conversion of high Al composition epitaxial AlGaAs into a stable native oxide ring is performed using the “wet oxidation” process. Typically $\text{Al}_{0.98}\text{Ga}_{0.02}\text{As}$ composition is used in oxide aperture technology because of the problems associated with the high reactivity of the pure AlAs and device lifetime limitations. The oxide impact on VCSEL design can be two-fold. Its use as a dielectric aperture overcomes the limitations due to optical surface scattering and allows device scaling down to a few microns. Efforts at reducing electrical parasitics, optimising output coupling, and optimising the index confinement and thus mode overlap with the injected carriers has resulted in remarkable low threshold, high efficiency VCSEL performance for devices that use all semiconductor DBRs and the oxide-aperture confinement [10]. It might seem that in many respects the oxide-confined VCSEL has rapidly developed into a near optimum device, especially for AlGaAs–GaAs–InGaAs based devices, except for some interesting and outstanding problems in achieving high single mode power. However, the present oxide-confined VCSELs emitting around $0.98\ \mu\text{m}$ wavelength have the most impressive all-around performance for mode diameters in the $3\text{--}5\ \mu\text{m}$ range (unless one desires high output power and multimode behaviour, which is achieved at larger diameters). As the lateral size is decreased further, optical losses begin to dominate and increase the threshold current density and decrease the efficiency. Although quite low thresholds have been achieved, it has been at the expense of high threshold current densities and low output efficiencies. The second possible impact of the oxide resides in the possibility to form high-contrast AlO_x/GaAs DBRs that can be monolithically integrated beneath the VCSEL cavity. The shortening of the effective cavity length allows lateral size reduction smaller than what can be achieved with AlGaAs/GaAs

DBRs. A concern about designing a VCSEL based on the AlO_x/GaAs DBRs is the strain associated with the selectively oxidized material because of the volume contraction of ~10% associated with the oxidation of AlAs. The volume contraction is reduced with the addition of a few percent of Ga, but this is at the expense of slowing the oxidation rate. The volume contraction and the different thermal expansion coefficients between the native oxide and semiconductor can result in severe device damage for heat treatments beyond that used in the oxide formation.

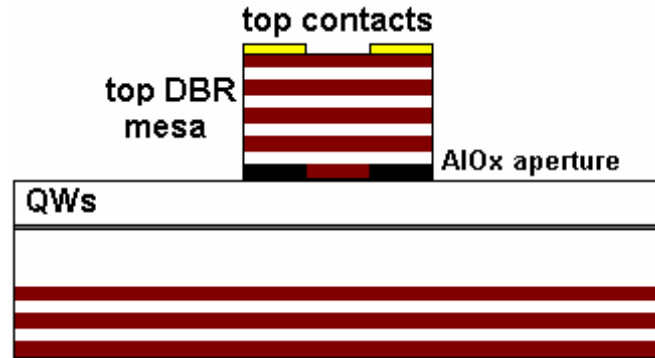


Figure 1.9: Schematic view of an oxide-confined VCSEL.

Not only the GaAs/AlGaAs material system beneficiaries of this oxide confinement method, but a similar method has been elaborated for InP-based devices where new aperture materials, namely AlGaAsSb-oxide have been explored. Sb segregation during the AlAsSb oxidation is a well-known problem. It has been observed that by the addition of 5% Ga to the ternary, the oxidation slows down, apparently arresting the Sb segregation [21]. The oxidation takes place at 350°C which is low enough to pose no problems to InP-based materials. Air apertures based on linear selective etch-rate of AlInAs have also been reported for this material system [16].

The buried oxide layer has profound implications, leading to new optical phenomena in the cavity. One novel optical effect is the strong modification of the longitudinal cavity resonance under the oxide layer relative to the as-grown cavity resonance. This is because the refractive index is reduced from 3 for the original AlGaAs layer to ~1.6 for the oxidised layer. The introduction of the oxide aperture determines a blue shift of the cavity resonance relative to the unoxidised cavity resonance and which has to be taken into account in the design of the layers' thicknesses.. In addition, the reflectivity across the mirror stop band is increased for the DBR containing the oxide layer as compared to the as-grown DBR. Both of these attributes arise from the significantly smaller refractive index of the oxide layer, and lead to unique lasing characteristics.

Another important issue in oxidised VCSELS concerns the placement of the oxide aperture and its effects on device characteristics. It is true that the introduction of low index apertures in the cavity confines the optical mode size and the current. But the aperture can also introduce losses. Different methods to reduce optical losses have been proposed: reducing the thickness of the apertures or making tapered apertures. By placing apertures at a node in the electric field standing wave, diffraction losses in the DBR can be reduced and high single-mode output powers can be obtained.

Actually when AlOx apertures are placed at a node there is no aperture dependent loss. It has also been shown that displacing apertures into the DBR where the optical field is reduced can also reduce these diffraction losses enabling fabrication of VCSELs with submicron apertures. However, when the apertures are placed at an antinode the internal loss is clearly a function of aperture size. For large multimode devices, the aperture placement does not play a role in the internal loss.

As a rule of thumb, planar, selectively oxidized VCSELs without extended cavity emit in a single transverse mode, up to active diameters of about 4 μm . Larger devices start lasing on several higher radial and azimuthal order modes right above or even at threshold. The light-current curve has a constant slope above threshold, as common for laser diodes, but shows a characteristic rollover for higher currents due to internal heating.

Furthermore, the design of oxide-apertured VCSELs allows the fabrication of **intracavity contacted VCSELs** (Figure 1.10) where the current is bypassing the DBRs [49]. Thus the high series electrical resistance introduced by the reflectors is avoided.



Figure 1.10: Schematic view of an intracavity contacted oxide-apertured VCSEL.

Generally, index-guided VCSELs are expected to have better performance than gain guided devices owing to the strong overlap of the electromagnetic field with the gain region in the device and current independent modal control.

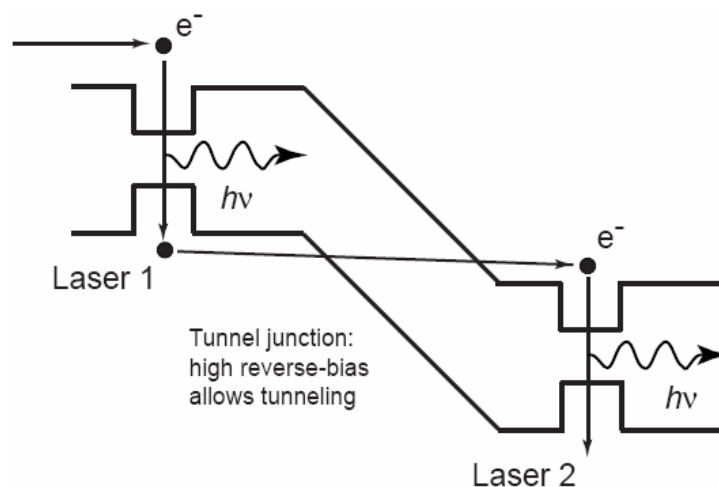


Figure 1.11: Schematic of the tunnel junction principle.

The **tunnel junction** constitutes an alternative approach for current injection that proved its reliability in special VCSEL designs. The operating principle of the tunnel junction laser is illustrated in Figure 1.11. This technique was employed in the realisation of a 1 mW, CW room temperature monolithic VCSEL emitting at 1.55 μm [26]. This device (Figure 1.12) consists in an InP/InGaAsP bottom mirror and a top, metamorphic GaAs/AlGaAs mirror directly grown on an InP-based cavity. The use of the tunnel junction enables one to employ two n-doped Bragg mirrors and, in addition, by H^+ implanting through the mirror to locally destroy the conductive properties of the tunnel junction, it allows one to localise the current injection without etching any mesa. Therefore, the whole processed structure remains planar.

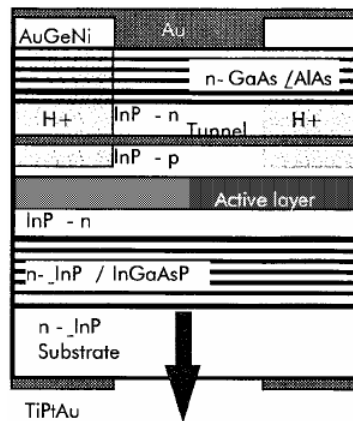


Figure 1.12: Vertical structure of the tunnel junction monolithic VCSEL emitting at 1.55 μm [26].

Another device that employs a tunnel junction was realised at Ulm Univ. [50] and is represented by a bipolar cascade VCSEL with monolithic stacking of active regions, electrically coupled by an Esaki tunnel junction. Due to this design, carriers can be recycled for additional radiative recombination, resulting in a higher round trip gain for cascade VCSELs compared to conventional structures. The structures (Figure 1.13) were realised in two configurations: two identical oxide apertures (design A) and only one oxide aperture (design B).

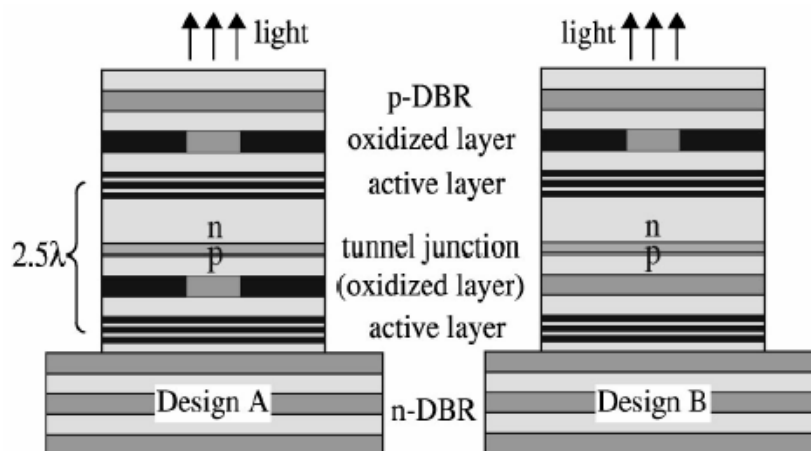


Figure 1.13: Cross sections of two cascade VCSELs with tunnel junctions [50].

1.6 VCSELs for wavelength engineering

One can see that due to their peculiarities VCSELs are ideal candidates for wavelength engineering. The Fabry-Perot (longitudinal) mode (within the laser gain bandwidth), which determines the lasing wavelength, can be modified by slightly varying the cavity length. The resonant mode can be tuned in a wavelength range given by the specific material system. This issue is discussed below. The possibility of engineering multi-wavelength laser arrays and wavelength-tunable lasers opened multiple opportunities for WDM system applications. WDM is one of the most expedient methods for increasing the transmission capacity of optical interconnects, such as an optical fibre. By transmitting signals in N channels (wavelengths) through one single fibre, the aggregate bandwidth can be increased by a factor of N without the need of physically increasing the number of fibres. WDM systems are now being rapidly deployed in telecommunication systems in the 1.55 μm -wavelength regime.

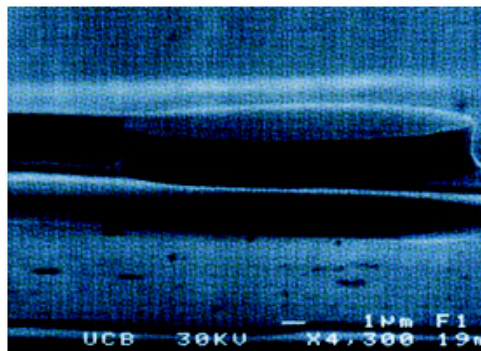


Figure 1.14: SEM of a micromechanically tunable VCSEL [51];

The top mirror of a VCSEL includes an air gap and a DBR, suspended above the rest of the heterostructure and supported by a cantilever.

Even if several different approaches have been tried for wavelength engineering, it was clear that no effect can vary the wavelength as effectively and over as large a range as a physical change of the cavity length itself. One solution to this problem is to create a structure where the VCSEL top mirror may be translated via a micromechanical structure. A micromechanical tunable VCSEL was reported by Hasnain and co-workers [51] and is presented in Figure 1.14, with its entire mechanical structure made of GaAs/AlGaAs epitaxial material with very high-thickness precision. An air-gap was made in the VCSEL cavity by selective removal of some of the epitaxial (GaAs/AlGaAs) material. Thus, most of the VCSELs top DBR is suspended above the rest of the heterostructure and is supported by a cantilever. A voltage is applied to the two contacts surrounding the air-gap, which makes the cantilever move up and down to vary the gap size, and thus, the VCSEL cavity length is varied, altering the Fabry-Perot wavelength. A third contact is used to inject current into the active region beneath the air-gap. A very wide, nearly continuous tuning range of 32 nm (13 THz) was

achieved for this structure. This VCSEL also exhibits excellent and uniform light-current characteristics over the entire tuning range.

An alternative approach was to integrate a thin-film heater [52] in the VCSEL design achieving a continuous wavelength tuning range of 10.1 nm. This method has several advantages: the design and fabrication process are very simple; no multiple mesa contacting scheme is needed; the heater is completely separated from the laser so that it can be added to most existing VCSEL structures after they have been fabricated. The heater can be optimised without changing the VCSEL structure or sacrificing its performance.

We have shown before that in the field of long-wavelength VCSELS that rely on the InP-based system, the method of wafer fusion is a good solution in order to combine AlGaAs-based DBRs with InP-based cavity materials. From the point of view of electrical and thermal conductivity AlGaAs-based DBRs considerably outperform DBRs in other material systems, while InGaAsP and especially InGaAlAs based multiquantum wells grown on InP are known to show the best performance in 1550 nm lasers. By structuring one or both wafers to be fused it is possible to fabricate devices with built-in lateral electric and optical confinement like single wavelength VCSELS. This technology also permits the introduction of device configurations that are either impossible or very difficult to obtain reliably, solely with post-fusion processing steps. One example is the mesa trimming technique, used to precisely determine the cavity length, applied in multiple-wavelength VCSEL array structures [53]. Significant advances have been made up-to-date so that 1.5 mW single mode operating VCSELS at 1.55 μm have been reported in 2003 [25] obtained by wafer fusion.

One can see in Figure 1.15 that the wafer fusion process allows for a continuous variation of the cavity length across the wafer. In this manner, VCSEL arrays can be obtained with emission wavelength variation range up to 60 nm (Figure 1.16).

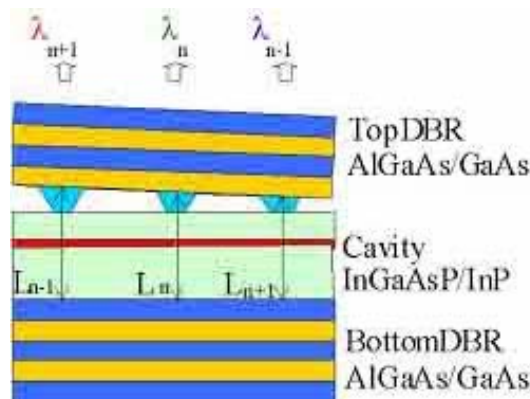


Figure 1.15: Schematic of the mesa trimming process for cavity length engineering [53].

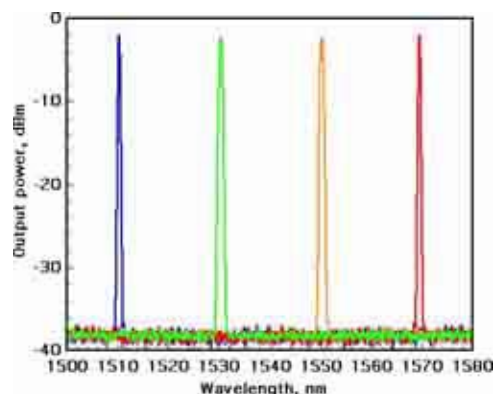


Figure 1.16: Emission spectra of coarse WDM VCSEL array fabricated with the localized fusion technique [53].

Bibliography CHAPTER 1

- [1] R. N. Hall, G. E. Fenner, J. D. Kingsley, T. J. Soltys, and R. O. Carlson, "Coherent light emission from GaAs junctions", *Phys. Rev. Lett.*, **9**, pp. 366-369, 1962.
- [2] K. Iga, Lab. Note, March 22, 1977.
- [3] H. Soda, K. Iga, C. Kitahara, and Y. Suematsu, "GaInAsP/InP surface emitting injection lasers", *Japan. J. Appl. Phys.*, **18**, pp. 2329-2330, 1979.
- [4] J.P. van der Ziel and M. Ilegems, "Multilayer GaAs-Al_{0.3}Ga_{0.7}As dielectric quarter wave stacks grown by molecular beam epitaxy", *Applied Optics*, **14**, pp. 2627-2630, 1975.
- [5] K. Iga, S. Ishikawa, S. Ohkouchi, and T. Nishimura, "Room-temperature pulsed oscillation of GaAlAs/GaAs surface emitting injection laser", *Appl. Phys. Lett.*, **45**, pp. 348, 1984.
- [6] F. Koyama, S. Kinoshita, and K. Iga, "Room-temperature CW operation of GaAs vertical-cavity surface emitting laser", *trans. IEICE*, vol. E71, pp. 1089-1090, 1988.
- [7] F. Koyama, S. Kinoshita, and K. Iga, "Room-temperature continuous-wave lasing characteristics of a GaAs vertical-cavity surface-emitting laser", *Appl. Phys. Lett.*, **55**, pp. 221-223, 1989.
- [8] R. S. Geels and L. A. Coldren, "Submilliwatt threshold vertical-cavity laser diodes", *Appl. Phys. Lett.*, **57**, pp. 1605-1607, 1990.
- [9] R. S. Geels, S. W. Corzine, and L. A. Coldren, "InGaAs Vertical-Cavity Surface-Emitting Lasers", *IEEE J. Quantum Electron.*, **27**, no. 6, pp. 1359-1367, 1991.
- [10] D. L. Huffaker, D. G. Deppe, K. Kumar, and T. J. Rogers, "Native oxide defined ring contact for low threshold vertical cavity lasers", *Appl. Phys. Lett.*, **65**, pp. 97-99, 1994.
- [11] K. D. Choquette, R. P. Schneider, K. L. Lear, and K. M. Geib, "Low threshold voltage vertical cavity lasers fabricated by selective oxidation", *Electron. Lett.*, **30**, pp. 2043-2044, 1994.
- [12] K. L. Lear, A. Mar, K. D. Choquette, S. P. Kilcoyne, R. P. Schneider, and K. M. Geib, "High-frequency modulation of oxide confined vertical cavity surface emitting lasers", *Electron. Lett.*, **32**, pp. 457-458, 1996.
- [13] R. Michalzik and K. J. Ebeling, "Operating principles of VCSELs", Univ. of Ulm, Optoelectronics Department.
- [14] K. Streubel, S. Rapp, J. André, and J. Wallin, "Room-Temperature Pulsed Operation of 1.5 μ m Vertical Cavity Lasers with an InP-Based Bragg Reflector", *IEEE Phot. Tech. Letters*, **8**, 1121-1123 (1996).

- [15] S. Nakagawa, E. Hall, G. Almuneau, J. K. Kim, D. A. Buell, H. Kroemer, and L. A. Coldren, “88°C, continuous-wave operation of apertured, intracavity contacted, 1.55 μ m vertical-cavity surface-emitting lasers”, *Appl. Phys. Lett.*, **78**, pp. 1337-1339, 2001.
- [16] T. Asano, D. Feezell, R. Koda, M. H. M. Reddy, D. A. Buell, A. S. Huntington, E. Hall, S. Nakagawa, and L. A. Coldren, “InP-Based All-Epitaxial 1.3 μ m VCSELS With Selectively Etched AlInAs Apertures and Sb-Based DBRs”, *IEEE Photon. Technol. Lett.*, **15**, pp. 1333-1335, 2003.
- [17] A.J. Moseley, J. Thomson, D.J. Robbins, and M.Q. Kearley, “High reflectivity AlGaInAs/InP multi layers mirrors grown by low pressure MOVPE for application to long wavelength high contrast ratio multi-quantum-well modulators”, *Electron. Lett.*, **29**, pp. 1717-1718 (1989).
- [18] W. Kowalsky and J. Mähns, “Monolithically integrated InGaAlAs dielectric reflectors for vertical cavity optoelectronic devices”, *Appl. Phys. Lett.*, **59**, pp. 1011-1012 (1991).
- [19] M. Linnik and A. Christou, “Vertical Cavity Surface Emitting Laser with AlGaInAs/InP Bragg mirrors fabricated for operation at 1.55 μ m” at http://www.mne.umd.edu/staff/faculty_profiles/christou/vcSEL.pdf.
- [20] J.-Ph. Debray, N. Bouché, G. Le Roux, R. Raj, and M. Quillec, “Monolithic vertical cavity device lasing at 1.55 μ m in InGaAlAs system”, *Electron. Lett.*, **33**, pp. 868-869 (1997).
- [21] L. Coldren, “Monolithic InP-based long-wavelength VCSELS”, Project Report 2001-02 for MICRO Project 01-018.
- [22] S. Nakagawa, E. Hall, G. Almuneau, J. K. Kim, D. A. Buell, H. Kroemer, and L. A. Coldren, “1.55 μ m InP lattice matched VCSELS with Al- GaAsSb-AlAsSb DBRs,” *IEEE J. Select. Topics Quantum Electron.*, **7**, pp. 224–230, Mar./Apr. 2001.
- [23] V. Jayaraman, J.C. Geske, M.H. MacDougall, F.H. Peters, T.D. Lowes, T.T. Char, “Uniform threshold current, continuous-wave, single mode 1300nm VCSEL from 0 to 70°C”, *Electron. Lett.*, **34**, pp. 1407, 1998.
- [24] A. V. Syrbu, V. P. Iakovlev, C. A. Berseth, O. Dehaese, A. Rudra, E. Kapon, J. Jacquet, J. Boucart, C. Stark, F. Gaborit, I. Sagnes, J. C. Harmand, and R. Raj, “30 C operation of 1.52 μ m InGaAsP/AlGaAs VCSELS with in-situ built-in lateral current confinement by localized fusion,” *Electron. Lett.*, **34**, pp. 1744–1745, 1998.
- [25] A. Syrbu, A. Mircea, A. Mereuta, A. Caliman, C.-A. Berseth, G. Suruceanu, V. Iakovlev, M. Achtenhagen, A. Rudra, and E. Kapon, “1.5mW Single-Mode Operation of Wafer-Fused 1550-nm VCSELS”, *IEEE Phot. Tech. Lett.*, **16**, pp. 1230-1232 (2004).
- [26] J. Boucart, C. Starck, F. Gaborit, A. Plais, N. Bouché, E. Derouin, L. Goldstein, C. Fortin, D. Carpentier, P. Salet, F. Brillouet, J. Jacquet, “1mW CW-RT monolithic VCSEL at 1.55 μ m”, *IEEE Photon. Technol. Lett.*, **11**, pp. 629-631 (1999).
- [27] R. Shau, M. Ortsiefer, J. Roskopf, G. Böhm, F. Köhler, and M.-C. Amann, “Vertical-cavity surface-emitting laser diodes at 1.55 μ m with large output power and high operation temperature”, *Electron. Lett.*, **37**, pp. 1295-1296 (2001).
- [28] Y. Qian, Z. H. Zhu, Y. H. Lo, D. L. Huffaker, D. G. Deppe, H. Q. Hou, B. E. Hammons, W. Lin, and Y. K. Tu, “Low-Threshold Proton-Implanted 1.3 μ m Vertical-Cavity Top-Surface-Emitting Lasers with Dielectric and Wafer-Bonded GaAs–AlAs Bragg Mirrors”, *IEEE Photon. Tech. Lett.*, **9**, pp. 866-868 (1997).
- [29] M.A. Fisher, Y.-Z. Huang, A.J. Dann, D.J. Elton, M.J. Harlow, S.D. Perrin, J. Reed, I. Reid, and M.J. Adams, “Pulsed Electrical Operation of 1.55 μ m Vertical-Cavity Surface-Emitting Lasers”, *IEEE Photon. Technol. Lett.*, **7**, pp. 608-610 (1995).
- [30] N. Nishiyama, C. Caneau, G. Guryanov, X. S. Liu, M. Hsu, and C. E. Zah, “High efficiency long wavelength VCSELS on InP grown by MOCVD,” *Electron. Lett.*, **39**, pp. 437–439 (2003).
- [31] K. Iga and F. Koyama, “Surface-emitting lasers”, *Semiconductor lasers II. Materials and structures*, pp. 323–372, San Diego, CA: Academic Press, 1999.

- [32] T. Miyamoto, K. Takeuchi, F. Koyama, and K. Iga, "A Novel GaInNAs–GaAs Quantum-Well Structure for Long-Wavelength Semiconductor Lasers", *IEEE Photon. Technol. Lett.*, **9**, pp. 1448-1450, 1997.
- [33] M. C. Larson, M. Kondow, T. Kitatani, K. Tamura, Y. Yazawa, and M. Okai, "Photopumped Lasing at 1.25 μm of GaInNAs–GaAs Multiple-Quantum-Well Vertical-Cavity Surface-Emitting Lasers", *IEEE Photon. Technol. Lett.*, **9**, pp. 1549-1551, 1997.
- [34] H. Riechert, A. Ramakrishnan, G. Steinle, "Development of InGaAsN-based 1.3 μm VCSELs", *Semiconductor Science and Technology*, **17**, p. 892-897, 2002.
- [35] G. Steinle, G. Kristen, H. Riechert, A.Y. Egorov, F. Mederer, M. Kicherer, R. Michalzik, K.J. Ebeling, "Data Transmission up to 10 Gbit/s with 1.3 μm Wavelength InGaAsN VCSELs", *Electron. Lett.*, **37**, p. 632, 2001.
- [36] G. Steinle, H. Riechert, A. Egorov, "Monolithic VCSEL with InGaAsN active region emitting at 1.28 μm and CW output power exceeding 500 μW at room temperature", *Electron. Lett.*, **37**, pp. 93-95, 2001.
- [37] Gh. Dumitras and H. Riechert, "Determination of band offsets in semiconductor quantum well structures using surface photovoltage", *Journal of Applied Physics*, **94**, pp. 3955-3958, 2003.
- [38] B. Borchert, A. Y. Egorov, S. Illek, M. Komainda, and H. Riechert, "1.29 μm GaInNAs multiple quantum-well ridge-waveguide laser diodes with improved performance," *Electron. Lett.*, **35**, pp. 2204–2206, 1999.
- [39] S. R. Kurtz, A. A. Allerman, E. D. Jones, J. M. Gee, J. J. Banas, and B. E. Hammons, "InGaAsN solar cells with 1.0 eV band gap, lattice matched to GaAs," *Appl. Phys. Lett.*, **74**, pp. 729–731, 1999.
- [40] D. L. Huffaker, H. Deng, and D. G. Deppe, "1.15 μm wavelength oxide-confined quantum dot vertical-cavity surface-emitting laser", *IEEE Photon. Technol. Lett.*, **10**, pp. 185-187, 1998.
- [41] D. L. Huffaker and D. G. Deppe, "Electroluminescence efficiency of 1.3 μm wavelength InGaAs/GaAs quantum dots," *Appl. Phys. Lett.*, **73**, pp. 520–522, 1998.
- [42] M. V. Maximov, A. F. Tsatsulnikov, B. V. Volovik, D. A. Bedarev, A. Y. Egorov, A. E. Zhukov, A. R. Kovsh, N. A. Bert, V. M. Ustinov, P. S. Kop'ev, and Z. I. Alferov, "Optical and structural properties of InAs quantum dots in a GaAs matrix for a spectral range up to 1.7 μm ," *Appl. Phys. Lett.*, **75**, pp. 2347–2349, 1999.
- [43] J. A. Lott, N. N. Ledentsov, V. M. Ustinov, N. A. Maleev, A. E. Zhukov, A. R. Kovsh, M. V. Maximov, B. V. Volovik, Z. I. Alferov, and D. Bimberg, "InAs-InGaAs quantum dot VCSEL's on GaAs substrates emitting at 1.3 μm ," *Electron. Lett.*, **36**, pp. 1384–1385, 2000.
- [44] T. E. Sale, "Vertical Cavity Surface Emitting Lasers", Research Studies Press, Taunton, England, 1995.
- [45] J. A. Lott; R.P. Schneider Jr.; K.J. Molly, "Visible (639 nm $<\lambda<$ 661 nm) vertical cavity surface emitting laser diodes", *IEEE Trans. on Electron Devices*, **40**, pp. 2115 - 2116, 1993.
- [46] R.P. Schneider Jr.; K.D. Choquette; J.A. Lott, K.L. Lear, J.J. Figiel, and K.J. Malloy, "Efficient room-temperature continuous-wave AlGaInP/AlGaAs visible (670 nm) vertical-cavity surface-emitting laser diodes", *IEEE Phot. Tech. Lett.*, **6**, pp. 313 – 316, 1994.
- [47] S. Nakamura et al., *Jpn. J. Appl. Phys.*, **35**, L14-L16, 15 J, 1996.
- [48] C.J. Chang-Hasnain, *Advances of VCSELs*, Optical Soc. America, 1997.
- [49] B.J. Thibeault, J.W. Scott, M.G. Peters, F.H. Peters, D.B. Young, and L.A. Coldren, "Integrable InGaAs/GaAs vertical-cavity surface-emitting lasers", *Electron. Lett.*, **29**, pp. 2197-2199, 1993.
- [50] T. Knödl, R. Michalzik, M. Golling, and K.J. Ebeling, "Current-spreading-induced bistability in bipolar cascade vertical-cavity surface-emitting lasers", *Appl. Phys. Lett.*, **81**, pp. 583-585 (2002).

[51] M.Y. Li, W. Yuen, G. S. Li, C. J. Chang-Hasnain, "Top-emitting micromechanical VCSEL with a 31.6nm tuning range", *IEEE Phot. Tech. Lett.*, **10**, pp. 18-20, 1998.

[52] L. Fan, M.C. Wu, H.C. Lee, and P. Grodzinski, "10.1nm range continuous wavelength-tunable vertical-cavity surface-emitting lasers", *Electron. Lett.*, **30**, pp. 1409-1410, 1994.

[53] Details at <http://www.beamexpress.com/>

Chapter 2

VCSELs – theory of operation

2.1 Introduction

As this thesis is focused on coupled-cavity VCSELs, we will start with some general considerations on classic, single cavity VCSELs and, more generally, with diode lasers. This chapter gives a phenomenological approach to diode lasers, emphasizing the characteristics that individualise VCSEL devices. The presentation will follow the procedure given by Coldren in reference [1].

Diode lasers, like most other lasers, incorporate an optical gain medium in a resonant optical cavity. The design of both the gain medium and the resonant cavity are critical. The gain medium consists in a material that absorbs incident radiation over some wavelength range of interest. If it is pumped with either electrical or optical energy, the electrons within the material can be excited to higher, non-equilibrium energy levels, so the incident radiation can be amplified rather than absorbed by stimulating the de-excitation along with the generation of additional radiation. If the resulting gain is sufficient to overcome the losses of some resonant optical mode of the cavity, this mode is said to have reached threshold, and coherent light will be emitted. The resonant cavity provides the necessary positive feedback for the radiation being amplified, so that a lasing oscillation can be established and sustained above threshold pumping levels. As in any other oscillator, the output power saturates at a level equal to the input minus any internal losses.

Together with gas lasers and solid-state lasers, diode lasers are only one class of laser devices. The possibility of direct electrical pumping specific to diode lasers result in a more efficient operation. Overall power conversion efficiencies of ~50% are specific to diode lasers, whereas in the case of gas and solid state lasers the common values are around 1%. However, in the case of CO₂ gas lasers, the typical efficiency is over 10%.

Net size is another striking difference between semiconductor and other lasers. While gas and solid state lasers are typically tens of centimeters in length, packaged diode laser chips size is of the order of a cubic centimeter.

An outstanding quality of diode lasers that has led to their widespread use in important applications such as fiber optic communication systems is their high reliability or useful lifetime. While the useful lifetime of gas or solid state lasers is typically measured in thousands of hours, that of carefully qualified diode lasers should exceed hundreds of years.

2.2 Energy levels and bands in solids

In order to understand how gain is accomplished in diode lasers, one has to understand how electrons can occupy the energy levels in the gain medium. The allowed energy levels are obtained by solving Schrödinger's equation using the appropriate electronic potentials. Figure 2.1 schematically illustrates the energy levels that might be associated with optically induced transitions in both an isolated atom and a semiconductor. Electron potential is plotted vertically.

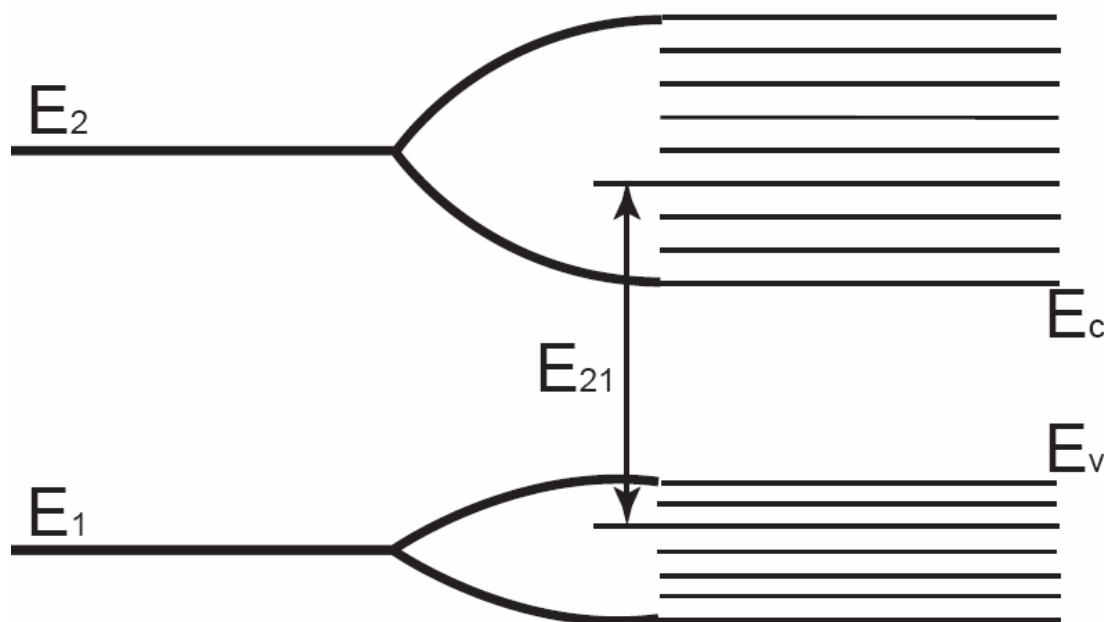


Figure 2.1: Illustration on how two discrete energy levels of an atom develop into bands of many levels in a crystal.

The semiconductor valence band is formed by the multiple splitting of the highest occupied atomic energy level of the constituent atoms. In semiconductors, the valence band is by definition entirely filled with no external excitation at $T=0K$. The next higher-lying atomic level splits apart into the conduction band which is entirely empty in semiconductors without any excitation. When thermal or other energy is added to the system, electrons in the valence band may be excited into the conduction band analogous to how electrons in isolated atoms can be excited to the next higher energy level of the atom. In the solid then, this excitation creates holes (missing electrons) in the valence band as well as electrons in the conduction band, and both can contribute to conduction.

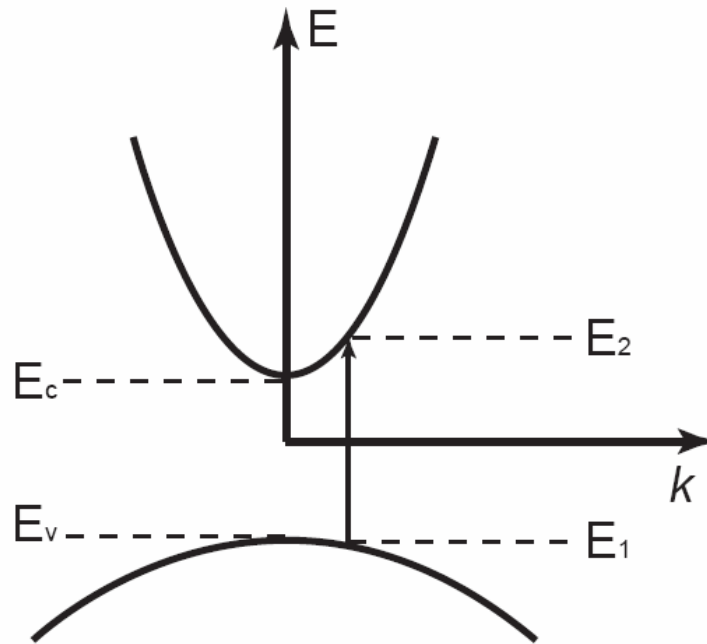


Figure 2.2: Electron energy vs. wave number in a semiconductor showing a transition of an electron from a bound state in the valence band (E_1) to a free carrier state in the conduction band (E_2). The transition leaves a hole in the valence band. The lowest and higher energies in the conduction and valence bands are E_c and E_v , respectively.

Imposing the momentum conservation in addition to energy conservation limits the interaction between photons and conduction-valence state pairs to a limited set of state pairs for a given transition energy. This situation is illustrated on the electron energy versus k -vector (E - k) plot shown schematically in Figure 2.2. Since the momentum of the interacting photon is negligibly small, transitions between the conduction and the valence band must have the same k -vector, and only vertical transitions are allowed on this diagram.

2.3 Spontaneous and stimulated transitions: the creation of light

We proceed to consider the electronic transitions that can exist and the possible interactions with lightwaves. Figure 2.3 illustrates the different kinds of important electronic transitions, emphasizing those that involve the absorption or emission of photons. Four basic electronic recombination/generation (photon emission/absorption) mechanisms must be considered separately: (1) stimulated generation (photon absorption); (2) stimulated recombination (coherent photon emission); (3) spontaneous recombination (photon emission); and (4) non-radiative recombination. Electron and hole densities are highest near the bottom or top of the conduction or valence bands, respectively. So, most transitions of interest involve these carriers. Thus, photon energies tend to be only slightly larger than the bandgap, i.e. $E_{21} = h\nu \sim E_g$. The effects involving electrons in the conduction band are all enhanced by the addition of some pumping means to increase the electron density to

above the equilibrium value there. The photon absorption can still take place even if some pumping has populated the conduction band somewhat.

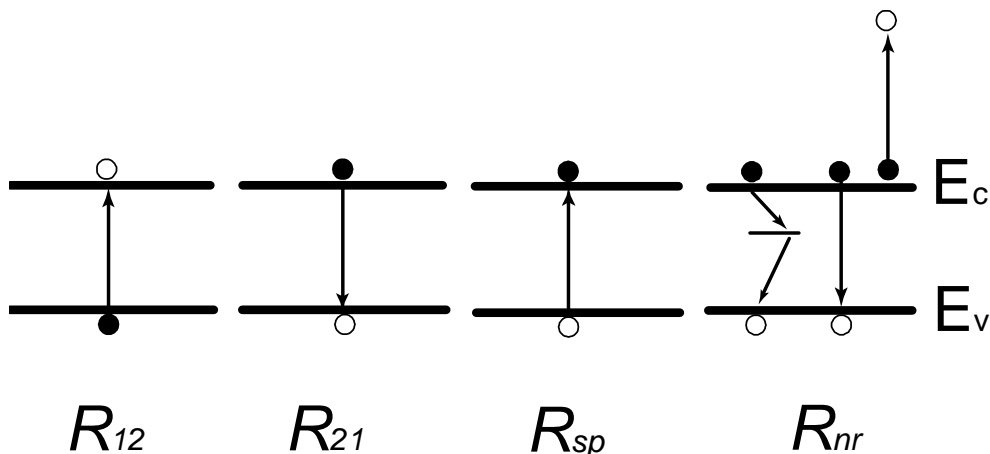


Figure 2.3: Electronic transitions between the conduction and valence bands. The first three represent radiative transitions in which the energy to free or bind an electron is supplied by or given to a photon. The fourth illustrates two non-radiative processes.

The first process (R_{12}) outlines photon absorption which stimulates the generation of an electron in the conduction band while leaving a hole in the valence band. In this process, the energy of a photon is transferred to an electron, elevating it from some state 1 in the valence band to some state 2 in the conduction band. Such stimulated absorption events generate new carriers and are responsible for the disappearance of photons.

The second process (R_{21}) is exactly the same as the second, only the sign of the interaction is reversed. An incident photon perturbs the system, stimulating the recombination of an electron and a hole, and simultaneously generating a new photon. This is the all important positive gain mechanism that is necessary for lasers to operate. The net combination of stimulated absorption and emission of photons, effects (R_{12}) and (R_{21}), will represent the net gain experienced by an incident radiation field.

The third case (R_{sp}) is really no different from the second one except that the field which stimulates the electron to emit a photon and make a downward transition is not a real field but a vacuum-field. Because vacuum-field transitions can occur with no classical field stimulation, we refer to them as spontaneous emission events. In other words, this process represents the case of an electron in the conduction band recombining spontaneously with a hole (missing electron) in the valence band to generate a photon. If a large number of such events should occur, relatively incoherent emission would result, since the emission time and direction would be random, and the photons would not tend to contribute to a coherent radiation field. This is the primary mechanism within a light-emitting diode (LED), in which photon feedback is not provided.

The fourth schematic in Figure 2.3 represents the several non-radiative ways in which a conduction band electron can recombine with a valence band hole without generating any useful photons. The energy is dissipated as heat in the semiconductor crystal lattice. This schematic

represents the ways in which conduction band electrons can escape from usefully contributing to the gain. In practice, two general non-radiative mechanisms are important. The first involves non-radiative recombination centers, such as point defects, surfaces and interfaces, in the active region of the laser. The second mechanism is the Auger recombination in which the electron-hole recombination energy, E_{21} , is given to another electron or hole in the form of kinetic energy.

The rates at which the first three radiative processes in Figure 2.3 occur depend on a number of factors. Two primary factors are the density of photons and the density of available state pairs. The dependence on the photon density enters through the local electric field strength, $|E|^2$. Thus $R_{12}, R_{21} \propto |E|^2$ and $R_{sp} \propto |E^{v-f}|^2$, where $|E^{v-f}|^2$ is the vacuum-field strength.

The dependence of the transition rates on the density of available state pairs can be broken down into two components: one which is strictly material dependent, and the other which depends on the injection levels. The first component is the density of total state pairs, which is found by taking the appropriate average between the density of states in the conduction and the valence bands. The second component is the fraction of state pairs available to participate in the transition. For upward transitions this fraction is maximized when all carriers are placed in the valence band. For downward transitions, this fraction is maximized when all carriers are placed in the conduction band. The former population of carriers occurs naturally, while the latter inverted population can only be achieved by providing energy which pumps the carriers into the conduction band – for example, by current injection into the center of a p-n junction.

An interesting feature of the downward transitions is that in addition to appearing in the same optical mode, the newly created photon also contributes to the existing field constructively. This feature allows the optical mode to build up a very coherent field. The vacuum-field phase is not correlated with the phase of real fields in the optical mode. As a result, new photons introduced into the field through spontaneous emission have random phases relative to the coherent fields created through stimulated emission. And although the number of photons introduced into the mode through spontaneous emission can be made small relative to the photons introduced through stimulated emission, they can never be removed completely, implying that perfect coherence in a laser can never be achieved.

So far we have not specified the electron states 1 and 2 in any detail. Photons with energy $h\nu$ induce upward and downward transitions only between those electron state pairs which conserve both energy and momentum in the course of transition. In other words, we must have $E_2 - E_1 = E_{21} = h\nu$ and $\mathbf{k}_2 = \mathbf{k}_1$. These conservation laws reduce the interaction to a very particular region of the E - k diagram of a semiconductor. Within this region, only vertical transitions are allowed.

Another restriction one must consider is that transitions occur only between filled initial states and empty final states. The above figure illustrates the fraction of state pairs which satisfy this criterion for both upward and downward transitions. Writing out the Fermi factors explicitly:

$$\begin{aligned} R_{12} &= R_r \cdot f_1 \cdot (1 - f_2) \\ R_{21} &= R_r \cdot f_2 \cdot (1 - f_1) \end{aligned} \quad (2.1)$$

In these equations, R_r represents the radiative transition rate that would exist if all state pairs were available to participate in the transition. R_r is proportional to the field strength and the reduced density of states function.

Because R_{21} and R_{12} are competing effects in that one generates new photons and the other takes them away, the net generation rate of photons in the semiconductor is given by:

$$R_{st} \equiv R_{21} - R_{12} = R_r \cdot (f_2 - f_1) \quad (2.2)$$

We will show in Section 2.6 by a more phenomenological route that the net stimulated emission rate, R_{st} , is directly proportional to the optical gain in the material.

The occupation probabilities are described using Fermi statistics even under non-equilibrium conditions by using a separate Fermi level for the conduction and valence bands:

$$f_1 = \frac{1}{\exp(E_1 - E_{F_v})/kT + 1} \quad \text{and} \quad f_2 = \frac{1}{\exp(E_2 - E_{F_c})/kT + 1} \quad (2.3)$$

where E_{F_c} and E_{F_v} are the conduction and valence band quasi-Fermi levels. Under non-equilibrium forward bias conditions, E_{F_c} and E_{F_v} are separated by slightly less than the applied voltage to the junction.

Simple relations between the transition rates are easily derived by substituting the occupation probabilities:

$$\frac{R_{21}}{R_{12}} = \frac{f_2 \cdot (1 - f_1)}{f_1 \cdot (1 - f_2)} = \exp[(\Delta E_F - E_{21})/kT] \quad (2.4)$$

This relation reveals that the stimulated emission rate will be larger than the absorption rate only when:

$$E_{F_c} - E_{F_v} \equiv \Delta E_F > E_{21} \quad (2.5)$$

In other words, the net stimulated emission rate, and hence the optical gain, will become positive only when the quasi-Fermi level separation is greater than the photon energy of interest. And because the photon energy must at least be equal to the band-gap energy, to achieve gain in a semiconductor one must have:

$$\Delta E_F > E_g \quad (2.6)$$

This condition demands that the voltage across a p-n junction must be greater than the band-gap to achieve gain in the active region.

In order to fully quantify these transition rates, one needs to evaluate the radiative transition rate R_r . This can be estimated using Fermi's Golden Rule:

$$R_r = \frac{2\pi}{\hbar} \cdot |M|^2 \cdot \rho(\hbar\omega) \quad (2.7)$$

where \mathbf{M} is the matrix element, and $\rho(\hbar\omega)$ is the density of states. The matrix element determines the strength of the interaction between the two states. This interaction can be strong, negligible or identically zero, all depending on the wavefunctions describing the two electron states. In the case of a QW, only transitions between subbands with the same quantum number are allowed, all others are forbidden. The wavefunction overlap also leads to the \mathbf{k} -selection rule, which dictates that transitions between planewave states are forbidden unless the \mathbf{k} -vectors of the two states are equal (the two electron states must propagate along the same direction). The matrix element represents the spatial overlap of the initial and final electron wavefunctions with the perturbation Hamiltonian:

$$M = \langle f | H' | i \rangle = \langle \psi_2 | H' | \psi_1 \rangle = \int \psi_2^* \cdot H'(\vec{r}) \cdot \psi_1 \cdot d^3\vec{r} \quad (2.8)$$

The electron wavefunctions are written as the product of two functions:

$$\psi = F(\vec{r}) \cdot u(\vec{r}) \quad (2.9)$$

The envelope function $F(\vec{r})$ is a slowly varying function that satisfied Schrödinger's equation using the macroscopic potential and the appropriate effective mass. The Bloch function, $u(\vec{r})$, is a complex periodic function which satisfies Schrödinger's equation using the atomic scale potential. Each energy band in the crystal has its own Bloch function. But one never needs to determine the Bloch functions precisely as only their symmetry properties are necessary for most calculations.

In uniformly doped bulk material, the envelope function takes the following form:

$$F(\vec{r}) = \frac{1}{\sqrt{V}} \cdot e^{-j\vec{k}\cdot\vec{r}} \quad (2.10)$$

while for the QW:

$$F(\vec{r}) = \frac{1}{\sqrt{A}} \cdot F(z) \cdot e^{-j\vec{k}\cdot\vec{r}_\parallel} \quad (2.11)$$

and for the quantum wires:

$$F(\vec{r}) = \frac{1}{\sqrt{L}} \cdot F(x, y) \cdot e^{-j\vec{k}\cdot\vec{r}} \quad (2.12)$$

where V (A , L) is the volume (area, length) of the crystal, and appears for normalization purposes.

The perturbation Hamiltonian is given by:

$$H'(\vec{r}) = -\vec{p}_e \cdot \vec{E}_{photon} = -\left(-e \cdot \vec{r}\right) \cdot \left(\vec{E}_0 \cdot e^{\pm i\vec{k}\cdot\vec{r}}\right) = e\vec{r} \cdot \vec{E}_0 e^{\pm i\vec{k}\cdot\vec{r}} \quad (2.13)$$

so the matrix element:

$$\begin{aligned}
M &= \frac{e}{A} \cdot \int F_2^* u_2^* \cdot \left(\vec{r} \cdot \vec{E}_0 e^{\pm i \vec{k} \cdot \vec{r}} \right) \cdot F_1 u_1 \cdot d^3 \vec{r} = \\
&= \frac{e}{A} \cdot \left[\int u_2^* u_1 \cdot F_2^* \cdot \left(\vec{r} \cdot \vec{E}_0 e^{\pm i \vec{k} \cdot \vec{r}} \right) \cdot F_1 \cdot d^3 \vec{r} + \int [F_2^* F_1] \cdot u_2^* \cdot \left(\vec{r} \cdot \vec{E}_0 e^{\pm i \vec{k} \cdot \vec{r}} \right) \cdot u_1 \cdot d^3 \vec{r} \right]
\end{aligned} \tag{2.14}$$

In transitions from the conduction band to the valence band, the first integral within the brackets vanished because of the orthogonality between the Bloch functions and due to the fact that the other terms in the integrand are, to a good approximation, constant in any one unit cell. To evaluate the second integral we break up the integration over the crystal volume into a sum of integrations over each unit cell. The terms in the square brackets in the second integral can be considered constant over one unit cell, and one can write:

$$M = \frac{e}{A} \cdot \sum_j [F_2^* F_1]_{r=r_j} \cdot \int_{\text{unit cell}} u_2^* \cdot \left(\vec{r} \cdot \vec{E}_0 e^{\pm i \vec{k} \cdot \vec{r}} \right) \cdot u_1 \cdot d^3 \vec{r} \tag{2.15}$$

where j sums over all unit cells in the crystal and \mathbf{r}_j is the position vector to the j th cell. Because the Bloch functions repeat themselves in each unit cell, the integral can be pulled out of the summation to obtain:

$$\begin{aligned}
M &= \frac{e}{A} \cdot \left[\frac{1}{A_{uc \text{ unit cell}}} \int u_2^* \cdot \left(\vec{r} \cdot \vec{E}_0 e^{\pm i \vec{k} \cdot \vec{r}} \right) \cdot u_1 \cdot d^3 \vec{r} \right] \cdot \sum_j [F_2^* F_1]_{r=r_j} \cdot A_{uc} = \\
&= \frac{e}{A} \cdot \langle u_2 | H' | u_1 \rangle \cdot \int_A F_2^* F_1 \cdot d^3 \vec{r} = \frac{e}{A} \cdot \langle u_2 | H' | u_1 \rangle \cdot \langle F_2 | F_1 \rangle
\end{aligned} \tag{2.16}$$

where, by assuming the volume of a unit cell to be very small, we have converted the summation over all unit cells back into an integral, using Dirac notation to express Bloch function overlap integral. The first component of the transition matrix element $\langle u_2 | H' | u_1 \rangle$ contains the polarization dependence of the interaction which will depend on the particular symmetries of the conduction and valence band Bloch functions. Aside from the polarization dependence (which can be a function of the photon energy), this momentum matrix element can be considered constant for a given material. (Coldren)

In addition to creating polarization sensitivity, the transition matrix element also restricts the types of states which can interact. We saw the envelope functions in a QW. Transitions between two such QW states are governed by the following overlap:

$$\begin{aligned}
\langle F_2 | F_1 \rangle &= \frac{1}{A} \cdot \int_V F_2^*(z) e^{j \vec{k}_2 \cdot \vec{r}_\parallel} \cdot F_1^*(z) e^{-j \vec{k}_1 \cdot \vec{r}_\parallel} \cdot d^3 \vec{r} = \\
&= \int_z F_2^*(z) F_1^*(z) \cdot d^3 \vec{r}
\end{aligned} \tag{2.17}$$

, with $\mathbf{k}_2 = \mathbf{k}_1$

Thus one can assume \mathbf{k} -selection in the plane of the QW, but still needs to evaluate $\left| \langle F_2 | F_1 \rangle \right|^2$ perpendicular to the plane, where again F_2 and F_1 are simply the particle in a box envelope functions

found for the quantized energy levels of the QW in both conduction and valence bands. Due to orthogonality between the QW wavefunctions solutions, the overlap integral reduces to the following rule for subband transitions:

$$\left| \langle F_2 | F_1 \rangle \right|^2 \approx \delta_{n_c, n_v} \quad (2.18)$$

Transitions can only occur between QW subbands which have the same quantum number, $n_c = n_v$. These are the allowed transitions. Transitions between subbands with dissimilar quantum numbers are forbidden transitions. The “nearly equal to” sign in the relation above is used because the different effective mass and barrier height in the conduction and valence bands means that the wavefunctions of the two bands are not completely orthogonal to each other. Nevertheless, allowed transitions overlaps are usually close to unity and forbidden transition overlaps are usually very small.

Next item to be explicated is the density of states.

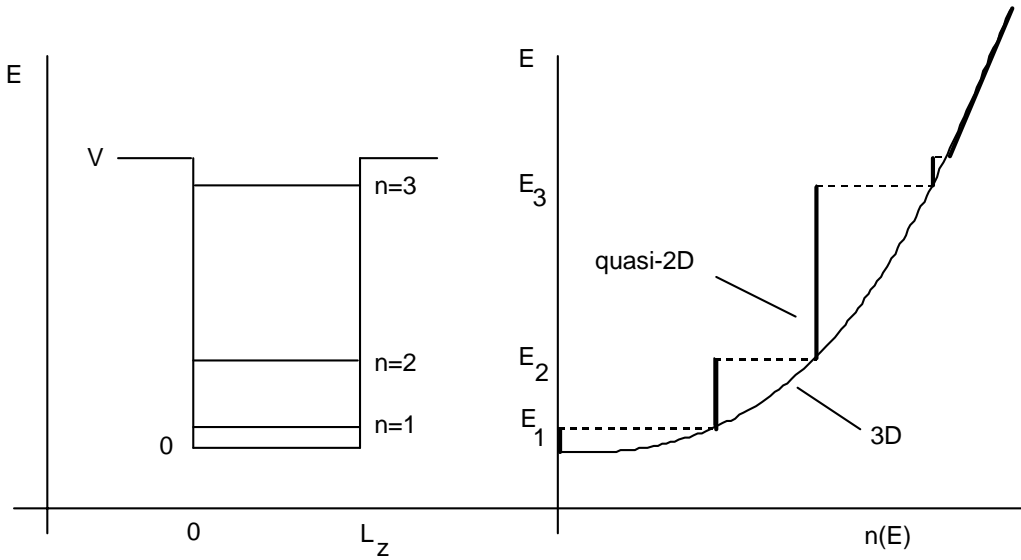


Figure 2.4: Schematic of the density of states for a QW and for bulk material.

The derivation of Fermi’s Golden Rule assumes that the electron initially occupies a single state which makes a transition to one of a large number of final states. In a semiconductor, both initial and final states of the electron are immersed within a large number of nearby states. For this case, the final density of states that appears in the expression of the radiative transition rate should be actually interpreted as the density of the transition pairs per unit transition energy. This density of transition pairs is referred to as the joint density of states. Taken into account the discrete energy levels in a QW, the corresponding joint density of states can be determined as:

$$\rho(E) = \frac{1}{d_x} \cdot \sum_n \frac{m^*}{\pi \hbar^2} \cdot H(E - E_n) \quad (2.19)$$

where H is the Heaviside unit step function.

2.4 Confinement of carriers and photons in diode lasers: the double heterostructure edge emitting laser

In the following sections we will describe the operating principles of the double heterostructure lasers, using as an example the double heterostructure edge-emitting laser. The discussion is essentially the same for VCSELS and we will underline each significant difference between the two types of devices. As shown in the figure below, we chose to designate always the optical propagation axis as the z -axis. In both cases the lateral y direction is in the plane of the substrate. For edge-emitting the vertical to the substrate is the transverse x direction while for VCSELS the x direction lies in the plane as a second lateral direction.

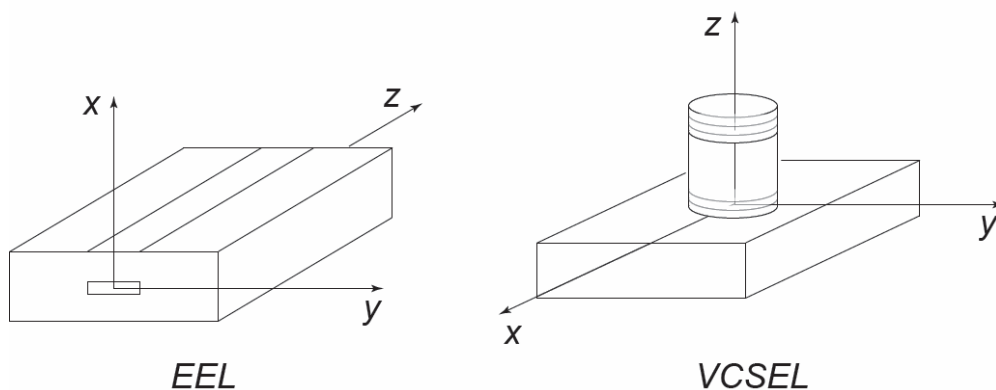


Figure 2.5: Schematic of in-plane and vertical-cavity surface emitting lasers showing selected coordinate systems

In order for the gain material in a semiconductor laser to function, it must be pumped or excited with some external energy source. A major attribute of diode lasers is their ability to be pumped directly with an electrical current. The active material can also be excited by the carriers generated from absorbed light, but we shall focus mainly on direct current injection technique.

Figure 2.6 gives a schematic of a broad area p-i-n double heterostructure (DH) laser diode, along with the transverse sketches of the energy gap, index of refraction and resulting optical mode across the DH region. A thin slab of active material is sandwiched between p - and n -type cladding layers which have a higher conduction-valence band energy gap. Because the bandgap of the cladding layer is larger, light generated in the active region will not have sufficient photon energy to be absorbed in them, i.e., $E_{21} = h\nu < E_{gcl}$.

For this DH, a transverse (x -direction) potential well is formed for electrons and holes that are being injected from the n - and p -type regions, respectively, under forward bias. They are captured and confined together, thereby increasing their probability of recombining. Unlike most semiconductor diodes or transistors used in purely electronic circuits, it is desirable to have all the injected carriers recombine in the active region to form photons in a laser or LED. A good assumption for lasers and LEDs is that all carriers recombine in the central i -region [2]. Nevertheless, there is a “leakage

current” which results from some of the carriers being thermionically emitted over the heterobarriers before they can recombine.

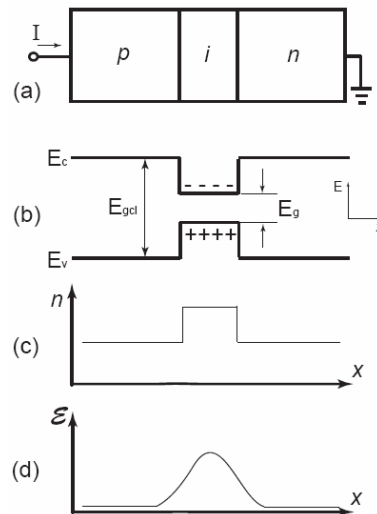


Figure 2.6: Aspects of the double-heterostructure diode laser: (a) schematic of the material structure; (b) energy diagram of the conduction and valence bands vs. transverse distance; (c) the refractive index profile; (d) the electric field profile for a mode traveling in the z direction.

To form the necessary resonant cavity for optical feedback, simple cleaved facets can be used due to the large index of refraction discontinuity at the semiconductor-air interface. The lower bandgap active region has a higher index of refraction, n , than the cladding, so that a transverse dielectric optical waveguide is formed with its axis along the z -direction. The resulting transverse optical energy density profile (proportional to the photon density or the electric field magnitude squared, $|\vec{E}|^2$) is illustrated in Figure 2.6(d). Thus, with the in-plane waveguide and perpendicular mirrors at the end, a complete resonant cavity is formed. More complex reflectors – the so-called distributed Bragg reflectors (DBR) – that can provide stronger feedback and wavelength selective feedback are used in VCSEL structures but in a vertical geometry as shown in Chapter 1.

The carrier-confining effect of the DH is one of the most important features in modern diode lasers. Many modern diode lasers have added complexity in their transverse carrier and photon confinement structure as compared to Figure 2.6, but the fundamental concepts remain valid. For example, in the case of in-plane lasers, where the light propagates parallel to the substrate surface, a common procedure is to use a thinner *quantum-well* (QW) carrier confining active region ($d \sim 10$ nm), and a surrounding intermediate bandgap *separate confinement* region to confine the photons. Figure 2.7 illustrates transverse bandgap profiles for such SCH, single QW lasers. The transverse optical energy density is also overlaid to show that the photons are confined primarily by the outer heterointerfaces and the carriers by the inner QW.

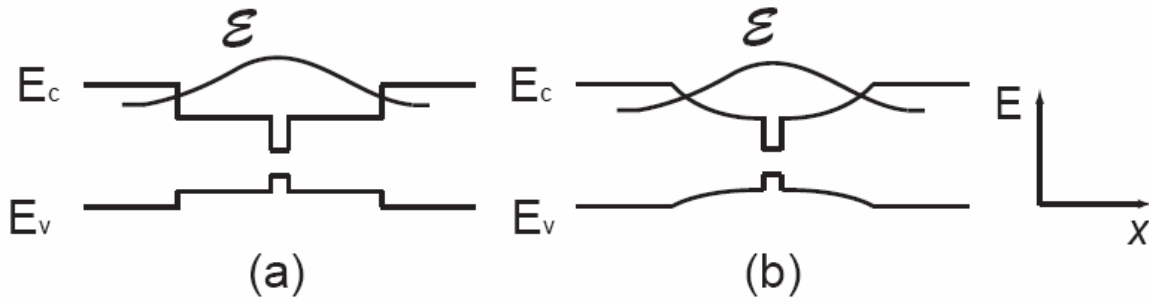


Figure 2.7: Transverse band structures for two different separate-confinement heterostructures (SCHs): (a) standard SCH; (b) graded-index SCH (GRINSCH). The electric field (photons) is confined by the outer step or graded heterostructure; the central QW confines the carriers.

2.5 Carrier generation and recombination in active regions

We will present a rate-equation model for the diode laser starting from simple, intuitive arguments. In a similar way, in Chapter 4, a rate equation model will be developed for coupled-cavity VCSELS.

As already mentioned, we consider the current injected into the terminals of a diode laser or LED. It is desirable to have all electrons and holes recombine in the active region. However, only a fraction, η_i , of the injected current, I , does contribute to such carriers. In Figure 2.8 we illustrate the process of carrier injection into a double heterostructure active region. Let us define the following notions:

Active region: the region where recombining carriers contribute to useful gain and photon emission.

The active region is usually the lowest bandgap region within the depletion region of a *pin* diode for efficient injection. Occasionally, it is convenient to include some of the surrounding intermediate bandgap regions. But there may be photon emission and even gain at some undesired wavelength elsewhere in the device.

Injection efficiency, η_{inj} : the fraction of terminal current that generates carriers in the active region.

The definition includes all the carriers that are injected into the active region, not just the carriers that recombine radiatively at the desired transition energy.

Only undoped or lightly doped active regions will be considered, so that under high injection levels relevant to LEDs and lasers, charge neutrality dictates that the electron density equals the hole density in the active region.

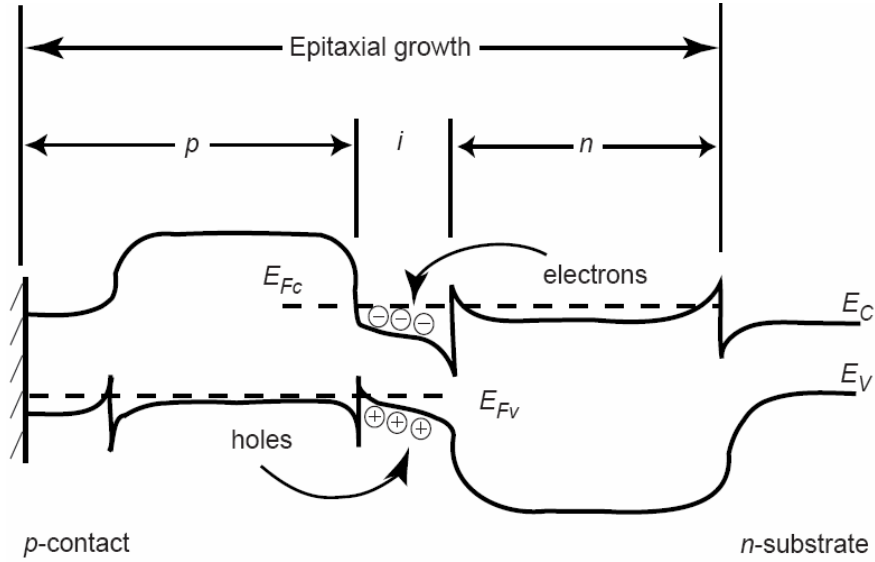


Figure 2.8: Band diagram of forward biased double heterostructure diode.

The carrier density in the active region is governed by a dynamic process. We will use a reservoir model in order to illustrate it, schematically shown in Figure 2.9. To insure particle conservation, each arrow represents the number of particles flowing per unit time. The rates per unit volume and the densities are multiplied by the active region volume V of the carrier reservoir or the mode volume V_p of the photon reservoir.

Starting with the carrier reservoir, we have the rate of carrier injection into the laser I/q . Of these carriers only $\eta_{inj}I/q$ reach the active region, where η_{inj} is the injection efficiency. The rest recombine elsewhere in the device. Some carriers in the carrier reservoir recombine via non-radiative recombination at the rate $R_{nr}V$. Others recombine spontaneously at the rate $R_{sp}V$, of which a certain fraction emit photons into the mode of interest at the rate $R'_{sp}V$ (or $\beta_{sp}R_{sp}V$ where β_{sp} is the spontaneous emission factor). Other carriers recombine via stimulated emission into the mode of interest at the rate $R_{21}V$. Some carriers might leak out from the active region via lateral diffusion and/or thermionic emission at the rate R_lV . Since this is often negligible we will include it in the non-radiative recombination process.

In the photon reservoir, the stimulated and spontaneous emission rates into the mode provide the necessary generation of photons at the rate $R_{21}V + \beta_{sp}R_{sp}V$. Absorption in the active region depletes photons at the rate $R_{12}V$. All other photons leave the cavity at the rate N_pV_p/τ_p , where τ_p represents the photon lifetime. Only $\eta_0N_pV_p/\tau_p$ of the photons leave through the desired mirror to be collected as useful output power, P_0 , where η_0 is the optical extraction efficiency of the laser. The rest of the photons exit the cavity through a different mirror or disappear through: (1) free carrier absorption in the active region, (2) absorption in materials outside the active region, and/or (3) scattering at rough surfaces.

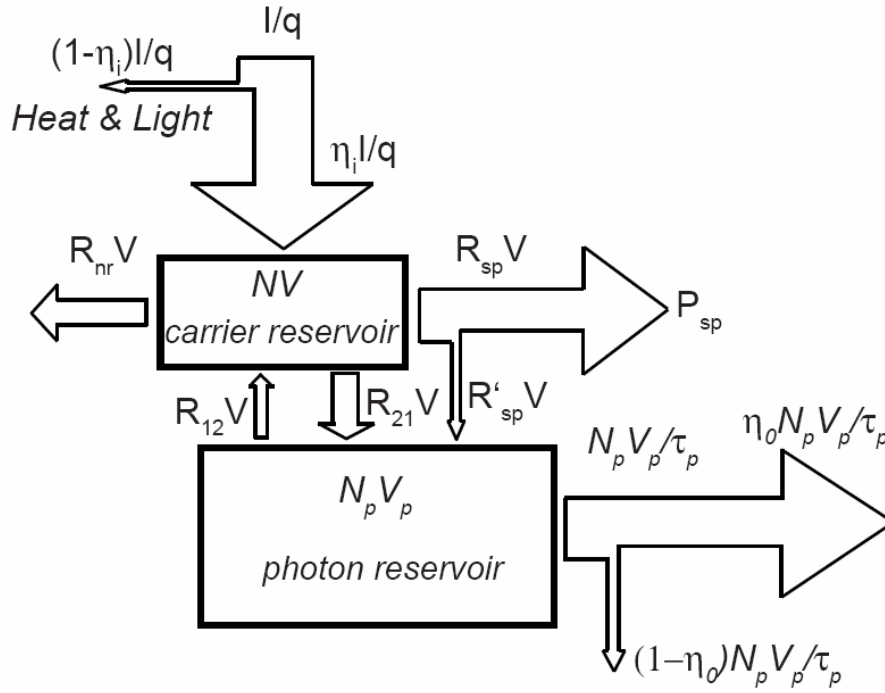


Figure 2.9: Reservoir model used for DH active region.

For the DH active region, the injected current provides a generation term, and various radiative and non-radiative recombination processes as well as carrier leakage provide recombination terms. Thus, we can write the rate equation:

$$\frac{dN}{dt} = G_{gen} - R_{rec} \quad (2.20)$$

where G_{gen} is the rate of injected electrons and R_{rec} is the rate of recombining electrons per unit volume in the active region. Since there are $\eta_i I/q$ electrons per second being injected into the active region:

$$G_{gen} = \frac{\eta_i I}{qV} \quad (2.21)$$

where V is the volume of the active region, i.e. the volume of the quantum wells in the QW laser.

Several mechanisms must be considered for the recombination process. There is a spontaneous recombination rate, R_{sp} , and a non-radiative recombination rate, R_{nr} . Sometimes, a carrier leakage rate, R_l , must be included if the transverse and/or lateral potential barriers are not sufficiently high. Thus we can write for the total recombination rate:

$$R_{rec} = R_{sp} + R_{nr} + R_l + R_{st} \quad (2.22)$$

The first three terms on right hand side refer to the natural or unstimulated carrier decay processes. The fourth one, R_{st} , representing the stimulated recombination rate, depends on the photon density. It is common to describe the natural decay processes by a *carrier lifetime*, τ . In the absence of photons or a generation term, the rate equation for carrier decay is just, $dN/dt = N/\tau$, where $N/\tau \equiv R_{sp} + R_{nr} + R_l$. This rate equation defines τ . We can rewrite:

$$R_{rec} = \frac{N}{\tau} + R_{st} \quad (2.23)$$

The carrier rate equation may be expressed as:

$$\frac{dN}{dt} = \frac{\eta_i I}{qV} - \frac{N}{\tau} - R_{st} \quad (2.24)$$

In the absence of a large photon density, such as in a laser well below threshold or in most LEDs, it can be shown that R_{st} can be neglected.

2.6 Photon generation and loss in laser cavities

For the diode laser we must now further investigate the nature of the net stimulated recombination rate, R_{st} , in generating photons as well as the effect of the resonant cavity in storing photons. We construct a rate equation for the photon density, N_p , which includes the photon generation and loss terms. The variables indicating the photons will be designed with the subscript p .

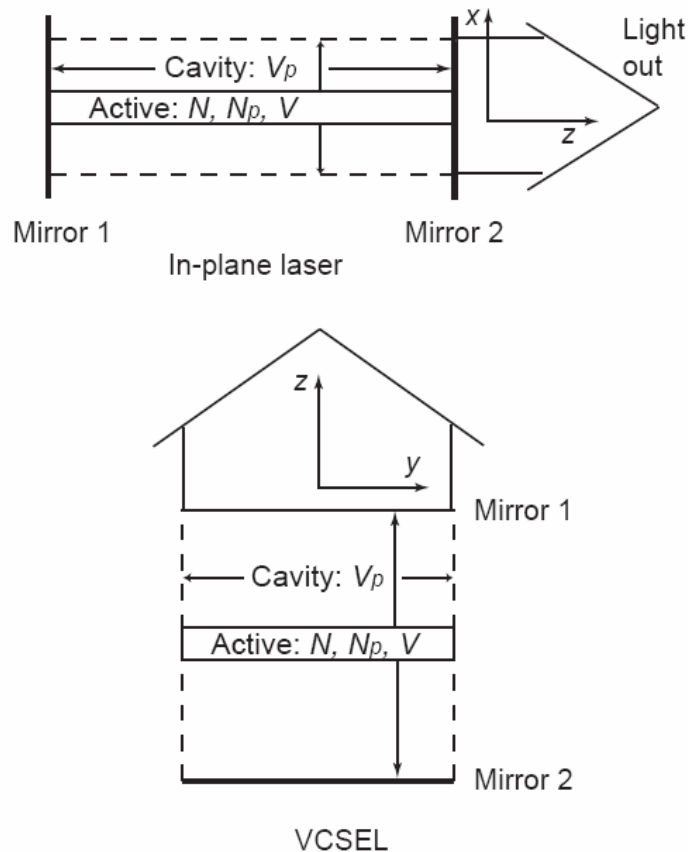


Figure 2.10: Schematics of in-plane and vertical-cavity lasers showing the active and cavity volumes.

A main difference between a laser and a LED is that one has to consider the light emission only into a single mode of the resonant cavity in the laser. Since there are typically thousands of possible optical modes in an edge emitting diode laser cavity situated within the gain window, only a small fraction of R_{sp} contributes for the photon generation rate into a particular mode. It is worth

mentioning that in a vertical cavity laser the number of the effective modes can be much fewer, typically from one to dozens rather than thousands.

The main photon generation term above threshold (the regime of interest in lasers) is R_{st} . Every time an electron-hole pair is stimulated to recombine, another photon is generated. As indicated in Figure 2.10, since the cavity volume occupied by photons, V_p , is usually larger than the active region volume occupied by electrons, V , the photon density generation rate will be $(V/V_p)R_{st}$, instead of R_{st} . We will refer to this ratio, $\Gamma=V/V_p$, as the electron-photon overlap factor. Sometimes it is convenient to introduce an effective thickness, width and length that contain the photons, d_{eff} , w_{eff} , and L , respectively. That is, $V_p=d_{eff}w_{eff}L$. Then, if the active region has dimensions, d , w , and L_a , the electron-photon overlap factor can be expressed as $\Gamma=\Gamma_x\Gamma_y\Gamma_z$, where $\Gamma_x=d/d_{eff}$, $\Gamma_y=w/w_{eff}$, and $\Gamma_z=L_a/L$. We will show that, putting the derivation of Γ on a more rigorous foundation, this is subject to an enhancement factor, the so-called *standing-wave enhancement factor* for $L_a \lambda$.

Photon loss occurs within the cavity due to optical absorption and scattering out of the mode, and it also occurs at the output coupling mirror where a portion of the resonant mode is usefully coupled to some output medium. The net loss will be characterized by the photon (or cavity) lifetime, τ_p , analogous to how we handled electron losses above. A first version of the photon rate equation takes the form:

$$\frac{dN_p}{dt} = \Gamma \cdot R_{st} + \Gamma \cdot \beta_{sp} \cdot R_{sp} - \frac{N_p}{\tau_p} \quad (2.25)$$

where β_{sp} is the *spontaneous emission factor*. In the absence of generation terms, the photons decay exponentially with a decay constant of τ_p .

Equations (2.24) and (2.25) are two coupled equations that can be solved for the steady-state and dynamic responses of a diode laser. However, there are still several terms that need to be written explicitly in terms of N and N_p before such solutions are possible.

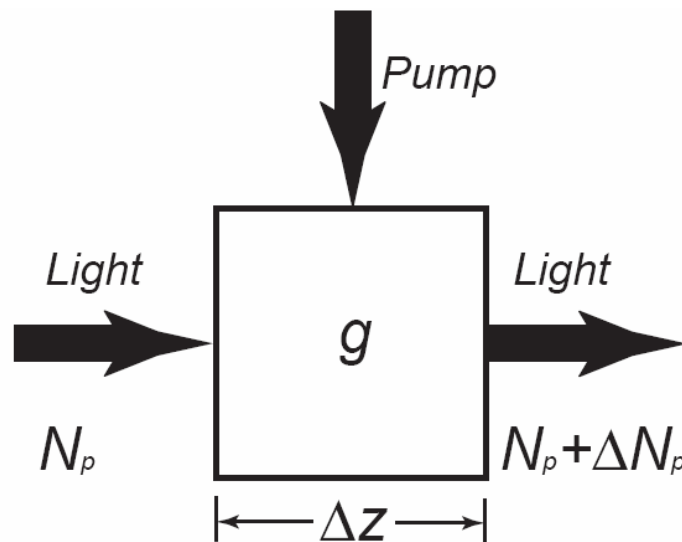


Figure 2.11: Definition of gain in terms of the increase in photon number across a small segment of gain material

R_{st} represents the photon stimulated net electron-hole recombination rate which generates more photons. This is a *gain* process for photons. In Figure 2.11 we show the growth of a photon density from an incoming value of N_p to an existing value of $N_p + \Delta N_p$ as it passes through a small length, z , of active region. Without loss of generality we assume full overlap between the active region and the photon field, i.e. $V/V_p = 1$. So we describe this growth in terms of a *gain per unit length*, g :

$$N_p + \Delta N_p = N_p \cdot e^{g \cdot \Delta z} \quad (2.26)$$

If z is sufficiently small, $\exp(g \cdot z) \approx (1 + g \cdot z)$. Also using the fact that $z = v_g \cdot t$, where v_g is the group velocity, we find that, $\Delta N_p = N_p g v_g t$. That is, the generation term for the dN_p/dt is given by:

$$\left(\frac{dN_p}{dt} \right)_{gen} = R_{st} = \frac{\Delta N_p}{\Delta t} = v_g \cdot g \cdot N_p \quad (2.27)$$

Thus, we can now rewrite the carrier and photon density rate equations:

$$\frac{dN}{dt} = \frac{\eta_i I}{qV} - \frac{N}{\tau} - v_g \cdot g \cdot N_p \quad (2.28)$$

$$\frac{dN_p}{dt} = \Gamma \cdot v_g \cdot g \cdot N_p + \Gamma \cdot \beta_{sp} \cdot R_{sp} - \frac{N_p}{\tau_p} \quad (2.29)$$

The simplest approximation of the gain as a function of the carrier density is a straight line, at least under small signal conditions. That is:

$$g \approx a \cdot (N - N_{tr}) \quad (2.30)$$

where a is the *differential gain*, g/N , and N_{tr} is a *transparency carrier density*. More complicated functions, typically logarithmic approximations, fit the gain better over a wider range of N .

2.7 Threshold or steady-state gain in lasers

We characterized the cavity loss by the photon decay constant or lifetime, τ_p . We will explicitly express τ_p in terms of the losses associated with optical propagation along the cavity and the cavity mirrors. Also, we will show that the net loss of some mode gives the value of the net gain required to reach the lasing threshold.

The optical energy of a diode laser propagates in a dielectric waveguide mode which is confined both transversally and laterally as defined by a normalized transverse electric field profile, $U(x, y)$. In the axial direction this mode propagates as $\exp(-j\beta^* z)$, where β^* is the complex propagation constant which includes any loss or gain. Thus, the time- and space-varying electric field can be written as:

$$\vec{E} = \vec{e}_y \cdot E_0 \cdot U(x, y) \cdot e^{j(\omega t - \beta^* z)} \quad (2.31)$$

where the \vec{e}_y is the unit vector indicating the TE polarization and E_0 is the magnitude of the field. Similar equations apply for the TM polarized mode. The complex propagation constant, β^* , includes the incremental *transverse modal gain*, $\langle g \rangle_{xy}$ and *internal modal loss*, $\langle \alpha_i \rangle_{xy}$. That is:

$$\beta^* = \beta + j \cdot \beta_i = \beta + \frac{j}{2} \cdot (\langle g \rangle_{xy} - \langle \alpha_i \rangle_{xy}) \quad (2.32)$$

where the real part of β^* , $\beta = 2\pi\bar{n}/\lambda$, and \bar{n} is an effective index of refraction for the mode. The transverse modal gain, $\langle g \rangle_{xy}$, and loss, $\langle \alpha_i \rangle_{xy}$, are found from weighted averages of the gain and loss, respectively, across the mode shape, $U(x, y)$. We can let $\langle g \rangle_{xy} = \Gamma_{xy} \cdot g$, where Γ_{xy} is the transverse confinement factor, if $g(x, y)$ is constant across the active region and zero elsewhere. This is generally valid for in-plane lasers, but not for VCSELS. Also, for notational convenience we shall let $\langle \alpha_i \rangle_{xy} = \alpha_i$.

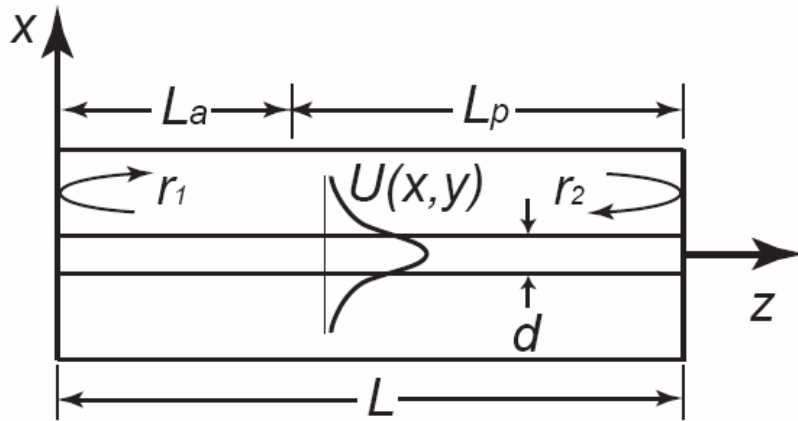


Figure 2.12: Generic laser cavity cross section showing active and passive sections and the guided mode profile.

As illustrated in Figure 2.12, most laser cavities can be divided into two general sections: an active section of length L_a and a passive section of length L_p . Also, g and α_i will be different in these two sections. In the passive section, by definition $g=0$, and α_i can be given a second subscript to designate its location. The propagating mode is reflected by end mirrors, which have amplitude reflection coefficients r_1 and r_2 , respectively, to provide a resonant cavity. The amount transmitted is potentially useful output.

In order for a mode of the laser to reach the threshold, the gain in the active section must be increased to the point where all the propagation and mirror losses are compensated, so that the electric field exactly replicates itself after one round trip in the cavity. Equivalently, we can unfold the round trip along the z -axis and require that $\vec{E}(z=2L) = \vec{E}(z=0)$ provided we insert the mode reflection coefficients at $z=0$ and $z=L$. As a consequence of considering these boundary conditions we obtain:

$$r_1 \cdot r_2 \cdot e^{-2 \cdot j \cdot \beta_{a,th}^* \cdot L_a} \cdot e^{-2 \cdot j \cdot \beta_{p,th}^* \cdot L_p} = 1 \quad (2.33)$$

The subscript *th* denotes that this characteristic equation only defines the threshold value of β^* . We can break the previous complex equation into two equations for its magnitude and phase. For the magnitude:

$$r_1 \cdot r_2 \cdot e^{(\Gamma_{xy} \cdot g_{th} - \alpha_{i,a}) \cdot L_a} \cdot e^{-2 \cdot \alpha_{i,p} \cdot L_p} = 1 \quad (2.34)$$

Solving for $\Gamma_{xy} \cdot g_{th} \cdot L_a$ we obtain:

$$\Gamma_{xy} \cdot g_{th} \cdot L_a = \alpha_{i,a} \cdot L_a + \alpha_{i,p} \cdot L_p + \ln\left(\frac{1}{R}\right) \quad (2.35)$$

where we defined the mean mirror intensity reflection coefficient, $R=r_1 r_2$. Dividing by the total cavity length, L , and defining the average internal loss $\alpha_{i,a} \cdot L_a + \alpha_{i,p} \cdot L_p = \langle \alpha_i \rangle$, we have:

$$\langle g \rangle_{th} = \Gamma \cdot g_{th} = \langle \alpha_i \rangle + \frac{1}{L} \cdot \ln\left(\frac{1}{R}\right) \quad (2.36)$$

For convenience, the mirror loss term is sometimes abbreviated as, $\alpha_m \equiv (1/L) \ln(1/R)$. Noting that the photon decay rate, $1/\tau_p = 1/\tau_i + 1/\tau_m = v_g \cdot (\langle \alpha_i \rangle + \alpha_m)$, we can also write:

$$\Gamma \cdot g_{th} = \langle \alpha_i \rangle + \alpha_m = \frac{1}{v_g \cdot \tau_p} \quad (2.37)$$

For the phase part, $\exp(2j\beta_{th,a}L_a)\exp(2j\beta_{th,p}L_p)=1$, requires that $\beta_{th,a}L_a + \beta_{th,p}L_p = m\pi$, which gives a condition on the modal wavelength:

$$\lambda_{th} = \frac{2}{m} \cdot \left[\bar{n}_a \cdot L_a + \bar{n}_p \cdot L_p \right] \quad (2.38)$$

where m is the longitudinal mode number. \bar{n} is the refractive index which varies with wavelength (dispersion), and the carrier density (plasma loading). That is, to determine \bar{n} at a wavelength $\lambda = \lambda_0 + \Delta\lambda$ and a carrier density $N = N_0 + \Delta N$, we use:

$$\bar{n}(\lambda, N) = \bar{n}(\lambda_0, N_0) + \frac{\partial \bar{n}}{\partial \lambda} \cdot \Delta\lambda + \frac{\partial \bar{n}}{\partial N} \cdot \Delta N \quad (2.39)$$

one can find the wavelength separation between two modes, m and $m+1$:

$$\delta\lambda = \frac{\lambda^2}{2 \cdot \left(\bar{n}_{ga} \cdot L_a + \bar{n}_{gp} \cdot L_p \right)} \quad (2.40)$$

where the group effective index for the j th section, $\bar{n}_{gj} = \bar{n}_j - \lambda \cdot (\partial \bar{n} / \partial \lambda) = \bar{n}_j + \omega \cdot (\partial \bar{n} / \partial \omega)$.

Finally, it is important to note that the steady-state gain in a laser operating above threshold must also equal its threshold value. That is, in a laser cavity:

$$g(I > I_{th}) = g_{th} \quad (\text{steady state}) \quad (2.41)$$

If the gain were higher than g_{th} , then the field amplitude would continue to increase without bound, and this clearly cannot exist in the steady state. Furthermore, since the gain is monotonically related to the carrier density, this implies that the carrier density must also clamp at its threshold value. That is:

$$N(I > I_{th}) = N_{th} \quad (\text{steady state}) \quad (2.42)$$

When the current is increased to a value above the threshold the carrier density and gain initially (for on the order of a nanosecond) increase to values above their threshold levels, and the photon density grows. But then, the stimulated recombination term also increases reducing the carrier density and gain until a new steady-state dynamic balance is reached. One can also reformulate saying that the stimulated recombination term uses up all additional carrier injection above threshold.

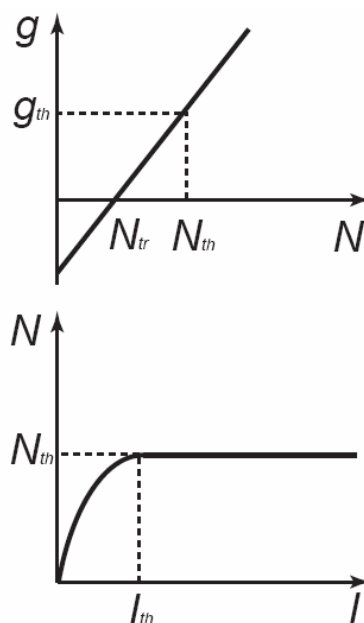


Figure 2.13: Gain vs. carrier density and carrier density vs. input current. The carrier density clamps at threshold causing the gain to clamp also.

Figure 2.13 summarizes the carrier clamping effect in a laser cavity. The physics of g vs. N curve never changes. The feedback effect causes the carrier density to clamp, in order to keep the gain at its threshold value.

2.8 Relative confinement factor

We will present now a few problems specific to VCSEL devices, namely the confinement factor and the distributed Bragg reflectors (DBRs), according to reference [3]. Figure 2.14 shows the layer structure and the standing wave pattern of the electric field in the inner part of a VCSEL cavity realized in the AlGaAs material system. Analogously with a simple Fabry-Pérot type EEL with its mirrors composed of abrupt semiconductor-air interfaces, maxima of the electric field amplitude are

found at both ends of the inner cavity of length L . With a positive integer m and the spatially averaged refractive index $\langle \bar{n} \rangle$, the resonance condition for the emission wavelength λ is then simply written as:

$$\langle \bar{n} \rangle \cdot L = m \cdot \frac{\lambda}{2} \quad (2.43)$$

The active layers have to be placed in an anti-node of the standing-wave pattern in order to provide good coupling between electrons and photons. Since splitting of the active region into segments separated by $\lambda/(2 \cdot \langle \bar{n} \rangle)$ has to be avoided for reasons of carrier injection efficiency, the shortest symmetric cavity is just one wavelength thick, equivalent to $m=2$.

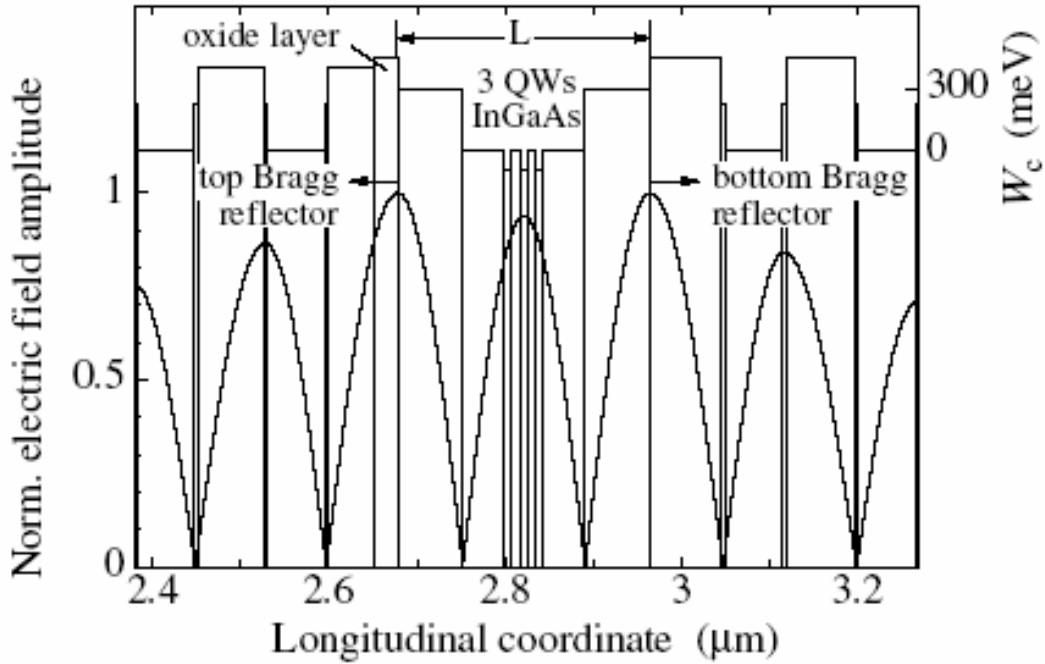


Figure 2.14: Spatial distribution of the normalized electric field amplitude squared in the center region of a VCSEL together with the conducting band edge W_c , neglecting band bending effects [3].

An important difference between a VCSEL cavity and a conventional EEL cavity arises from the fact that the active gain region does not extend over the full cavity length L but is typically limited to the thickness of the quantum well layers. Therefore, for an arbitrary position and total thickness d_a of the active layers, we have to take into account the overlap with the standing wave pattern in order to obtain the average gain in the cavity [4]. We define the relative confinement factor or gain enhancement factor by:

$$\Gamma_r = \frac{L}{d_a} \cdot \frac{\int_{d_a} |E(z)|^2 \cdot dz}{\int_L |E(z)|^2 \cdot dz} \quad (2.44)$$

imposing that for all further considerations the material gain coefficient g of the QWs has to be modified to $\Gamma_r g$. The electric field profile in the central $\lambda/(2 \cdot \langle \bar{n} \rangle)$ part of the cavity in Figure 2.14 is very well approximated by:

$$E(z) = E_0 \cdot \cos\left(2 \cdot \pi \cdot \langle \bar{n} \rangle \cdot z / \lambda\right) \quad (2.45)$$

if $z=0$ is centered in the inner cavity, resulting in:

$$\Gamma_r = 1 + \frac{\sin\left(2 \cdot \pi \cdot \langle \bar{n} \rangle \cdot d_a / \lambda\right)}{2 \cdot \pi \cdot \langle \bar{n} \rangle \cdot d_a / \lambda} \quad (2.46)$$

for a single gain segment. The gain enhancement factor for a perfectly aligned active layer is thus expressed as a raised-sinc function. For a thin QW we have $\Gamma_r \rightarrow 2$. For $d_a = m \cdot \lambda / (2 \cdot \langle \bar{n} \rangle)$, we obtain $\Gamma_r = 1$, as known for EELs.

2.9 Distributed Bragg reflectors

As discussed in the previous chapter, the Bragg reflectors consist in an alternating sequence of high and low refractive index layers with quarter wavelength thickness. Typically more than 20 Bragg pairs are required for each mirror. The reflectivity of a lossless DBR mirror calculated at the resonant (Bragg) wavelength is given by:

$$R = \left(\frac{1-b}{1+b}\right)^2 \quad (2.47)$$

where the b -parameter has a different expression for an even or an odd number of quarter wavelength layers:

$$b_{\text{even}} = \frac{n_{\text{out}}}{n_{\text{in}}} \cdot \left(\frac{n_1}{n_2}\right)^{2m} \quad (2.48)$$

$$b_{\text{odd}} = \frac{n_1^2}{n_{\text{in}} \cdot n_{\text{out}}} \cdot \left(\frac{n_1}{n_2}\right)^{2m}$$

n_{in} and n_{out} denote the index of refraction of the medium from which the wave is incident and into which the light is transmitted after the stack of layers, while n_1 and n_2 are the high and respectively low refractive indexes of the layers in the DBR.

To maintain the analogy with EELs, the first layer of the top or bottom mirror, as seen from the inner cavity, has to have a lower refractive index and higher bandgap than the neighboring carrier confinement layer. The requirement of an alternating index sequence then leads to an integer number of Bragg pairs for the top mirror of an AlGaAs-based VCSEL, whereas a single low-index quarter

wave layer adjacent to the high-index GaAs substrate has to be added to the bottom mirror. Here we assume that the top mirror is terminated by a low-index material such as air.

Another important parameter in the design of a DBR is the spectral reflectivity $R(\lambda)$ and the phase $\varphi_r(\lambda)$ (Figure 2.15). A broad spectral plateau of high reflectivity, often denoted as stop-band, appears around the Bragg wavelength λ_B , the width of which can be roughly estimated as [5,6]:

$$\Delta\lambda_{SB} \approx \frac{2 \cdot \lambda_B \cdot \overline{\Delta n_B}}{\pi \cdot \langle \overline{n_{gr}} \rangle} \quad (2.49)$$

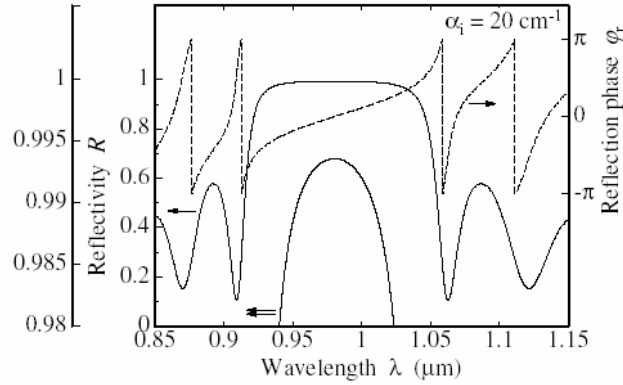


Figure 2.15: Wavelength dependence of the reflectivity R and of the phase φ_r for the lossy DBR; Detail of reflectivity dependence in the center of the stop-band [3].

The stop-band width is proportional to the refractive index step $\overline{\Delta n_B} = |\overline{n_1} - \overline{n_2}|$ which yields $\Delta\lambda_{SB} \approx 100nm$ for the GaAs-AlAs composition from Figure 2.15 with $\overline{\Delta n_B} = 0.56$ [7] and $\langle \overline{n_{gr}} \rangle \approx 3.6$ for the spatial average of the group index $\overline{n_{gr}} = \overline{n} - \lambda \cdot \frac{d\overline{n}}{d\lambda}$ at $\lambda_B = 980nm$.

For incidence from a high index material, the phase φ_r of the complex amplitude reflection coefficient $r = \sqrt{R} \cdot \exp(i \cdot \varphi_r)$ is zero at the Bragg wavelength but varies almost linearly with phase coefficient β . One can define the penetration depth in the Bragg stack, which in the approximation of a high reflectivity DBR is given by:

$$l_{eff} \approx \frac{\lambda_B}{4 \cdot \overline{\Delta n_B}} \quad (2.50)$$

This last result is obtained for high reflectivities [5]: $\sqrt{R} \approx 1$, which is the case for VCSELs. The slow variation of the penetration depth with the number of mirror pairs is plotted in the figure above and leads to $l_{eff} \approx 440nm$ for the considered mirror. It should be noted that a more rigorous treatment of Bragg mirror properties distinguishes between phase and energy penetration depths, which, however, turn out to be very similar for usual semiconductor mirrors with small index steps.

The total effective cavity length is finally determined as the sum of the cavity length and the penetration depths in the two Bragg reflectors:

$$L_{eff} = L + l_{eff,top} + l_{eff,bot} \quad (2.51)$$

Therefore the longitudinal mode spacing is given by:

$$\Delta\lambda_m \approx \frac{\lambda^2}{2 \cdot L_{eff} \cdot \langle n_{gr} \rangle} \quad (2.52)$$

A numerical application for $L_{eff} \approx 1.3\mu m$ yields $\Delta\lambda_m \approx 110nm$, extending far beyond the mirror stop-band and being even larger than the spectral gain bandwidth of the QW material. Therefore just a single longitudinal mode can oscillate in a VCSEL with a thin inner cavity. The spectral position of this mode can readily be theoretically or experimentally determined by localizing the sharp dip appearing in the reflectivity spectrum of the complete layer stack. However, depending on the lateral size of the VCSEL several transverse modes may oscillate simultaneously.

Bibliography CHAPTER 2

[1] L.A. Coldren and S.W. Corzine, “Diode Lasers and Photonic Integrated Circuits”, Wiley Series in Microwave and Optical Engineering, 1995.

[2] S. M. Sze, *Physics of Semiconductor Devices*, Wiley-Interscience, New York, 1981.

[3] R. Michalzik and K.J. Ebeling, *Operating Principles of VCSELS*, University of Ulm, Optoelectronics Department, D-89069, Germany.

[4] S.W. Corzine, R.S. Geels, J.W. Scott, R.-H. Yan, and L.A. Coldren, “Design of Fabry-Pérot surface-emitting lasers with a periodic gain structure”, *IEEE J. Quantum Electron.*, **25**, pp. 1513–1524 (1989).

[5] K.J. Ebeling, *Integrated Optoelectronics*, Berlin: Springer, 1993.

[6] P. Yeh, *Optical Waves in Layered Media*, New York: J. Wiley & Sons, 1988.

[7] S. Adachi, “GaAs, AlAs, and $Al_xGa_{1-x}As$: Material parameters for use in research and device applications”, *J. Appl. Phys.*, **58**, pp. R1–R29 (1985).

Chapter 3*

The coupled-cavity VCSEL (CC-VCSEL)

3.1 State of the art of coupled-cavity VCSELs

We have seen in the previous chapters that VCSELs are rapidly emerging as strong competitors to conventional edge-emitting semiconductor lasers as sources in short to medium haul optical communications systems. The circular output aperture of a typical VCSEL yields a well-behaved output beam that can be very tightly focused and efficiently coupled into optical fibre. Because VCSELs are typically batch-fabricated, with thousands of devices on a single wafer, they are mass-producible and potentially low cost. Furthermore, these surface-emitting lasers lend themselves naturally to the construction of two-dimensional (2-D) arrays. These devices are currently mass-produced for gigabit Ethernet over multimode fibre; in addition, they may be used for optical disk readout, as optical drivers for phased array radar or as a solution for the optical interconnect problem. Whatever final solution is used, increased sophistication is required for future generations of optoelectronic devices. For instance in the classical edge-emitting geometry, multisection lasers allow greater freedom of the lasing parameters such as bandwidth, wavelength tuning etc. than single section devices [1]. Moreover, devices with a lasing section and an absorbing section can perform a variety of logic functions. When one requires mode interaction between the different sections, multiple cavities need to be formed. Depending on the configuration, the cavities may be achieved by creating facets through etching or cleaving or by optically connecting the different sections via optical waveguides [2]. For many applications the device performances of EELs can be significantly improved through the use of multiple section devices. Cleaved coupled-cavity (C^3) lasers have already shown great promise as the interaction between the different mode spectra of each section can lead to single mode operation, wavelength tuning, high-speed switching, as well as the generation of short pulses via mode locking and Q switching [3]. VCSELs have made their way in the field of multisection devices too, since they offer many advantages over edge emitters which make them attractive for use in coupled cavity structures. These include monolithic growth of the coupled resonator, the ability to easily

* This chapter is based on the paper:

- V. Badilita, J.-F. Carlin, and M. Ilegems, "Lumped-mirror model for CC-VCSELs", to be submitted for *IEEE J. of Lightwave Technology*.

modify the amount of coupling and of course the ability to fabricate two-dimensional arrays. The monolithic integration of coupled resonators within a vertical cavity laser opens up new possibilities due to the unique ability to tailor the interaction between the cavities.

In contrast to EELs, the mirrors in VCSELs are monolithically integrated during growth in the form of dielectric mirrors. With this type of manufacturing it is easy to make twin section vertical cavity devices where the two sections are separated by a mirror whose reflectivity can be precisely controlled. It is just a matter of growth control to integrate two microcavities with a common mirror between them.

Coupled semiconductor microcavities were first investigated by Stanley et al. in 1994 [4]. The coupled semiconductor microcavity is a system in which there are three oscillators, two photonic and one electronic (quantum well oscillator). It develops three strongly coupled modes which allow a wide design range for a variety of optoelectronic applications.

Reflectance spectra of the two λ -sized cavities each containing three InGaAs quantum wells (QW) showed pronounced anticrossing effect due to the optical coupling between the two cavities. The separation of the resonant wavelengths depends on the coupling strength between the two cavities, i.e. the transmission T_0 of the common DBR. This work also gave evidence of an interesting regime for excitons at these high-Q microcavities, namely the existence of the cavity polariton. If the coupling of the cavity mode and the QW exciton is sufficiently strong, then this gives rise to a mixed exciton-photon state analogous to the exciton polariton of the bulk semiconductors. The resulting cavity polariton manifests itself as additional resonance in the reflectance spectrum [4].

Light emission in CC-VCSELs was first demonstrated by Pellandini et al. [5] with optically pumped devices. Depending on the detuning between the two cavities, the CC-VCSELs can operate on a single short or long wavelength mode, as well as on the two of them simultaneously. The structure is optically pumped at room temperature under quasi-cw conditions (1 μ s pulse, 5 kHz) above the GaAs bandgap using a tunable Ti-sapphire laser. Due to a wedge induced into each cavity, the detuning between the cavities can be continuously varied when moving across the sample. Input-output curves are shown in Figure 3.1. Such dual wavelength laser is of great interest for two-wavelength interferometry [6] or terahertz signal generation [7]. The role of the gain asymmetry in the CC-VCSEL structure in the process of achieving a stable dual wavelength operation has also been identified in reference [5]. At resonance, the system can no longer be considered as two separate lasers with independent gains because the optical fields are distributed over the whole system. The two optical modes supported in the structure are affected by both gain media in the two cavities, but these cavities are unequally pumped. It is this asymmetry in the two gain profiles that makes possible for dual lasing to occur. Since it is the same principle as in the structures investigated in this work, we will briefly explain the operating principle of the optically pumped coupled-cavity VCSEL: let us suppose that there is some gain for the long wavelength mode, but not sufficient to reach the threshold, while for the short wavelength mode there is gain in the top (shorter) cavity and absorption in the bottom

(longer) cavity. Light emitted on the short wavelength mode from the top gain medium is efficiently absorbed by the QWs located in the bottom cavity. That means that the short wavelength mode acts as an additional pump for the bottom gain medium. The pump will become very efficient when the gain is sufficient to cause lasing at the short wavelength mode. Through this internal pump mechanism, the bottom cavity gain increases until its value at long wavelength mode is large enough, when combined with the contribution from the gain in the top cavity, to initiate laser oscillation in the long wavelength mode. However, stimulated emission at the long wavelength mode will decrease the number of carriers in the top gain medium. Any resulting decrease in the laser emission at the short wavelength mode due to competition with the long wavelength mode for burning the same carriers in the top medium results in a weakening of the internal pump mechanism. Therefore, there will be in turn a decrease in power at long wavelength mode. Through this mechanism, a self-regulation is obtained, which prevents the onset of laser oscillation at long wavelength mode from turning off laser oscillation at short wavelength mode and makes the simultaneous laser emission at both wavelengths coupled.

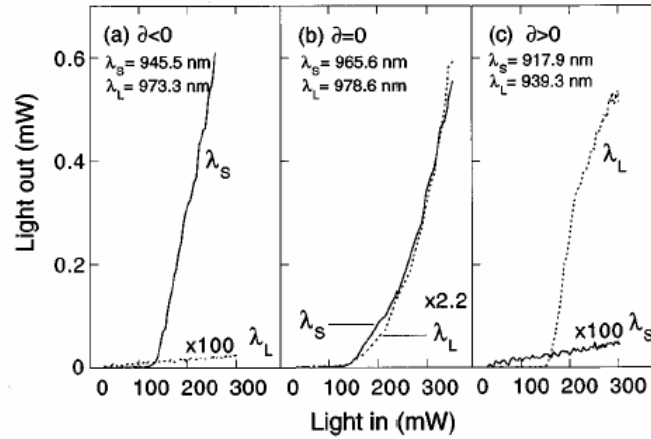


Figure 3.1: Optical power output in the top direction versus incident power for the two cavity modes, λ_S (solid line) and λ_L (dashed line). Each plot is from a different point of the wafer, corresponding to a different cavity detuning: (a) negative detuning ($L_{top} < L_{bot}$); (b) resonant cavities ($L_{top} = L_{bot}$); (c) positive detuning ($L_{top} > L_{bot}$);

The dynamics of the dual wavelength operation under optical excitation has been investigated in reference [8] by a different group. The QWs in this case were of different thicknesses while the cavities were of the same lengths. Lasing in pulses as short as 4.8 ps was achieved with a well pronounced asymmetry in the time-decay for the short and the long wavelength modes.

Simultaneous dual wavelength operation of CC-VCSELs with electrical pumping was first demonstrated by Carlin et al. [9]. The active regions were formed by InGaAs QWs of the same thickness but with a different number of wells in the two cavities, the two cavities being of slightly different length. In this device only one cavity, the shorter (top) cavity is electrically pumped. Lasing starts at the short wavelength mode. This laser emission acts as an optical pump for the QWs in the longer cavity and provides gain for the long wavelength mode, resulting in subsequent laser emission

on this mode. With increasing injection current, the device maintains stable emission at the two wavelengths over six times the threshold current.

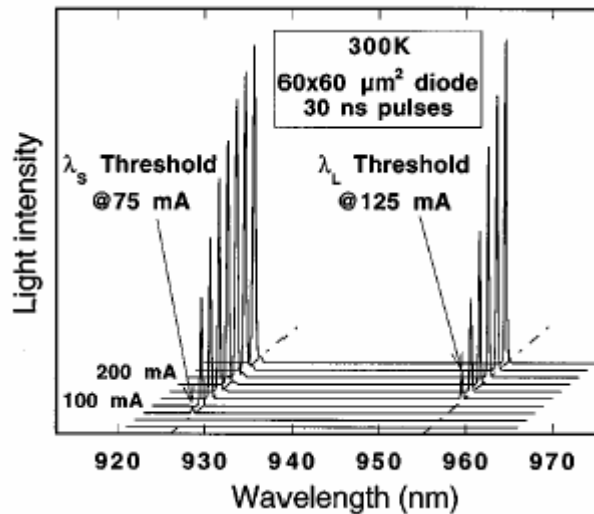


Figure 3.2: Emission spectra of $60 \times 60 \mu\text{m}^2$ coupled-cavity VCSEL measured under pulsed current injection [9].

In order to assure a well-controlled and stable operation of the coupled-cavity VCSEL device on two wavelengths simultaneously, a special attention has to be paid to the overlap between the spectral gain and the two cavity modes. One has to consider the thermal red-shift of both the cavity modes and the gain spectrum. The gain spectrum shifts with temperature at a rate of 0.4 nm/K , while the cavity modes shift at a rate of 0.065 nm/K , so the overlap between the gain maximum and the cavity modes is very sensitive to the temperature. As shown in Figure 3.3, in order to partially overcome this temperature dependence, one can design the CC-VCSEL device to operate on the low-wavelength side of the gain maximum, i.e. to red-shift the gain curve with respect to the cavity modes.

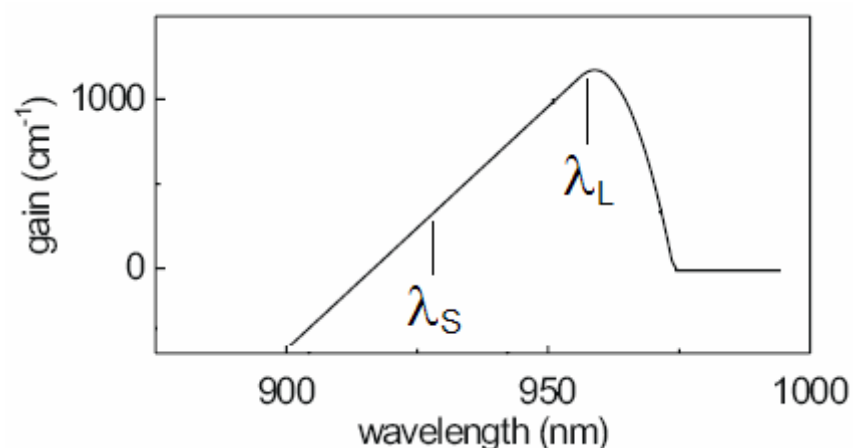


Figure 3.3: Sketch of the spectral gain showing the red-shift of the gain maximum with respect to the cavity modes.

In the next chapter, we give a detailed model that simulates the operation of the coupled-cavity VCSEL and the optical pumping in one cavity is one particular case that will be investigated. The results of this simulation are in good agreement with the experimental data reported in reference [9].

The above mentioned device however operated only with pulse current injection. The first electrical pumped CC-VCSELs capable of emitting simultaneously on two different wavelengths were built by Brunner et al. in 2000 [10]. When current is applied only to the top (shorter) cavity, lasing occurs at the short wavelength mode only. However, with injection current applied to the two cavities, the longer wavelength mode starts lasing first and the lasing undergoes a continuous transition to the short wavelength mode with increasing the injection current in the shorter cavity. This behavior is analyzed and explained on the basis of the model described in the next chapter.

CC-VCSELs consisting of an active cavity containing InGaAs QWs coupled to a passive GaAs cavity were realized by Fisher et al. [11]. The device demonstrates modulation characteristics arising from dynamic changes in the coupling between the active and the passive cavities. Modulation of the laser intensity by both forward and reverse biasing of the passive cavity was demonstrated and attributed to carrier induced changes in the refractive index and to field dependent cavity absorption in forward and reverse bias, respectively [11]. These CC-VCSELs structures have also been shown to operate in a Q-switch mode with a pulse width as small as 150 ps [12]. In contrast to conventional single cavity VCSELs, the Q-switching is achieved by modulation of the reverse bias applied to the passive cavity, i.e. by modulation of the optical losses rather than the optical gain [12].

Subsequently, CC-VCSELs with identical GaAs QWs in the two cavities were shown to exhibit bistable behavior in the Light-versus-Current (LI) characteristics even when operating in the multiple transverse mode regime [13]. Such bistability is only observed when operating in a CW mode, suggesting a strong influence of current induced heating in the CC-VCSELs. Cavity detuning induced by such heating and the shift of the absorption resonance in the passive cavity were suggested as a possible mechanism for the observed abrupt switching-off of the lasing action [13].

The threshold characteristics of CC-VCSELs were investigated in [14]. Lasing into two longitudinal modes and multiple transverse modes was reported and the effect of current injection in one cavity on the threshold current in the other cavity was demonstrated [14]. Single fundamental mode operation with 6.1 mW output power was achieved for these structures by reducing the aperture size [15]. In both cases, the two cavities are of the same length each containing five GaAs QWs. The electrical and optical confinement consists in an oxide layer for one cavity and proton implanted region for the other. When the current confinement apertures are of the same size strong mode competition is observed, resulting in mode hopping between the short and the long wavelength modes [15].

3.2 Device structure and operating principles

From now on we will study the coupled-cavity VCSEL with separate electrical injection in each cavity, first described by Brunner et al. [10]. Novel characteristics arising from the cavity coupling including methods for external modulation of the laser are demonstrated. The three-electrical-contact design of the structure enables independent control of the two separate gain regions. Because the lasing wavelength of a VCSEL is determined simply by the optical cavity length, the position of the lasing wavelength(s) can be precisely controlled.

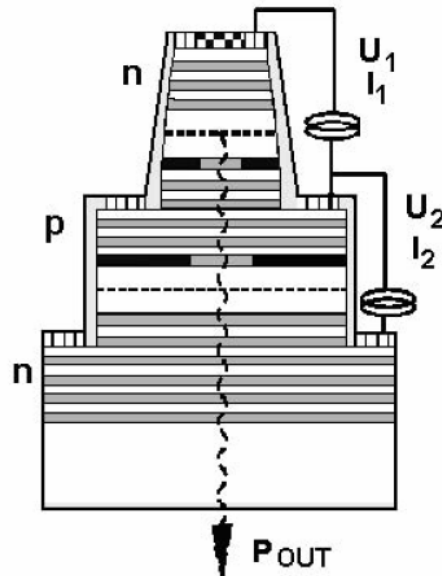


Figure 3.4: Schematic of the coupled-cavity VCSEL.

The coupled-cavity VCSEL consists of two optical cavities which can be independently pumped by both optical and electrical means. From the point of view of the operating principle, the coupling mirror shared by the two cavities plays an important role. Since a photon may pass through the coupling mirror from one cavity to another, the optical modes of the system are shared between the two cavities, the degree of optical coupling being controlled by the common mirror. It is mandatory to consider the whole structure in order to completely characterize the optical modes of the coupled microcavities.

Under dual-wavelength operation, some sort of mode competition will occur, especially when the mode spacing is small. However, when the mode spacing is large enough, mode competition is significantly reduced, increasing the possibility of two-mode oscillation. On the other hand, dual-wavelength operation with very large mode spacing is difficult to achieve because of the limited bandwidth of the gain medium.

The optical coupling between the cavities leads to two, non-degenerate longitudinal modes, which compete for the common gain reservoirs. The mode competition phenomenon depends on the design of the gain regions and on the degree of mode localization. For a symmetric coupled-cavity structure, the device supports two longitudinal modes, which have equal intensities in the two cavities.

Because of the large field overlap there will be a strong competition between the two modes for any gain located in the cavities; energy will be transferred from one mode to the other by absorption followed by re-emission. Therefore, simultaneous dual wavelength output is difficult to obtain. As one of the main objectives of this device was to achieve lasing on two different wavelengths, in order to stabilize the dual wavelength output, an asymmetry has to be introduced between the lengths of the two cavities. Typical detuning values between the two optical cavities are below 5%.

3.3 CC-VCSEL processing

The process flow for the fabrication of the CC-VCSEL device is complex. The most important steps are the deposition of the three electrical contacts (n-type for top and bottom contacts, p-type for the middle contact), the wet oxidation process to form the AlOx apertures for optical and electrical confinement and the etching of the two mesas. The lift-off steps employed for the electrical contacts represent a major difficulty. As the final diameter of the top mesa is small, there are many structures where the metal does not lift-off, depending mainly on their position on the wafer. Since there are two lift-off processes after the dry-etching of the second mesa, the final yield is small.

A second critical point is represented by the etching of the first AlOx layer in order to deposit the middle electrical contact. After dry-etching the first mesa, the two AlAs layers in the middle DBR are selectively oxidised. In order to deposit the middle electrical contact, the second mesa has to be etched and the etch process has to be stopped inside the middle DBR. So the first AlOx layer has to be etched as well. But AlOx is not attacked by the Cl-based plasma used to dry-etch the AlGaAs. In order to overcome this difficulty, a combined dry-etch – wet-etch procedure was established. After etching in a Cl-based plasma the AlGaAs material up to the AlOx layer, the sample was dry-etched in a CF₄-based plasma that successfully attacks the oxide layer. Subsequently, the usual wet-etch process was employed to expose a GaAs surface for metallization. Figure 3.5 shows the successful penetration of the oxide layer and subsequent wet-etching of the GaAs/AlGaAs material.

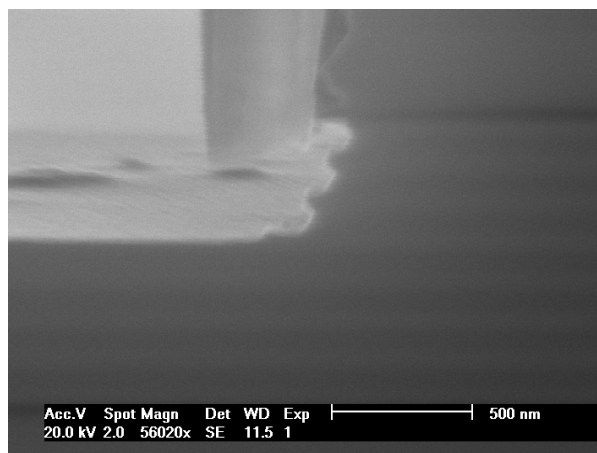


Figure 3.5: Successful etching of the first AlOx layer and subsequent etching of the middle DBR for p-contact deposition.

3.4 The lumped-mirror model

In order to describe the operation of the coupled-cavity vertical laser from the optical point of view, a lumped-mirror model is proposed. This model considers a simplified structure of the device as presented in Figure 3.6 and takes into account only the optical parameters of the structure. Let us consider the structure that consists of three hard-mirrors with the reflectivities denoted by R_1 and R_2 for the end-mirrors and R_0 for the mirror between the cavities, that assures the optical coupling. The actual structure has active media in each cavity, consisting of nominally identical InGaAs QWs as it will be shown in Chapter 4. In the algorithm developed in this section the gain/absorption contribution of the QWs in the cavities is included in the reflectivities (R_1 and R_2) for the end-mirrors.

The optical cavities are designed to be detuned by an amount ΔL so the actual lengths are given by $L_0 \pm \frac{\Delta L}{2}$. Furthermore, one has to take into account the penetration depth of the field in the cavities in each mirror, respectively. From now on, we will work with an effective cavity length that is obtained by adding to the physical cavity length the penetration depth of the field in the mirror i : L_{θ_i} . Thus, the resulting effective lengths of the cavities are:

$$L_{eff,1,2} = L_0 \pm \frac{\Delta L}{2} + L_{\theta_{1,2}} + L_{\theta_0} \equiv L_{1,2} \quad (3.1)$$

Having the structure characterized by the above parameters, the lumped mirrors model describes the wave pattern as the superposition of the four planar waves shown in Figure 3.6, all waves having the same damping coefficient γ .

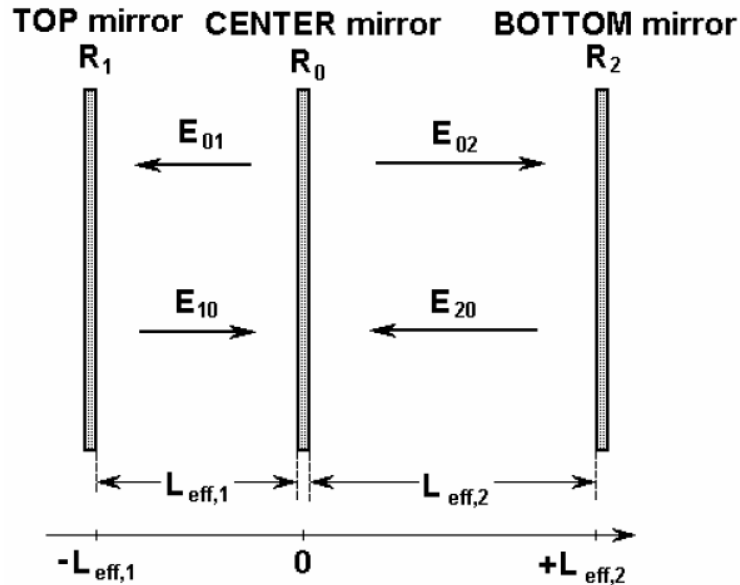


Figure 3.6: Schematic of the structure as considered in the lumped-mirrors model. The mirrors R_0 , R_1 and R_2 have zero thickness.

High reflectivity (close to 1) for the end-mirrors and lower reflectivity for the middle mirror corresponds to a strong coupling regime. The four planar waves are supposed to have the same extinction rate defined by the factor $\gamma/2$ in the equations below. The time dependent expressions for the fields in the cavities can be written as:

$$\begin{cases} E_{01} = \varepsilon_{01} \exp\left(i\omega - \frac{\gamma}{2}\right) \cdot \left(t + \frac{n}{c}x\right) \\ E_{10} = \varepsilon_{10} \exp\left(i\omega - \frac{\gamma}{2}\right) \cdot \left(t - \frac{n}{c}x\right) \\ E_{02} = \varepsilon_{02} \exp\left(i\omega - \frac{\gamma}{2}\right) \cdot \left(t - \frac{n}{c}x\right) \\ E_{20} = \varepsilon_{20} \exp\left(i\omega - \frac{\gamma}{2}\right) \cdot \left(t + \frac{n}{c}x\right) \end{cases} \quad (3.2)$$

In the previous equations, ε represents the amplitudes of the four waves, ω the pulsation, n the refractive index of the cavity and c the speed of light in free space. The centre mirror is chosen as the origin of the x coordinate. Therefore one has to impose boundary conditions for the end-mirrors reflexions: ($x = -L_1$ and $x = L_2$) as well as continuity conditions for the coupling mirror ($x = 0$). The equations that express these conditions are:

$$\begin{cases} E_{10} = e^{i\theta_1} \sqrt{R_1} E_{01} & x = -L_1 \\ E_{20} = e^{i\theta_2} \sqrt{R_2} E_{02} & x = L_2 \\ E_{01} = e^{i\theta_0} \sqrt{R_0} E_{10} - i e^{i\theta_0} \sqrt{1-R_0} E_{20} & x = 0 \\ E_{02} = e^{i\theta_0} \sqrt{R_0} E_{20} - i e^{i\theta_0} \sqrt{1-R_0} E_{10} & x = 0 \end{cases} \quad (3.3)$$

where $\theta_i = 2 \cdot k_0 \cdot L_{\theta_i}$ represents the phase change, the wave-vector of the Bragg reflector being defined by: $k_0 = \frac{2\pi}{L_0}$. Introducing the boundary and continuity conditions – eqs. (3.3) – in the set of

eqs. (3.2) and omitting the time dependent terms, we obtain:

$$\begin{cases} \varepsilon_{10} \cdot \exp\left[\frac{n}{c}L_1 \cdot \left(i\omega - \frac{\gamma}{2}\right)\right] = e^{i\theta_1} \sqrt{R_1} \cdot \varepsilon_{01} \cdot \exp\left[-\frac{n}{c}L_1 \cdot \left(i\omega - \frac{\gamma}{2}\right)\right] \\ \varepsilon_{20} \cdot \exp\left[\frac{n}{c}L_2 \cdot \left(i\omega - \frac{\gamma}{2}\right)\right] = e^{i\theta_2} \sqrt{R_2} \cdot \varepsilon_{02} \cdot \exp\left[-\frac{n}{c}L_2 \cdot \left(i\omega - \frac{\gamma}{2}\right)\right] \\ \varepsilon_{01} = e^{i\theta_0} \sqrt{R_0} \cdot \varepsilon_{10} - i \cdot e^{i\theta_0} \sqrt{1-R_0} \cdot \varepsilon_{20} \\ \varepsilon_{20} = e^{i\theta_0} \sqrt{R_0} \cdot \varepsilon_{20} - i \cdot e^{i\theta_0} \sqrt{1-R_0} \cdot \varepsilon_{10} \end{cases} \quad (3.4)$$

Rearranging the terms:

$$\begin{cases} \sqrt{R_1} \cdot \varepsilon_{01} = \varepsilon_{10} \cdot \exp\left[2 \cdot \left(i\omega - \frac{\gamma}{2}\right) \cdot \frac{n}{c} \cdot L_1 - i \cdot \theta_1\right] \\ \sqrt{R_2} \cdot \varepsilon_{02} = \varepsilon_{20} \cdot \exp\left[2 \cdot \left(i\omega - \frac{\gamma}{2}\right) \cdot \frac{n}{c} \cdot L_2 - i \cdot \theta_2\right] \\ \varepsilon_{01} = e^{i\theta_0} \cdot \left(\sqrt{R_0} \cdot \varepsilon_{10} - i \cdot \sqrt{1-R_0} \cdot \varepsilon_{20}\right) \\ \varepsilon_{02} = e^{i\theta_0} \cdot \left(-i \cdot \sqrt{1-R_0} \cdot \varepsilon_{10} + \sqrt{R_0} \cdot \varepsilon_{20}\right) \end{cases} \quad (3.5)$$

Eliminating ε_{01} and ε_{02} in the above set, a system of two eqs. and two unknowns is obtained.

We also introduce $k = \frac{\omega \cdot n}{c}$ and $g = \frac{\gamma \cdot n}{c}$:

$$\begin{cases} \varepsilon_{10} \cdot \exp[(2ik - g) \cdot L_1 - i \cdot \theta_1] = \sqrt{R_1} \cdot e^{i\theta_0} \cdot \left(\sqrt{R_0} \cdot \varepsilon_{10} - i \cdot \sqrt{1-R_0} \cdot \varepsilon_{20}\right) \\ \varepsilon_{20} \cdot \exp[(2ik - g) \cdot L_2 - i \cdot \theta_2] = \sqrt{R_2} \cdot e^{i\theta_0} \cdot \left(-i \cdot \sqrt{1-R_0} \cdot \varepsilon_{10} + \sqrt{R_0} \cdot \varepsilon_{20}\right) \end{cases} \quad (3.6)$$

Rearranging the terms with respect to ε_{10} and ε_{20} :

$$\begin{cases} \left[\exp[(2ik - g) \cdot L_1 - i \cdot (\theta_0 + \theta_1)] - \sqrt{R_1} \cdot R_0\right] \cdot \varepsilon_{10} + i \cdot \sqrt{(1-R_0)} \cdot R_1 \cdot \varepsilon_{20} = 0 \\ i \cdot \sqrt{(1-R_0)} \cdot R_2 \cdot \varepsilon_{10} - \left[\exp[(2ik - g) \cdot L_2 - i \cdot (\theta_0 + \theta_2)] - \sqrt{R_2} \cdot R_0\right] \cdot \varepsilon_{20} = 0 \end{cases} \quad (3.7)$$

The previous system is linear and homogenous with two equations and two unknowns. In order to have non-trivial solutions, one has to impose the condition that the discriminator of the system is zero. This condition can be written:

$$\left[\exp[(2ik - g) \cdot L_1 - i \cdot (\theta_0 + \theta_1)] - \sqrt{R_1} \cdot R_0\right] \cdot \left[\exp[(2ik - g) \cdot L_2 - i \cdot (\theta_0 + \theta_2)] - \sqrt{R_2} \cdot R_0\right] - (1-R_0) \cdot \sqrt{R_1} \cdot R_2 = 0 \quad (3.8)$$

Let us introduce the wave-vector k as a small arbitrary variation (k) of the wave-vector of the DBR (k_0): $k = k_0 + \Delta k$. We recall also equation (3.1) that expresses L_1 and L_2 . Taking into account that $2 \cdot k_0 \cdot L_{\theta_i} = \theta_i$, equation (3.8) becomes:

$$\left[\exp[(2i \cdot \Delta k - g) \cdot (L_1 + L_2)] - \sqrt{R_1} \cdot R_0\right] \cdot \exp[2i \cdot \Delta k \cdot L_2] \cdot e^{-i\varphi} - \sqrt{R_2} \cdot R_0 \cdot \exp[2i \cdot \Delta k \cdot L_1] \cdot e^{i\varphi} + \sqrt{R_1} \cdot R_2 = 0 \quad (3.9)$$

where the detuning between the cavities has been introduced as $\varphi = k_0 \Delta L = 2\pi \frac{\Delta L}{L_0}$. The previous

equation can be further simplified. One can evaluate the penetration depths L_{θ_i} in each mirror and consequently L_1 and L_2 . Let us make the following approximation noting with $X \cong \exp[(2 \cdot i \cdot \Delta k - g) \cdot L_1] \cong \exp[(2 \cdot i \cdot \Delta k - g) \cdot L_2] \cong \exp[(2 \cdot i \cdot \Delta k - g) \cdot L]$. In these conditions equation (3.9) is reduced at:

$$X^2 - \left(e^{i\varphi} \sqrt{R_2 R_0} + e^{-i\varphi} \sqrt{R_1 R_0}\right) X + \sqrt{R_1} R_2 = 0 \quad (3.10)$$

It is difficult to directly solve this second order equation so we will write the sum and the product of the solutions. Let X_1 and X_2 be solutions of equation (3.10):

$$\begin{cases} X_1 \cdot X_2 = \sqrt{R_1 \cdot R_2} \\ X_1 + X_2 = \frac{1}{2} \cdot (e^{i\varphi} \cdot \sqrt{R_2 \cdot R_0} + e^{-i\varphi} \cdot \sqrt{R_1 \cdot R_0}) \end{cases} \quad (3.11)$$

The product of the solutions of this equation is real, which means that the solutions are complex-conjugated so they can be written in the general form:

$$\begin{cases} X_1 = x_1 \cdot e^{i\theta} \\ X_2 = x_2 \cdot e^{-i\theta} \end{cases} \quad (3.12)$$

Introducing this in the expression for the sum of the solutions, we identify the real and the imaginary parts as follows:

$$\begin{aligned} X_1 + X_2 &= (x_1 + x_2) \cdot \cos\theta + i \cdot (x_1 - x_2) \cdot \sin\theta = \\ &= \frac{1}{2} \cdot (\sqrt{R_2} + \sqrt{R_1}) \cdot \sqrt{R_0} \cdot \cos\varphi + i \cdot (\sqrt{R_2} - \sqrt{R_1}) \cdot \sqrt{R_0} \cdot \sin\varphi \end{aligned} \quad (3.13)$$

Identification yields:

$$\begin{cases} x_1 + x_2 = \frac{1}{2} \cdot (\sqrt{R_2} + \sqrt{R_1}) \cdot \sqrt{R_0} \cdot \frac{\cos\varphi}{\cos\theta} \\ x_1 - x_2 = \frac{1}{2} \cdot (\sqrt{R_2} - \sqrt{R_1}) \cdot \sqrt{R_0} \cdot \frac{\sin\varphi}{\sin\theta} \end{cases} \quad (3.14)$$

From equations (3.14) one can find the modules x_1 and x_2 of the solutions X_1 and X_2 . So the solutions of equation (3.10) can be written:

$$\begin{cases} X_1 = x_1 \cdot e^{i\theta} = \frac{1}{4} \cdot \left[\left(1 - \frac{tg\varphi}{tg\theta}\right) \cdot \sqrt{R_1} + \left(1 + \frac{tg\varphi}{tg\theta}\right) \cdot \sqrt{R_2} \right] \cdot e^{i\theta} \\ X_2 = x_2 \cdot e^{-i\theta} = \frac{1}{4} \cdot \left[\left(1 + \frac{tg\varphi}{tg\theta}\right) \cdot \sqrt{R_1} + \left(1 - \frac{tg\varphi}{tg\theta}\right) \cdot \sqrt{R_2} \right] \cdot e^{-i\theta} \end{cases} \quad (3.15)$$

In the actual coupled-cavity VCSEL the reflectivities of the two end-mirrors are very high and very close to 1. One can make a good approximation setting $R_1 \cong R_2$. Thus we can express the phase term θ as a function of the structural parameters – coupling mirror reflectivity and detuning between the cavities – as follows:

$$\cos\theta = \sqrt{R_0} \cdot \cos\varphi \quad (3.16)$$

Going back to the definition of X :

$$X = \exp[(2 \cdot i \cdot \Delta k - g) \cdot L] = \exp(-g \cdot L) \cdot \exp(2 \cdot i \cdot \Delta k \cdot L) \quad (3.17)$$

we identify the module and the phase between the above definition of X and equations (22). The phase part yields two equations:

$$\begin{cases} 2 \cdot \Delta k_1 \cdot L = \theta \\ 2 \cdot \Delta k_2 \cdot L = -\theta \end{cases} \quad (3.18)$$

The effective length of the cavity L is made up of the original cavity length L_0 and the penetration depths in the neighbouring mirrors. For the case of an AIAs/GaAs DBR one finds:

$$L = \left(1 + 2 \cdot \frac{n_{AlAs}}{4 \cdot (n_{GaAs} - n_{AlAs})} \right) \cdot L_0 \cong 3.55 \cdot L_0 \quad (3.19)$$

3.5 Results of the lumped-mirror model

Introducing this in equations (3.18) one obtains the two resonant modes of the coupled-cavity VCSEL structure in closed form:

$$\begin{cases} k_1 = k_0 \cdot \left(1 + \frac{\theta}{4 \cdot \pi \cdot 3.55} \right) \\ k_2 = k_0 \cdot \left(1 - \frac{\theta}{4 \cdot \pi \cdot 3.55} \right) \end{cases} \Rightarrow \begin{cases} \lambda_1 = \frac{\lambda_0}{1 + \frac{\theta}{4 \cdot \pi \cdot 3.55}} \\ \lambda_2 = \frac{\lambda_0}{1 - \frac{\theta}{4 \cdot \pi \cdot 3.55}} \end{cases} \quad (3.20)$$

with θ given by equation (3.16). Equations (3.20) describe the mode splitting between the two modes supported in the structure. They are useful for the design of the device as they give the evolution of the wavelengths of the modes in the structure as a function of the detuning and of the coupling strength between the two cavities.

The modes in the detuned coupled cavities can be computed also with the transmission matrix method. The transmission matrix theory allows one to calculate the reflectivity of a stratified media. The transmission matrix expresses the inputs and outputs at a given port in terms of those at the others. The transmission matrix of a stack, containing an arbitrary number of transmission lines and dielectric interfaces, is simply found by matrix multiplication of the individual segments.

In Figure 3.7 the two modes are plotted versus the detuning between the cavities for different values of the reflectivity of the middle mirror according to the equation (3.20) (line). For comparison the results calculated in Matlab with the transmission matrix theory have also been plotted in the same figure for the same reflectivities of the coupling mirror (symbols). One can see the good agreement between the results provided by the two methods.

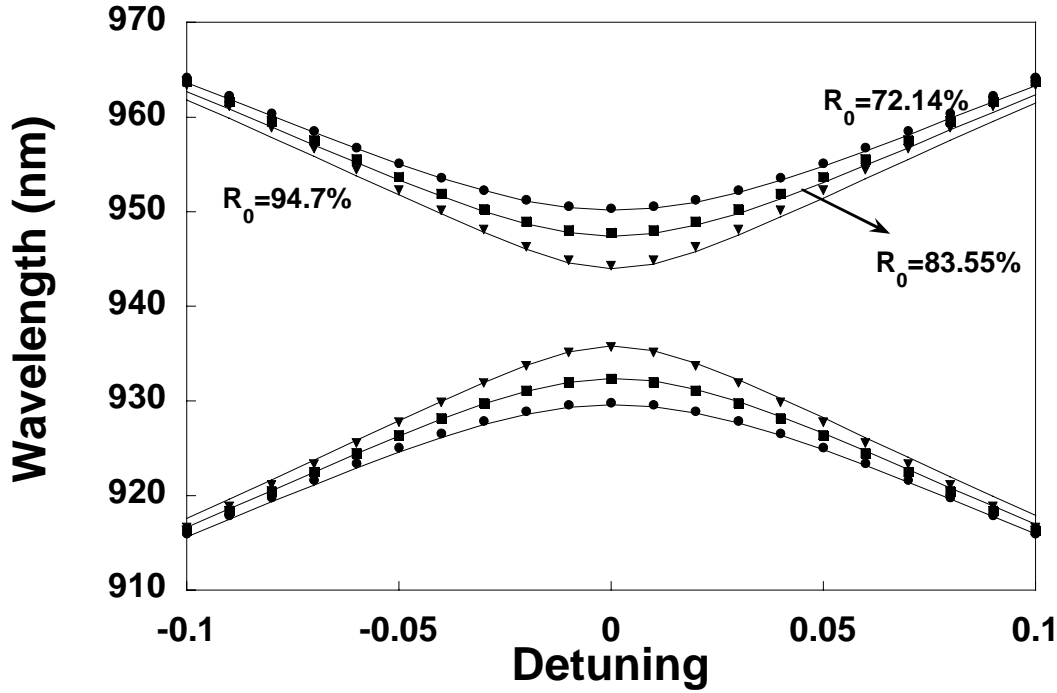


Figure 3.7: Wavelength splitting between the two modes supported in the structure.

Identification of the module part between eqs. (3.15) and expression (3.17) leads to:

$$\exp(-g \cdot L) = \frac{1}{4} \cdot \left[\left(1 \mp \frac{tg\varphi}{tg\theta} \right) \cdot \sqrt{R_1} + \left(1 \pm \frac{tg\varphi}{tg\theta} \right) \cdot \sqrt{R_2} \right] \quad (3.21)$$

The threshold condition imposes a non-evanescent wave so that $g = 0 \Rightarrow \exp(-g \cdot L) = 1$.

We make the following notation:

$$\begin{cases} \Gamma_1^s = \frac{1}{2} \cdot \left(1 - \frac{tg\varphi}{tg\theta} \right) \\ \Gamma_2^s = \frac{1}{2} \cdot \left(1 + \frac{tg\varphi}{tg\theta} \right) \end{cases} \quad (3.22)$$

We now explain the meaning of this notation. Let us evaluate the ratio of the squared modules of the field amplitudes in each cavity:

$$\left(\frac{|\mathcal{E}_{20}| + |\mathcal{E}_{02}|}{|\mathcal{E}_{10}| + |\mathcal{E}_{01}|} \right)^2 = \frac{|\mathcal{E}_{20}|^2}{|\mathcal{E}_{10}|^2} \cdot \left(\frac{1 + \frac{|\mathcal{E}_{02}|}{|\mathcal{E}_{20}|}}{1 + \frac{|\mathcal{E}_{01}|}{|\mathcal{E}_{10}|}} \right)^2 \quad (3.23)$$

Once we admit that X_1 and X_2 given by (3.15) are solutions for the characteristic equation (3.10), from system (3.7) we can write the ratio in the approximation $R_1 \cong R_2$:

$$\left| \frac{\mathcal{E}_{20}}{\mathcal{E}_{10}} \right|^2 = \frac{\sin(\theta + \varphi)}{\sin(\theta - \varphi)} \cdot \sqrt{\frac{R_2}{R_1}} \cong \frac{\sin(\theta + \varphi)}{\sin(\theta - \varphi)} = \frac{1}{2} \cdot \left(1 + \frac{\text{tg } \varphi}{\text{tg } \theta} \right) \quad (3.24)$$

From the first two equations of system (3.5) one finds the ratios:

$$\left| \frac{\mathcal{E}_{01}}{\mathcal{E}_{10}} \right| = \left| \frac{\exp(2ik \cdot L_1 - i \cdot \theta_1)}{\sqrt{R_1}} \right| = \frac{1}{\sqrt{R_1}} \quad (3.25)$$

$$\left| \frac{\mathcal{E}_{02}}{\mathcal{E}_{20}} \right| = \left| \frac{\exp(2ik \cdot L_2 - i \cdot \theta_2)}{\sqrt{R_2}} \right| = \frac{1}{\sqrt{R_2}}$$

Going back with these results to equation (3.23) we get:

$$\left(\frac{|\mathcal{E}_{20}| + |\mathcal{E}_{02}|}{|\mathcal{E}_{10}| + |\mathcal{E}_{01}|} \right)^2 \cong \frac{\frac{1}{2} \cdot \left(1 + \frac{\text{tg } \varphi}{\text{tg } \theta} \right)}{\frac{1}{2} \cdot \left(1 - \frac{\text{tg } \varphi}{\text{tg } \theta} \right)} \equiv \frac{\Gamma_2^S}{\Gamma_1^S} \quad (3.26)$$

So the Γ – coefficients defined in (3.22) represent the confinement of each mode in each cavity, i.e. Γ_i^α , ($i=1, 2$ and $\alpha=S, L$) represents the confinement factor that corresponds to the mode α (short or long) in the cavity i ($i=1$ – top, $i=2$ – bottom). Hereafter, we will call these coefficients the effective confinement factors. The confinement factors for the long wavelength mode are:

$$\begin{cases} \Gamma_1^L = \frac{1}{2} \cdot \left(1 + \frac{\text{tg } \varphi}{\text{tg } \theta} \right) \\ \Gamma_2^L = \frac{1}{2} \cdot \left(1 - \frac{\text{tg } \varphi}{\text{tg } \theta} \right) \end{cases} \quad (3.27)$$

One can check that the normation relations are verified:

$$\begin{cases} \Gamma_1^S + \Gamma_2^S = 1 \\ \Gamma_1^L + \Gamma_2^L = 1 \end{cases} \quad (3.28)$$

The confinement factors depend only on the coupling strength (so the interaction between the cavities is accounted for in $\Gamma_i^{S,L}$) and on the detuning between the cavities. They are symmetric for the two cavities, which means $\Gamma_i^{S,L} = \Gamma_j^{L,S}; i \neq j$. The evolution of this confinement coefficient with the detuning for different coupling strengths between the two cavities is presented in the Figure 3.8 below and represents a useful tool for the design of coupled-cavities VCSELs. Higher coupling degree between the cavities means higher transmission coefficient of the coupling mirror, so smaller reflectivity. In Figure 3.8 one can see that if the coupling is strong, the modes are closer to the equal distribution in both cavities even for a large detuning which means that the confinement coefficients are close to 0.5. Higher reflectivity of the coupling mirror, i.e. lower coupling, leads to a segregation

of the modes. They are close to equal distribution between the cavities only around zero detuning. As a design rule for the device, it is easier to play with the confinement coefficient $\Gamma_i^{S,L}$ for high coupling degree between the cavities – small reflectivity of the middle DBR, as the variation of the confinement coefficients is not as steep as in the case of low coupling.

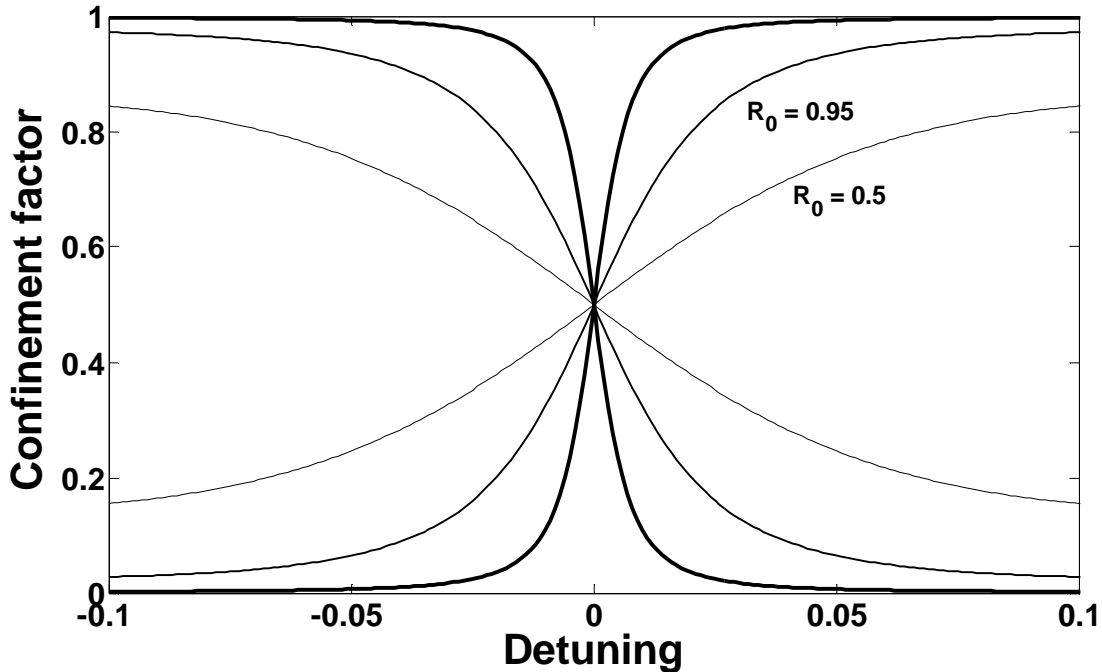


Figure 3.8: Effective confinement factor for different coupling strengths.

3.6 Design of the CC-VCSEL structures

In the symmetric structure (zero detuning) the two modes are equally shared between the two cavities. As a detuning is introduced the short wavelength mode becomes more localised in the short cavity (increasing Γ_1^S) and the long wavelength mode becomes more localised in the long cavity (increasing in the same time Γ_2^L). In Figure 3.9 to Figure 3.11 we present reflectivity/absorption spectra for CC-VCSEL structures with different detuning values as well as the field distributions inside these structures. The graphs in Figure 3.9 to Figure 3.11 are calculated in Matlab using the transmission matrix theory.

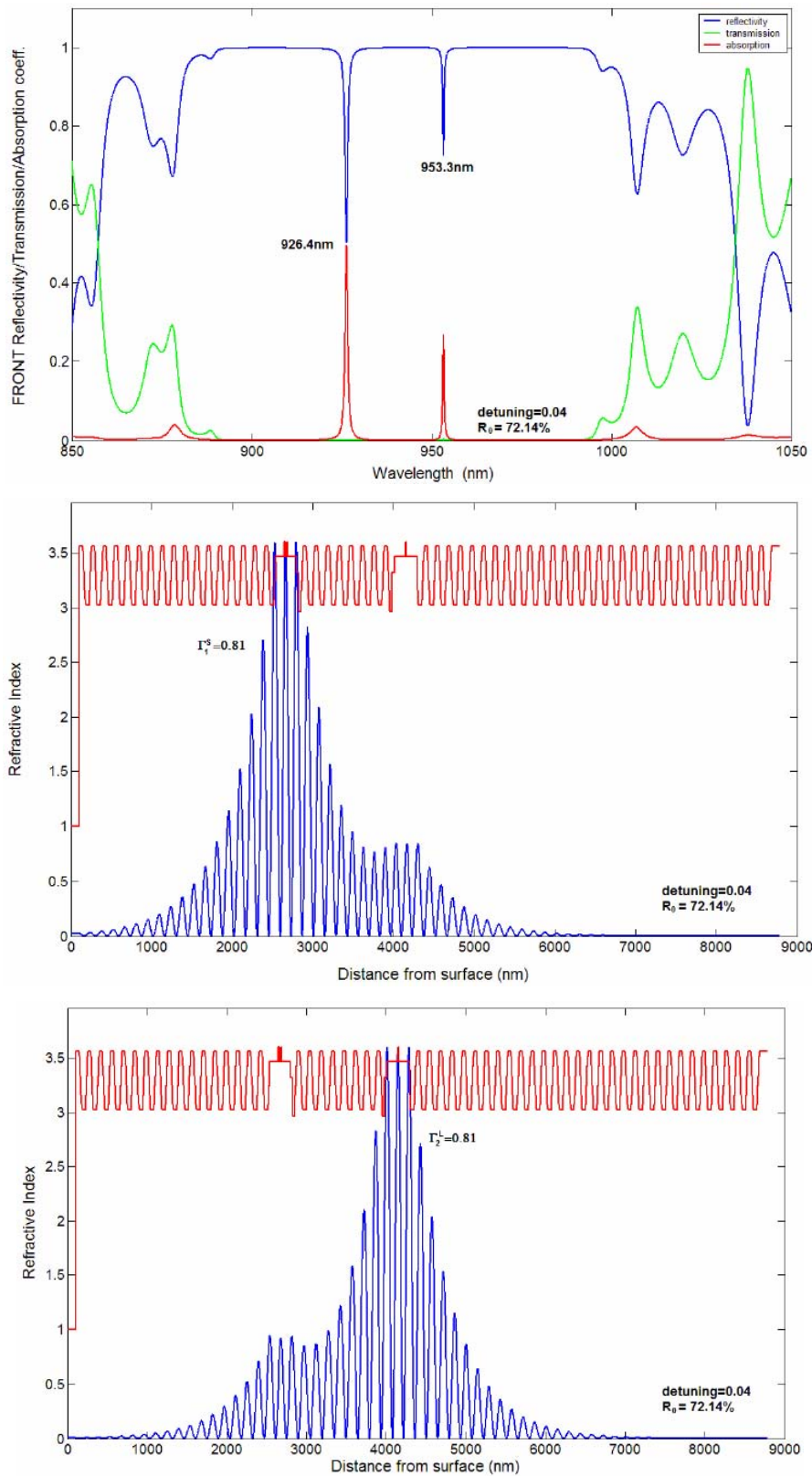


Figure 3.9: Modes' position and confinement inside a CC-VCSEL structure with 4% detuning and 72.14% coupling mirror reflectivity.

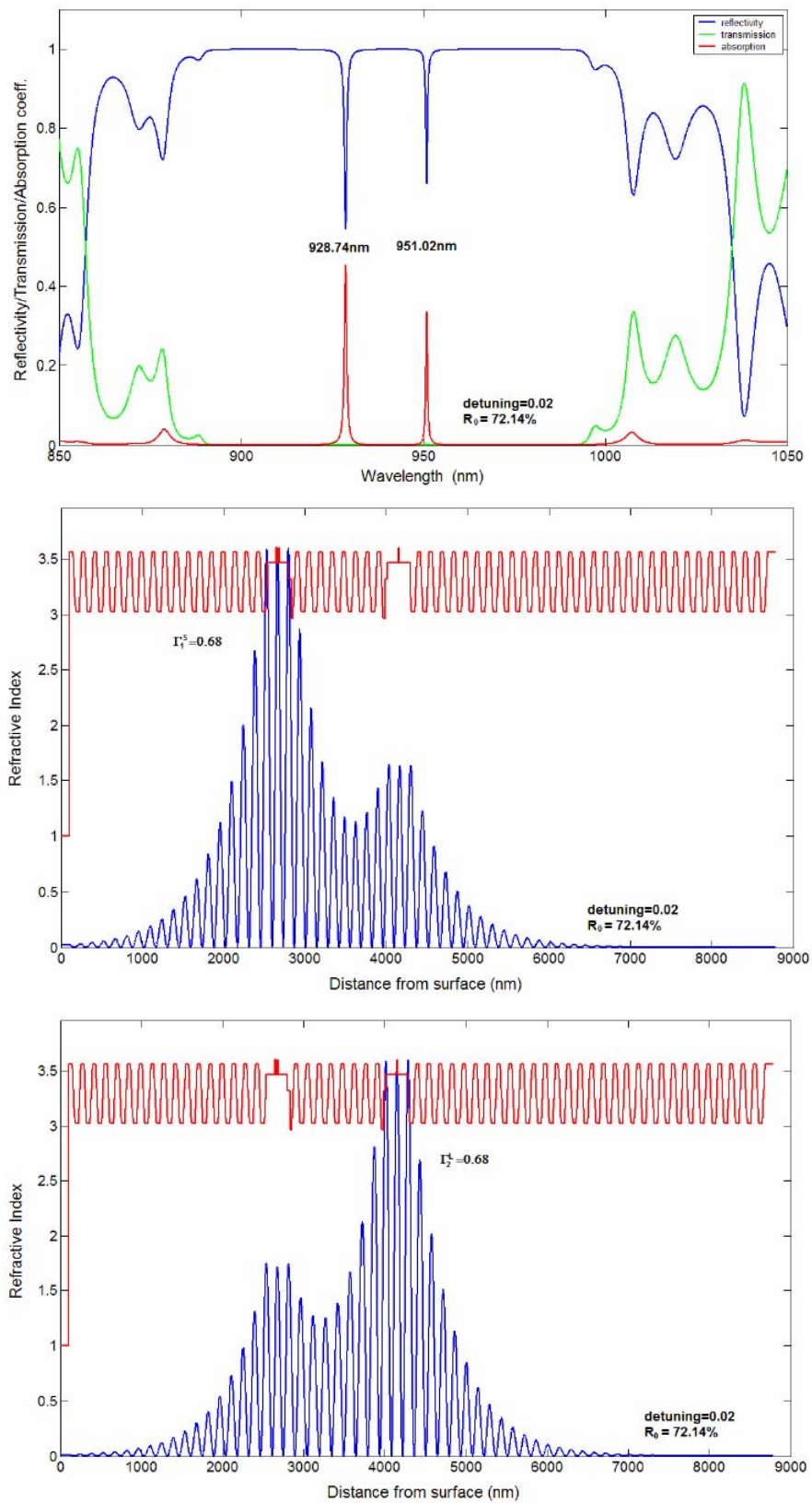


Figure 3.10: Modes' position and confinement inside a CC-VCSEL structure with 2% detuning and 72.14% coupling mirror reflectivity.

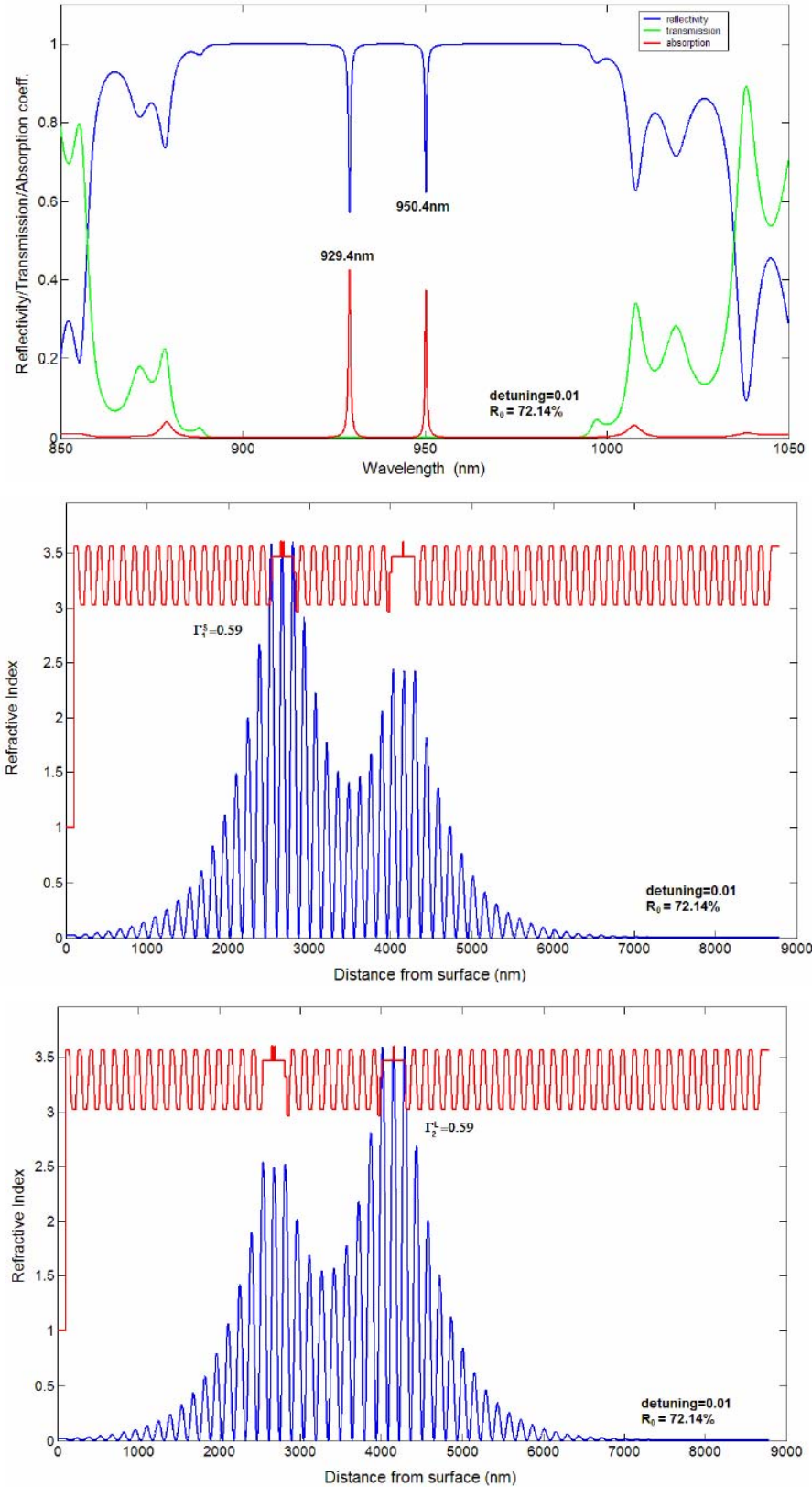


Figure 3.11: Modes' position and confinement inside a CC-VCSEL structure with 1% detuning and 72.14% coupling mirror reflectivity.

One can see that the mode spacing becomes smaller as the detuning is decreased in agreement with the model presented above. Another confirmation is given by the confinement coefficient that

describes a more pronounced asymmetry (81%) for 4% detuning versus a more balanced distribution of the two modes in the two cavities (59%) for a structure closer to the symmetric case, i.e. with only 1% detuning between the two cavities.

3.7 Conclusions

In this chapter we present a simple model that considers only the optical parameters of the coupled-cavity VCSEL structure and starting from these input parameters provides the two resonant modes supported in the structure as well as the degree of confinement of each optical mode in the corresponding cavity. These essential characteristics of the device are calculated with the lumped-mirror model as a function of the reflectivity of the coupling mirror, i.e. the strength of the optical coupling between the two cavities, and versus the detuning between the two cavities, i.e. the asymmetry introduced between them. The results obtained with the lumped-mirror model prove to be in good agreement with the calculations performed with Matlab code built on the basis of the transmission matrix theory.

The next chapter will complete in the framework of the rate-equation model, the present lumped-mirror model, considering the electrical injection together with the optical parameters of the structures.

Bibliography CHAPTER 3

-
- [1] H. Kawaguchi, *IEE Proc. J. Optoelectron*, **140**, 3 (1993).
 - [2] G. P. Agarwal and N. Dutta K., *Semiconductor Lasers*, 2nd ed. (Van Nostrand Reinhold, New York, 1993), p. 530.
 - [3] W. T. Sang, in *Semiconductors and Semimetals*, edited by R. K. Willardson and A. C. Beer (Academic, New York, 1985), **22B**, p.257.
 - [4] R.P. Stanley, R. Houdre, U. Oesterle, M. Ilegems, C. Weisbuch, Coupled semiconductor microcavities, *Appl. Phys. Lett.*, **65**, pp.2093-2095 (1994).
 - [5] P. Pellandini, R.P. Stanley, R. Houdre, U. Oesterle, M. Ilegems, C. Weisbuch, "Dual-wavelength emission from coupled semiconductor microcavity", *Appl. Phys. Lett.*, **71**, pp.864-866 (1997).
 - [6] C.L. Wang, Y.H. Chuang, C.L. Pan, Two wavelength interferometer based on a two-color laser-diode array and the second-order correlation technique, *Opt.Lett.*, **20**,1071 (1995).
 - [7] C.L. Wang, C.L. Pan, Tunable multigigahertz beat signal generation from a two-wavelength laser-diode array, *Opt. Lett.*, **20**, p. 1292 (1995).
 - [8] P. Michler, H. Hilpert, G. Reiner, Dynamics of dual-wavelength emission from coupled semiconductor microcavity laser, *Appl. Phys. Lett.*, **70**, pp.2073-2075 (1997).
 - [9] J.-F. Carlin, R.P. Stanley, P. Pellandini, U. Oesterle, and M. Ilegems, The dual wavelength Bivertical cavity surface-emitting laser, *Appl. Phys. Lett.*, **75**, pp.908-910 (2000).

- [10] M. Brunner, K. Gulden, R. Hovel, M. Moser, J.-F. Carlin, R.P. Stanley, and M. Ilegems, Continuous-Wave Dual-Wavelength Lasing in a Two-Section Vertical-Cavity Laser, *IEEE Phot. Techn. Lett.*, **12**, pp.1316-1318 (2000).
- [11] A. J. Fisher, K. D. Choquette, W. W. Chow, H. Q. Hou, and K. M. Geib, "Coupled resonator vertical-cavity diode", *Appl. Phys. Lett.*, **75**, pp. 3020-3022 (1999).
- [12] A. J. Fisher, W. W. Chow, K. D. Choquette, A. A. Allerman, and K. M. Geib, "Q-switched operation of a coupled-resonator vertical-cavity diode", *Appl. Phys. Lett.*, **76**, pp. 1975-1977 (1999).
- [13] A. J. Fisher, K. D. Choquette, W. W. Chow, A. A. Allerman, and K. M. Geib, "Bistable output from a coupled-resonator vertical-cavity diode", *Appl. Phys. Lett.*, **77**, pp. 3319-3321 (2000).
- [14] D. M. Grasso, K. D. Choquette, "Threshold and Modal Characteristics of Composite-Resonator Vertical-Cavity Lasers", *IEEE J. Quant. Electron.*, **39**, pp. 1526-1530 (2003).
- [15] A. J. Fischer, K. D. Choquette, W. W. Chow, A. A. Allerman, D. K. Serkland, and K.M. Geib, "High single-mode power observed from a coupled-resonator vertical-cavity laser diode", *Appl. Phys. Lett.*, **79**, pp. 4079-4081 (2001).

Chapter 4*

Rate-equation model for CC-VCSELs

4.1 Rate equations – general form

The operation of the coupled-cavity device is described starting from simple, intuitive arguments, developing the rate-equations for both the number of carriers, N_i , and the number of photons, $N_{ph}^{S,L}$, for the two optical modes. The reservoir model [1] used to develop the rate-equations is shown below (Figure 4.1). From now on, we will use the subscript index $i=1, 2$ to denote the cavity ($1 = \text{top, shorter cavity}; 2 = \text{bottom, longer cavity}$), and the superscript index “S” or “L” to denote the short or the long mode, respectively. We recall that the short mode is predominantly confined in the short/top ($i=1$) cavity and the long mode is predominantly confined in the long/bottom ($i=2$) cavity. The number of carriers injected into each cavity of the laser is I_i/q but only a fraction of $\eta_i I_i/q$ reaches the corresponding QW active region i , where η_i designates the carrier injection efficiency of the laser. The carriers that succeed to get in the reservoir may experience: (i) non-radiative recombination at the rate $R_{nr,i}$; (ii) spontaneous recombination at the rate $R_{sp,i}$ of which a certain fraction, given by the spontaneous emission factor, recombine in the mode of interest $\beta_{sp,i} R_{sp,i}$; (iii) stimulated recombination at the rate $R_{em,i}$; (iv) stimulated absorption at the rate $R_{abs,i}$.

In the following, the spontaneous recombination into the cavity modes will be neglected. The recombination rates will be expressed as usual per unit volume, and therefore are multiplied by the volume V_i of the active region, i.e. of the QWs, in Figure 4.1. $V_{p,i}$ represent the volume occupied by the optical modes in the cavities.

In the two photon-reservoirs, the number of photons in modes “S” and “L” varies as follows: stimulated and spontaneous emission provide the emission of photons at the rate: $R_{em,i} + \beta_{sp,i} R_{sp,i}$ while the absorption in the active region depletes photons at the rate $R_{abs,i}$. All the other photons either leave

* This chapter is based on the papers:

- V. Badilita, J.-F. Carlin, M. Brunner, and M. Ilegems, “Light-current characterization of dual-wavelength VCSELs”, *Proc. SPIE*, vol. 4649, pp. 87–95, 2002.
- V. Badilita, J.-F. Carlin, K. Panajotov, and M. Ilegems, “Rate-Equation Model for Coupled-Cavity Surface-Emitting Lasers”, accepted for publication in *IEEE Journal of Quantum Electronics*, Dec. 2004.

the cavity through the mirrors or are internally absorbed; the photon population decays at the rate $N_{p,i}^{S,L} / \tau_{ph}^{S,L}$, where $N_{p,i}^{S,L}$ is the number of photons in cavity i in the mode “S” or “L” and $\tau_{ph}^{S,L}$ is the photon lifetime in the mode “S” or “L”. Following the usual procedure we obtain the carrier and photon number rate equations, setting the time variation rate of the number of carriers and photons equal to the sum of rates into, minus the sum of rates out of the respective reservoirs.

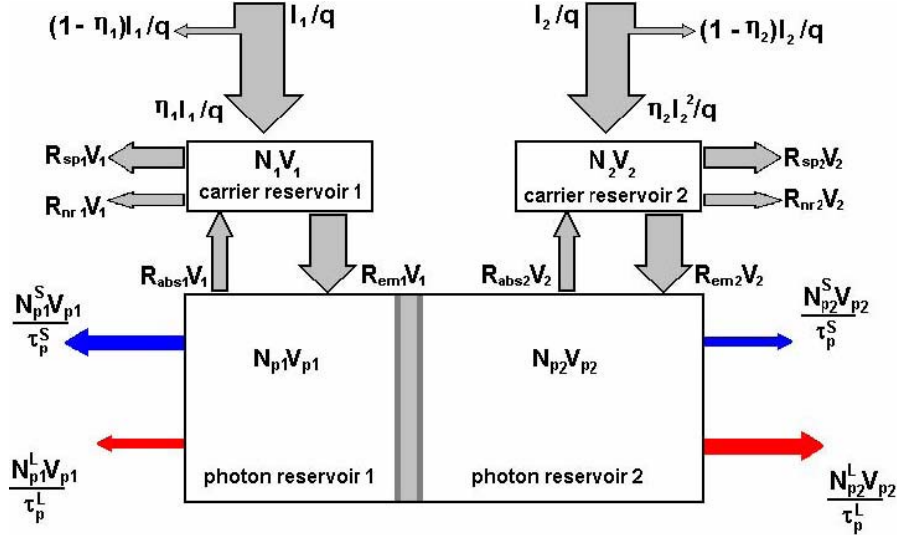


Figure 4.1: Reservoir model of the coupled-cavities VCSEL.

The rate equations for the carriers are written for each cavity while those for the photons are written for each mode (S – short and L – long):

$$\frac{dN_1}{dt} = \frac{\eta_1 I_1}{q} - (R_{em,1} - R_{abs,1}) \cdot V_1 - (R_{sp,1} + R_{nr,1}) \cdot V_1 \quad (4.1)$$

$$\frac{dN_2}{dt} = \frac{\eta_2 I_2}{q} - (R_{em,2} - R_{abs,2}) \cdot V_2 - (R_{sp,2} + R_{nr,2}) \cdot V_2 \quad (4.2)$$

The rate equations for the photons in the short, respectively long wavelength modes are given by:

$$\frac{d}{dt} (N_{ph,1}^S + N_{ph,2}^S) \equiv \frac{dN_{ph}^S}{dt} = [(R_{em,1}^S - R_{abs,1}^S) \cdot V_1 + (R_{em,2}^S - R_{abs,2}^S) \cdot V_2] + (\beta_{sp,1}^S R_{sp,1} V_1 + \beta_{sp,2}^S R_{sp,2} V_2) - \frac{N_{ph}^S}{\tau_{ph}^S} \quad (4.3)$$

$$\frac{d}{dt} (N_{ph,1}^L + N_{ph,2}^L) \equiv \frac{dN_{ph}^L}{dt} = [(R_{em,1}^L - R_{abs,1}^L) \cdot V_1 + (R_{em,2}^L - R_{abs,2}^L) \cdot V_2] + (\beta_{sp,1}^L R_{sp,1} V_1 + \beta_{sp,2}^L R_{sp,2} V_2) - \frac{N_{ph}^L}{\tau_{ph}^L} \quad (4.4)$$

where the total number of photons $N_{ph}^{S,L}$ in the mode “S” or “L” has been introduced.

Before proceeding further, let us develop some preliminary considerations: the variation of the carrier density in cavity i due to stimulated emission and stimulated absorption is given by [1]:

$$R_{em,i} - R_{abs,i} = \frac{2\xi_i^S v_g^S}{V_{ph,i}} N_{ph,i}^S g_i^S + \frac{2\xi_i^L v_g^L}{V_{ph,i}} N_{ph,i}^L g_i^L \quad (4.5)$$

valid for $i = 1, 2$

where $g_i^{S,L}$ represent the gain coefficients for the modes “S” or “L” in the cavity i , $v_g^{S,L}$ the group velocity corresponding to the photons in each mode, and $V_{ph,i}$ the volume of the cavity i . The factor 2 accounts for the fact that one photon crosses the active region two times per round trip. The other parameter – $\xi_i^{S,L}$ – stands for the standing wave enhancement factor that depends on the placement of the QWs with respect to the field distribution; the value of $\xi_i^{S,L}$ varies between 0 if the QWs are placed at a field node, and 2 if the QWs are located at a field maximum. The standing wave enhancement factors are design parameters calculated using a transmission matrix program.

The derivation of the rate equation model is presented with full details in Appendix A. It consists in imposing steady-state conditions to the rate-equations for carriers and photons, expressing the number of photons in each mode, in each cavity ($N_{ph,i}^{S,L}$) using the confinement coefficients ($\Gamma_i^{S,L}$) found in Chapter 3 with the lumped-mirror model, and using the fact that the spontaneous emission rate together with the non-radiative recombination rate in cavity i are proportional to the total carrier density in cavity $i - \frac{N_i}{V_i}$, the proportionality factor being the carrier lifetime τ_e assumed to be the same in both cavities:

$$R_{sp,i} + R_{nr,i} = \frac{N_i}{V_i \tau_e} \quad (4.6)$$

We take the result of the derivation carried out in Appendix A, i.e. the expression of the rate equations for carriers and photons written in the compact form below:

$$\frac{\eta_1 I_1}{q} = 2\xi_1^S v_g^S \cdot \frac{l_1}{L} \cdot \Gamma_1^S N_{ph}^S \cdot g_1^S + 2\xi_1^L v_g^L \cdot \frac{l_1}{L} \cdot \Gamma_1^L N_{ph}^L \cdot g_1^L + \frac{N_1}{\tau_e} \quad (4.7)$$

$$\frac{\eta_2 I_2}{q} = 2\xi_2^S v_g^S \cdot \frac{l_2}{L} \cdot \Gamma_2^S N_{ph}^S \cdot g_2^S + 2\xi_2^L v_g^L \cdot \frac{l_2}{L} \cdot \Gamma_2^L N_{ph}^L \cdot g_2^L + \frac{N_2}{\tau_e} \quad (4.8)$$

$$N_{ph}^S \cdot \left(2\xi_1^S v_g^S \cdot \frac{l_1}{L} \cdot \Gamma_1^S \cdot g_1^S + 2\xi_2^S v_g^S \cdot \frac{l_2}{L} \cdot \Gamma_2^S \cdot g_2^S - \frac{1}{\tau_{ph}^S} \right) = 0 \quad (4.9)$$

$$N_{ph}^L \cdot \left(2\xi_1^L v_g^L \cdot \frac{l_1}{L} \cdot \Gamma_1^L \cdot g_1^L + 2\xi_2^L v_g^L \cdot \frac{l_2}{L} \cdot \Gamma_2^L \cdot g_2^L - \frac{1}{\tau_{ph}^L} \right) = 0 \quad (4.10)$$

4.2 Solutions for different operating regimes

For numerical calculations we will write the system (4.7-10) in a simpler way as follows:

$$\frac{\eta_1 I_1}{q} = A_1^S \cdot N_{ph}^S g_1^S + A_1^L \cdot N_{ph}^L g_1^L + \frac{1}{\tau_e} \cdot N_1 \quad (4.11)$$

$$\frac{\eta_2 I_2}{q} = A_2^S \cdot N_{ph}^S g_2^S + A_2^L \cdot N_{ph}^L g_2^L + \frac{1}{\tau_e} \cdot N_2 \quad (4.12)$$

$$N_{ph}^S \cdot \left(A_1^S \cdot g_1^S + A_2^S \cdot g_2^S - \frac{1}{\tau_{ph}^S} \right) = 0 \quad (4.13)$$

$$N_{ph}^L \cdot \left(A_1^L \cdot g_1^L + A_2^L \cdot g_2^L - \frac{1}{\tau_{ph}^L} \right) = 0 \quad (4.14)$$

The constants introduced in the equations above contain the design parameters of the device and are given below:

$$A_1^S = 2\xi_1^S v_g^S (l_1 / L) \Gamma_1^S \quad A_2^S = 2\xi_2^S v_g^S (l_2 / L) \Gamma_2^S \quad (4.15)$$

$$A_1^L = 2\xi_1^L v_g^L (l_1 / L) \Gamma_1^L \quad A_2^L = 2\xi_2^L v_g^L (l_2 / L) \Gamma_2^L \quad (4.16)$$

We express the gain versus carrier density variation by a logarithmic dependence with three fitting parameters [1] which can be resumed in the following equations:

$$g_1^S = G_0^S \cdot \ln \frac{n_1 + n_0^S}{n_{tr}^S + n_0^S} \quad (4.17)$$

$$g_2^S = G_0^S \cdot \ln \frac{n_2 + n_0^S}{n_{tr}^S + n_0^S} \quad (4.18)$$

$$g_1^L = G_0^L \cdot \ln \frac{n_1 + n_0^L}{n_{tr}^L + n_0^L} \quad (4.19)$$

$$g_2^L = G_0^L \cdot \ln \frac{n_2 + n_0^L}{n_{tr}^L + n_0^L} \quad (4.20)$$

where $n_i = \frac{N_i}{V_i}$ designates the carrier densities in the quantum wells. The fitting parameter $n_{tr}^{S,L}$ represents the transparency carrier density such that if the carrier density in one cavity reaches this value, the corresponding gain is zero. The fitting parameter $n_0^{S,L}$ determines the quantum well absorption at the corresponding wavelength, i.e.:

$$\alpha^{S,L} = G_0^{S,L} \cdot \ln \frac{n_0^{S,L}}{n_{tr}^{S,L} + n_0^{S,L}} \quad (4.21)$$

Equations (4.11-14) form a system of 4 equations having 4 unknowns: the two photon numbers $N_{ph}^{S,L}$, the two carrier numbers N_i , and 2 input parameters – the two bias currents I_i . In fact one can set any other two parameters as “input parameters” and solve the system with respect to the remaining 4 unknowns. For instance, for any pair of injection currents (I_1, I_2) one can determine the corresponding number of photons, i.e. the output powers for each mode, and the number of carriers which give also the gain coefficients.

In this section, we separately consider the following cases:

- A. The “double-threshold” point which is the point where both modes start lasing simultaneously;
- B. One mode lasing threshold while the other mode remains below threshold;
- C. One mode lasing threshold provided the other mode is well above threshold;
- D. One mode well above threshold provided the other mode is below threshold.
- E. Both modes well above threshold;

For each situation, the dependency between the two injection currents to fulfill the corresponding lasing conditions is found.

A. The “double-threshold” point

An important point in the description of a CC-VCSEL is the “double-threshold point”, the point where the two modes start lasing simultaneously. At this point the numbers of photons in each mode is zero $N_{ph}^S = N_{ph}^L = 0$ so equations (4.11-12) can be written:

$$\frac{\eta_1 I_1}{q} = \frac{1}{\tau_e} \cdot N_1 \quad (4.22)$$

$$\frac{\eta_2 I_2}{q} = \frac{1}{\tau_e} \cdot N_2 \quad (4.23)$$

Equations (4.13-14) must be satisfied whatever the values of N_{ph}^S and N_{ph}^L , whenever the corresponding mode is lasing:

$$A_1^S \cdot G_0^S \cdot \ln \frac{n_1 + n_0^S}{n_{tr}^S + n_0^S} + A_2^S \cdot G_0^S \cdot \ln \frac{n_2 + n_0^S}{n_{tr}^S + n_0^S} - \frac{1}{\tau_{ph}^S} = 0 \quad (4.24)$$

$$A_1^L \cdot G_0^L \cdot \ln \frac{n_1 + n_0^L}{n_{tr}^L + n_0^L} + A_2^L \cdot G_0^L \cdot \ln \frac{n_2 + n_0^L}{n_{tr}^L + n_0^L} - \frac{1}{\tau_{ph}^L} = 0 \quad (4.25)$$

where the gain-carrier density dependences have already been inserted to get the threshold equations (4.24-25). The last two equations determine the double-threshold carrier numbers – $N_{1,0}$, $N_{2,0}$ and in consequence the gains corresponding to the double-threshold – $g_{1,0}^{S,L}$, $g_{2,0}^{S,L}$. Together with equations (4.22-23) they determine the bias current values needed to achieve simultaneous dual-wavelength lasing ($I_{1,0}, I_{2,0}$). This point is labeled by “A” in Figure 4.3.

B. Borders of the single-mode lasing regions

In order to find the $I_2=f(I_1)$ for the long-wavelength mode threshold, we solved the above system for $N_{ph}^S = N_{ph}^L = 0$ taking into account the threshold equation for the long-wavelength mode – equation (4.14). The threshold equation (4.13) for the short-wavelength mode is not valid since this mode is under threshold. In this case the equations can be written:

$$\frac{\eta_1 I_1}{q} = \frac{1}{\tau_e} \cdot N_1 \quad (4.26)$$

$$\frac{\eta_2 I_2}{q} = \frac{1}{\tau_e} \cdot N_2 \quad (4.27)$$

$$A_1^L \cdot G_0^L \cdot \ln \frac{n_1 + n_0^L}{n_{tr}^L + n_0^L} + A_2^L \cdot G_0^L \cdot \ln \frac{n_2 + n_0^L}{n_{tr}^L + n_0^L} - \frac{1}{\tau_{ph}^L} = 0 \quad (4.28)$$

The interdependence between the two carrier densities given by (4.28) is introduced in (4.27) in order to find the relationship between the two bias currents.

The procedure to find the $I_2=f(I_1)$ relation for the short-wavelength mode threshold while the long-wavelength mode is below threshold is similar. The theoretical curves corresponding to this case are labeled by “B” in Figure 4.3.

C. Borders of “both modes lasing” region

In order to find the $I_2=f(I_1)$ for the threshold of the long-wavelength mode while the short wavelength mode is lasing, we solve the above system for $N_{ph}^L = 0$ and $N_{ph}^S > 0$. Both threshold equations (4.13) and (4.14) are valid since one mode is above threshold (short wavelength mode) and the other is exactly at threshold (long wavelength mode). The system in this case is written:

$$\frac{\eta_1 I_1}{q} = A_1^S \cdot N_{ph}^S \cdot G_0^S \cdot \ln \frac{n_1 + n_0^S}{n_{tr}^S + n_0^S} + \frac{1}{\tau_e} \cdot N_1 \quad (4.29)$$

$$\frac{\eta_2 I_2}{q} = A_2^S \cdot N_{ph}^S \cdot G_0^S \cdot \ln \frac{n_2 + n_0^S}{n_{tr}^S + n_0^S} + \frac{1}{\tau_e} \cdot N_2 \quad (4.30)$$

$$A_1^S \cdot G_0^S \cdot \ln \frac{n_1 + n_0^S}{n_{tr}^S + n_0^S} + A_2^S \cdot G_0^S \cdot \ln \frac{n_2 + n_0^S}{n_{tr}^S + n_0^S} - \frac{1}{\tau_{ph}^S} = 0 \quad (4.31)$$

$$A_1^L \cdot G_0^L \cdot \ln \frac{n_1 + n_0^L}{n_{tr}^L + n_0^L} + A_2^L \cdot G_0^L \cdot \ln \frac{n_2 + n_0^L}{n_{tr}^L + n_0^L} - \frac{1}{\tau_{ph}^L} = 0 \quad (4.32)$$

One can notice that the last two equations are identical with (4.24) and (4.25), used to characterize the double-threshold point of the device. This means that the number of carriers and the gain values for the whole dual-wavelength region – where both threshold equations hold simultaneously – will be equal to the threshold number of carriers and the corresponding gains. Analogous with a single-cavity laser, the gains and the number of carriers in each cavity are pinned in the case of simultaneous lasing on both modes. With the gains and number of carriers pinned at their threshold value, we get a linear dependence $I_2=f(I_1)$. The analytical dependence between the two bias currents for the threshold of the “L”-mode while the “S”-mode is above threshold is given below:

$$I_2 = \frac{\eta_1}{\eta_2} \cdot \frac{A_2^S g_{2,0}^S}{A_1^S g_{1,0}^S} \cdot \left(I_1 - \frac{1}{\tau_e} \cdot qN_{1,0} \right) + \frac{1}{\tau_e} \cdot qN_{2,0} \quad (4.33)$$

The procedure is similar to find the threshold of the short-wavelength mode while the long-wavelength mode is lasing. The set of equations used to study this case is given by:

$$\frac{\eta_1 I_1}{q} = A_1^L \cdot N_{ph}^L \cdot G_0^L \cdot \ln \frac{n_1 + n_0^L}{n_{tr}^L + n_0^L} + \frac{1}{\tau_e} \cdot N_1 \quad (4.34)$$

$$\frac{\eta_2 I_2}{q} = A_2^L \cdot N_{ph}^L \cdot G_0^L \cdot \ln \frac{n_2 + n_0^L}{n_{tr}^L + n_0^L} + \frac{1}{\tau_e} \cdot N_2 \quad (4.35)$$

$$A_1^S \cdot G_0^S \cdot \ln \frac{n_1 + n_0^S}{n_{tr}^S + n_0^S} + A_2^S \cdot G_0^S \cdot \ln \frac{n_2 + n_0^S}{n_{tr}^S + n_0^S} - \frac{1}{\tau_{ph}^S} = 0 \quad (4.36)$$

$$A_1^L \cdot G_0^L \cdot \ln \frac{n_1 + n_0^L}{n_{tr}^L + n_0^L} + A_2^L \cdot G_0^L \cdot \ln \frac{n_2 + n_0^L}{n_{tr}^L + n_0^L} - \frac{1}{\tau_{ph}^L} = 0 \quad (4.37)$$

This yields also a linear dependence between the two bias currents:

$$I_2 = \frac{\eta_1}{\eta_2} \cdot \frac{A_2^L g_{2,0}^L}{A_1^L g_{1,0}^L} \cdot \left(I_1 - \frac{1}{\tau_e} \cdot qN_{1,0} \right) + \frac{1}{\tau_e} \cdot qN_{2,0} \quad (4.38)$$

Equations (4.33) and (4.38) delimitate in the (I_1, I_2) coordinates the region where both modes are lasing at the same time, i.e. the dual-wavelength working region. These relations are represented graphically in Figure 4.3 with the label ‘‘C’’.

One may also be interested to find the dependence between the two bias currents for a certain, constant output power emitted in either mode.

D. Inside the ‘‘one mode lasing’’ regions

In order to find the $I_2=f(I_1)$ for a constant (non-zero) output power in the long-wavelength mode while the short-wavelength mode is below threshold, we solve the system (4.11-14) for $N_{ph}^S = 0$ and $N_{ph}^L > 0$. Only the threshold equation (4.14) is valid since the short-wavelength mode is under threshold. In this case the equations can be written:

$$\frac{\eta_1 I_1}{q} = A_1^L \cdot N_{ph}^L \cdot G_0^L \cdot \ln \frac{n_1 + n_0^L}{n_{tr}^L + n_0^L} + \frac{1}{\tau_e} \cdot N_1 \quad (4.39)$$

$$\frac{\eta_2 I_2}{q} = A_2^L \cdot N_{ph}^L \cdot G_2^L \cdot \ln \frac{n_2 + n_0^L}{n_{tr}^L + n_0^L} + \frac{1}{\tau_e} \cdot N_2 \quad (4.40)$$

$$A_1^L \cdot G_0^L \cdot \ln \frac{n_1 + n_0^L}{n_{tr}^L + n_0^L} + A_2^L \cdot G_0^L \cdot \ln \frac{n_2 + n_0^L}{n_{tr}^L + n_0^L} - \frac{1}{\tau_{ph}^L} = 0 \quad (4.41)$$

The non-linear equation (4.39) has to be solved for the carrier density N_1 as a function of I_1 . This can be done both numerically and in closed-form using the ‘‘Lambert’s W’’ function [2,3]. Equation (4.41) gives the dependency between the two carrier densities $N_2=f(N_1)$. In this manner, equation (4.40) yields the $I_2=f(I_1)$ dependency.

A similar procedure has been carried out to find the $I_2=f(I_1)$ for a constant (non-zero) output power in the short-wavelength mode while the long-wavelength mode is below threshold. The system of equations used is equivalent with the above system written for the short wavelength mode:

$$\frac{\eta_1 I_1}{q} = A_1^S \cdot N_{ph}^S \cdot G_0^S \cdot \ln \frac{n_1 + n_0^S}{n_{tr}^S + n_0^S} + \frac{1}{\tau_e} \cdot N_1 \quad (4.42)$$

$$\frac{\eta_2 I_2}{q} = A_2^S \cdot N_{ph}^S \cdot G_2^S \cdot \ln \frac{n_2 + n_0^S}{n_{tr}^S + n_0^S} + \frac{1}{\tau_e} \cdot N_2 \quad (4.43)$$

$$A_1^S \cdot G_0^S \cdot \ln \frac{n_1 + n_0^S}{n_{tr}^S + n_0^S} + A_2^S \cdot G_0^S \cdot \ln \frac{n_2 + n_0^S}{n_{tr}^S + n_0^S} - \frac{1}{\tau_{ph}^S} = 0 \quad (4.44)$$

The theoretical curves obtained with these two systems are labeled with “D” in Figure 4.6.

A special case is realized when the top cavity lases and the bottom cavity is biased such that all the carriers are extracted from the corresponding QWs (typically bottom cavity under reverse-bias). In this situation, the meaning of I_2 is not of an injection current any longer, but that of a photo-current which is extracted from the system, therefore it will be negative. In order to treat this specific case, one has to add to the previous mentioned conditions ($N_{ph}^S > 0$, $N_{ph}^L = 0$, equations (4.39-41)) the fact that all the carriers are extracted from the bottom active region, i.e. $N_2 = 0$. The equations used for this particular case are:

$$\frac{\eta_1 I_1}{q} = A_1^S \cdot N_{ph}^S \cdot G_0^S \cdot \ln \frac{n_1 + n_0^S}{n_{tr}^S + n_0^S} + \frac{1}{\tau_e} \cdot N_1 \quad (4.45)$$

$$\frac{\eta_2 I_2}{q} = A_2^L \cdot N_{ph}^L \cdot G_2^L \cdot \ln \frac{n_0^L}{n_{tr}^L + n_0^L} \quad (4.46)$$

$$A_1^L \cdot G_0^L \cdot \ln \frac{n_1 + n_0^L}{n_{tr}^L + n_0^L} + A_2^L \cdot G_0^L \cdot \ln \frac{n_0^L}{n_{tr}^L + n_0^L} - \frac{1}{\tau_{ph}^L} = 0 \quad (4.47)$$

The solution of this particular case is a single point in the (I_1, I_2) diagram which gives the maximum photocurrent (i.e. all the carriers are extracted) detected in the bottom cavity for a certain output power in the lasing mode of the top cavity. For different values of the input current in the top cavity, the dependence $I_2=f(I_1)$ (labeled with “D1” in Figure 4.6) is given by:

$$I_2 = \frac{\eta_1}{\eta_2} \cdot \frac{A_2^S g_2^S}{A_1^S g_1^S} \cdot \left(I_1 - \frac{1}{\tau_e} \cdot q N_1 \right) \quad (4.48)$$

E. Inside of the dual-mode lasing region

The last investigation aims to find the $I_2=f(I_1)$ dependency for a constant non-zero output power in the long-wavelength mode while the short-wavelength is also above threshold, i.e. the output power for the “S”-mode is also non-zero. The system (4.11-14) is used in its most general form:

$$\frac{\eta_1 I_1}{q} = A_1^S \cdot N_{ph}^S \cdot G_0^S \cdot \ln \frac{n_1 + n_0^S}{n_{tr}^S + n_0^S} + A_1^L \cdot N_{ph}^L \cdot G_0^L \cdot \ln \frac{n_1 + n_0^L}{n_{tr}^L + n_0^L} + \frac{1}{\tau_e} \cdot N_1 \quad (4.49)$$

$$\frac{\eta_2 I_2}{q} = A_2^S \cdot N_{ph}^S \cdot G_0^S \cdot \ln \frac{n_2 + n_0^S}{n_{tr}^S + n_0^S} + A_2^L \cdot N_{ph}^L \cdot G_0^L \cdot \ln \frac{n_2 + n_0^L}{n_{tr}^L + n_0^L} + \frac{1}{\tau_e} \cdot N_2 \quad (4.50)$$

$$A_1^S \cdot G_0^S \cdot \ln \frac{n_1 + n_0^S}{n_{tr}^S + n_0^S} + A_2^S \cdot G_0^S \cdot \ln \frac{n_2 + n_0^S}{n_{tr}^S + n_0^S} - \frac{1}{\tau_{ph}^S} = 0 \quad (4.51)$$

$$A_1^L \cdot G_0^L \cdot \ln \frac{n_1 + n_0^L}{n_{tr}^L + n_0^L} + A_2^L \cdot G_0^L \cdot \ln \frac{n_2 + n_0^L}{n_{tr}^L + n_0^L} - \frac{1}{\tau_{ph}^L} = 0 \quad (4.52)$$

From equations (4.51) and (4.52) one can see that the carrier densities and gain values governing this working regime will be those corresponding to the threshold carrier densities and the threshold gain. The analytical dependence between the two bias currents will be also linear. The straight line describing the $I_2=f(I_1)$ dependency for constant output power in the “L”-mode are parallel with those given by (4.33) – the threshold for the “L”-mode while the “S”-mode is lasing:

$$I_2 = \frac{\eta_1}{\eta_2} \cdot \frac{A_2^S g_{2,0}^S}{A_1^S g_{1,0}^S} \cdot \left(I_1 - A_1^L \cdot g_{1,0}^L \cdot qN_{ph}^L - \frac{1}{\tau_e} \cdot qN_{1,0} \right) + A_2^L \cdot g_{2,0}^L \cdot qN_{ph}^L + \frac{1}{\tau_e} \cdot qN_{2,0} \quad (4.53)$$

Analogously we obtain the dependency for the case when a constant output power is set for the “S”-mode, while the “L”-mode is also above threshold:

$$I_2 = \frac{\eta_1}{\eta_2} \cdot \frac{A_2^L g_{2,0}^L}{A_1^L g_{1,0}^L} \cdot \left(I_1 - A_1^S \cdot g_{1,0}^S \cdot qN_{ph}^S - \frac{1}{\tau_e} \cdot qN_{1,0} \right) + A_2^S \cdot g_{2,0}^S \cdot qN_{ph}^S + \frac{1}{\tau_e} \cdot qN_{2,0} \quad (4.54)$$

One can notice that inside the dual-wavelength operation region, the constant-output power curves in the (I_1, I_2) diagram are straight lines parallel to the corresponding threshold lines that delimitate this working regime labeled with “E” in Figure 4.6.

Table I summarizes the operating regimes investigated above, indicating the labels that identify them on the graphic in Figure 4.3 and Figure 4.6 as well as the conditions to be imposed to the system of equations (4.11-14) for each case.

TABLE I
OPERATING REGIMES OF THE CC-VCSEL

Operating regime	Curve label	N_{ph}^S	N_{ph}^L	Threshold condition @ λ_S	Threshold condition @ λ_L
No lasing		=0	=0	-	-
Double-threshold point	A	=0	=0	satisfied	satisfied
λ_S @ threshold λ_L below threshold	B	=0	=0	satisfied	-
λ_L @ threshold λ_S below threshold	B	=0	=0	-	satisfied
λ_S @ threshold λ_L above threshold	C	=0	>0	satisfied	satisfied
λ_L @ threshold λ_S above threshold	C	>0	=0	satisfied	satisfied
λ_S above threshold λ_L below threshold	D	>0	=0	satisfied	-
λ_L above threshold λ_S below threshold	D	=0	>0	-	satisfied
λ_S above threshold λ_L above threshold	E	>0	>0	satisfied	satisfied

4.3 Experiment and theory – comparison

As explained in the description of the device (Section II), the double-mesa structure of the CC-VCSEL allows independent electrical pumping of the two cavities. The experimental results presented here are obtained under pulsed operation for both cavities with frequency 1 kHz and duty cycle 1%, which corresponds to a period of 1 ms and a pulse-width of 10 μ s. Two pulse generators (Agilent 8114A 100V/2A Pulse Generator and Hameg HM8310 Programmable Function Generator) have been used to electrically pump the two cavities, one of them (Agilent) triggering the other one (Hameg) in order to synchronize the electrical pulses for the two active regions. All measurements have been performed at room-temperature. As we demonstrated in the previous section using the rate equations, the threshold for each mode is a function of both bias currents. Experimentally, the threshold curves in the (I_1, I_2) diagram are presented in Figure 4.2. One can clearly notice the four operating regimes of the device: the “no-lasing” region, the single-mode lasing region on either wavelength or the dual-

wavelength lasing region. For comparison, we present in Figure 4.3 the calculated threshold curves that show a very similar behavior as the experimental ones. The following parameters have been used in order to plot the threshold curves in Figure 4.6: $\xi_1^S = \xi_1^L = 1.63$; $\xi_2^S = \xi_2^L = 1.92$; $\Gamma_1^S = \Gamma_2^L = 0.76$; $\Gamma_1^L = \Gamma_2^S = 0.24$ – have been calculated with the transmission matrix model; $e=8\text{nm}$; $p_1=4$; $p_2=2$ – the actual structure parameters; $S=100\ \mu\text{m}^2$ – estimated area of the oxide aperture; $\tau_{ph}^S = 0.289\text{ps}$, $\tau_{ph}^L = 0.257\text{ps}$ – calculated with the confinement factors $\Gamma_i^{S,L}$ and the mirror reflectivity values of the actual structure: transmission of the top mirror: $T_1=0.6\%$, transmission of the bottom mirror: $T_2=0.86\%$, loss in the coupling mirror: $A=0.42\%$; $\tau_e=1\text{ns}$, $G_0^S = 1800\text{cm}^{-1}$; $G_0^L = 2000\text{cm}^{-1}$; $n_0^S = 0.4 \cdot 10^{18}\text{cm}^{-3}$; $n_0^L = 0.4 \cdot 10^{18}\text{cm}^{-3}$; $n_{tr}^S = 1.8 \cdot 10^{18}\text{cm}^{-3}$; $n_{tr}^L = 1.8 \cdot 10^{18}\text{cm}^{-3}$ – taken from literature (ref. [1]).

Both experimental and theoretical results in Figure 4.2 and Figure 4.3 confirm the results reported previously [4] on a similar structure. The threshold being a function of both currents, one can see that the decrease of the bias current in one cavity increases the current in the other cavity necessary to reach threshold. The threshold for the short-wavelength mode can be reached even for a zero current in the bottom cavity, i.e. with the bottom cavity acting as a passive absorber.

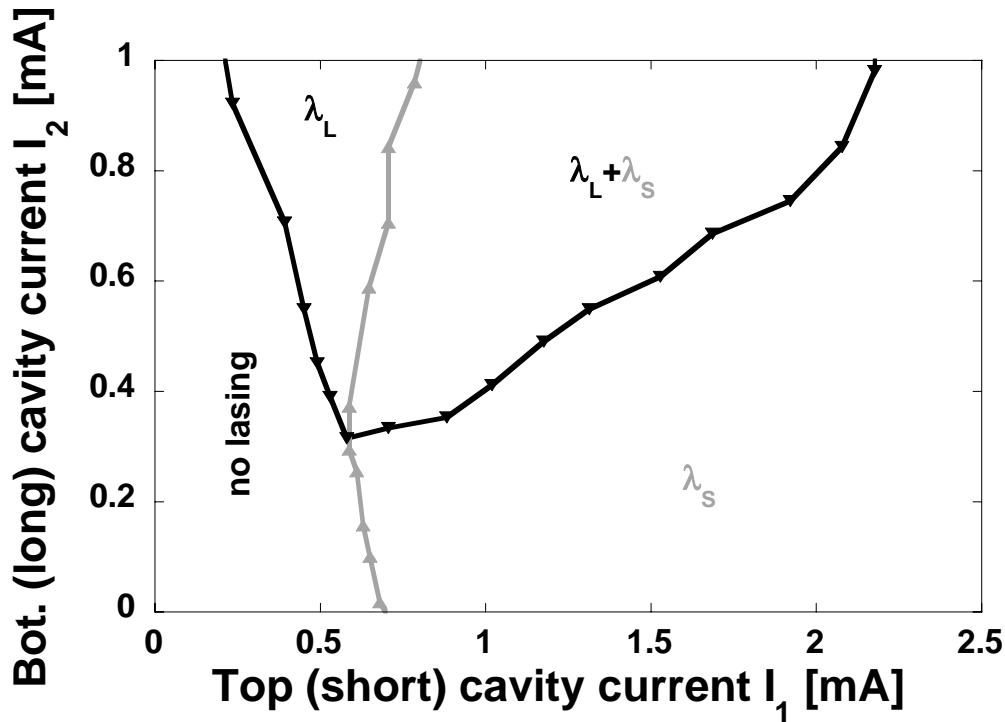


Figure 4.2: Threshold for each mode as a function of the bias currents (experimental).

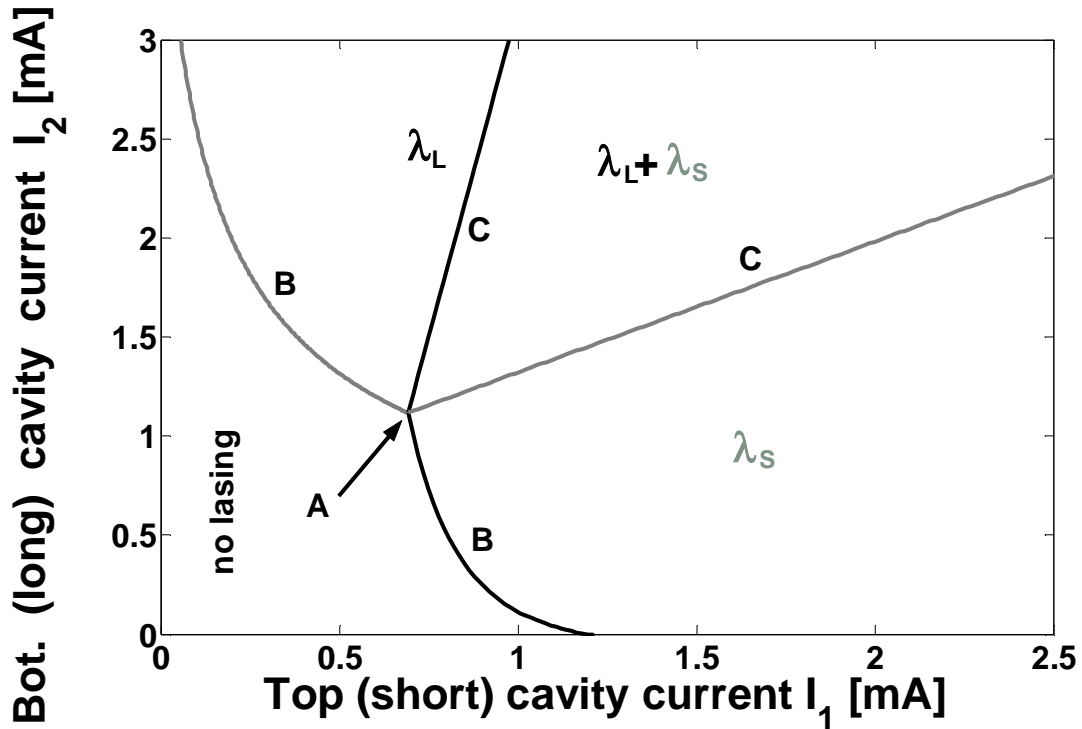


Figure 4.3: Threshold for each mode as a function of the bias currents (calculated).

The two longitudinal coupled non-degenerate optical modes are localized at 927nm and 953nm. Figure 4.4 shows representative emission spectra for each lasing region of the device.

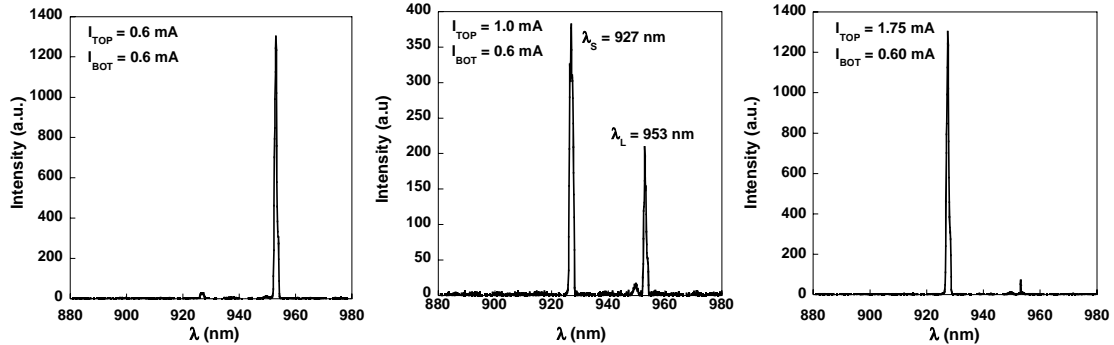


Figure 4.4: Representative spectra for each lasing region: a) long wavelength mode at 953 nm; b) dual-wavelength region; c) short wavelength mode at 927 nm.

Figure 4.5 presents a quasi-three dimensional diagram where one can see the dependency between the bias currents for different constant values of the output power for each mode. As predicted by the rate-equation model in Section 4.3, the curves corresponding to different constant output powers for the “L”-mode inside the dual-wavelength operating region are approximately parallel to the threshold curve for the “L”-mode that delimitates this region. The curves for the “S”-mode show the same behavior in agreement with the theory. For comparison Figure 4.6 shows the calculated curves that correspond to three different numbers of photons for each mode respectively,

which means actually three different output powers. The two families of curves in Figure 4.6 are calculated according to the algorithm presented in the previous section.

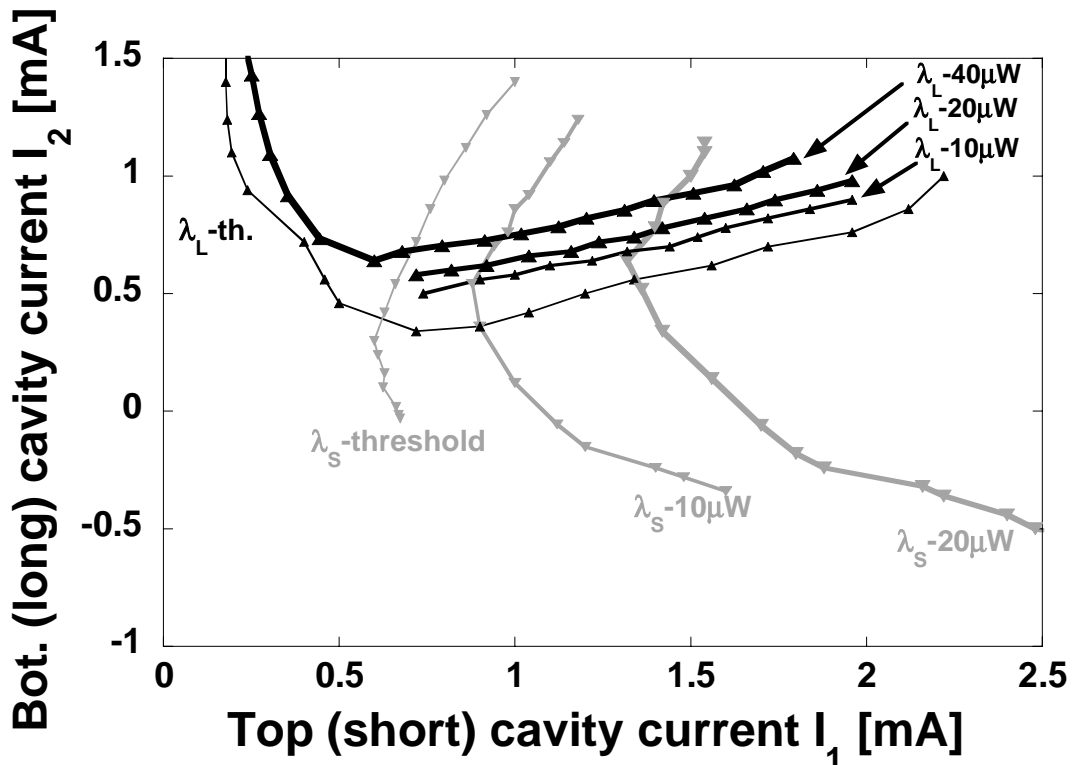


Figure 4.5: Quasi-3D phase-diagram: spectral resolved constant level curves for the output power as a function of the bias currents (experimental).

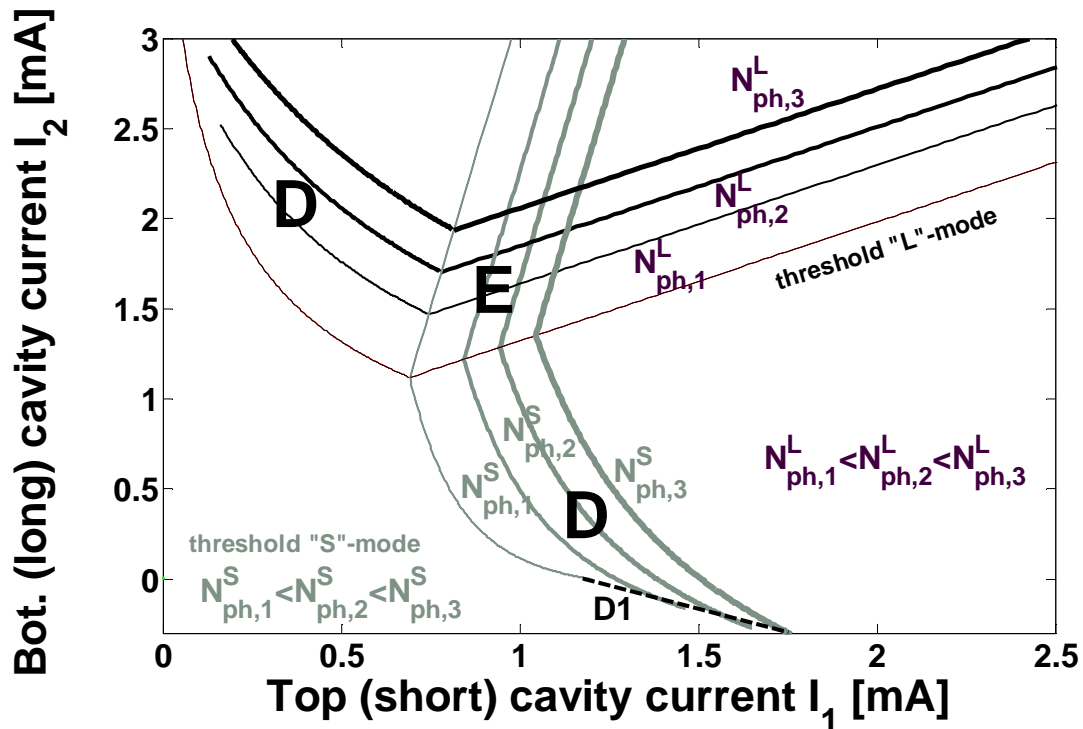


Figure 4.6: Quasi-3D phase-diagram: spectral resolved constant level curves for the output power as a function of the bias currents (calculated).

In order to completely characterize the CC-VCSEL device, one can perform a scan over one of the bias currents (for instance I_1) for a constant value of the other current (I_2) for different parameters of interest such as the spectrally resolved output power (Figure 4.8) or the carrier density in each active region (Figure 4.9). A good qualitative agreement is obtained between the experimental L-I curves (Figure 4.7) and the calculated ones (Figure 4.8). When increasing the top (short) cavity current I_1 at a constant bottom (long) cavity current $I_2=1.5$ mA (Figure 4.8), the threshold for the long-wavelength mode is reached at approx. 0.4 mA. The short-wavelength mode starts lasing at around 0.75 mA, the device entering the dual-wavelength lasing regime. The competition between the two modes determines the switch-off of the long-wavelength mode at $I_1=1.25$ mA. A discontinuity in the slope of the short-wavelength mode is noticed simultaneously with the switch-off of the “L”-mode. This is because of the stop of the optical pumping due to the “L”-mode due to the absorption in the long cavity.

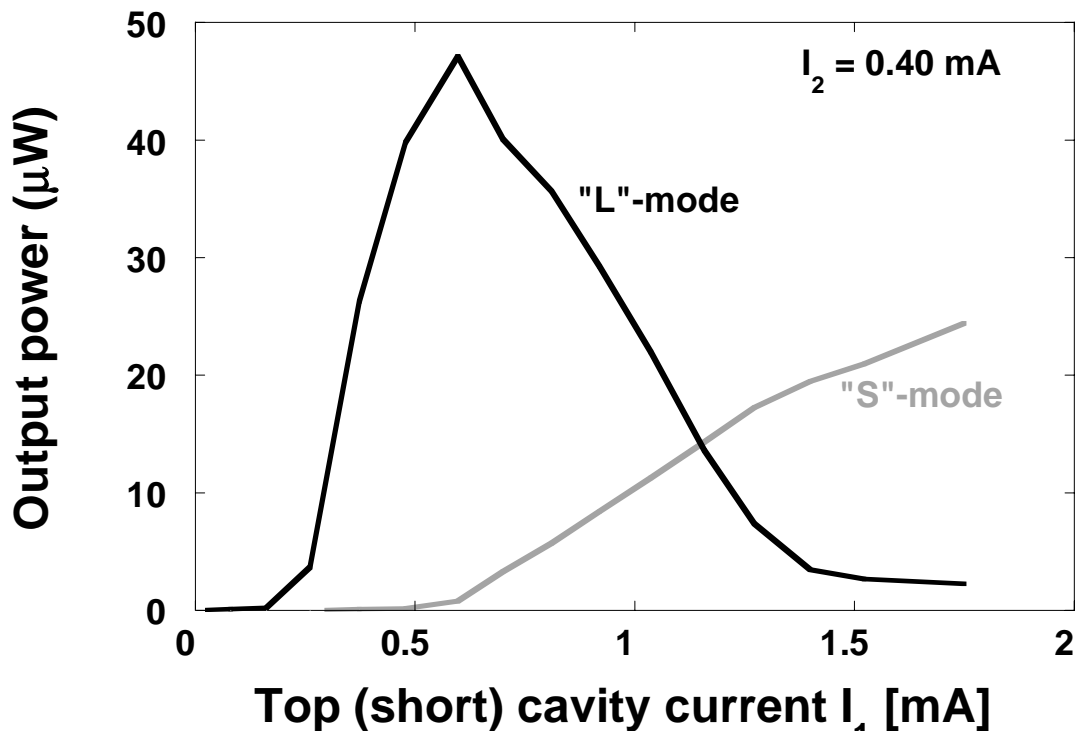


Figure 4.7: Experimental LI curves for a constant value of the current in the bottom cavity $I_2=0.4$ mA.

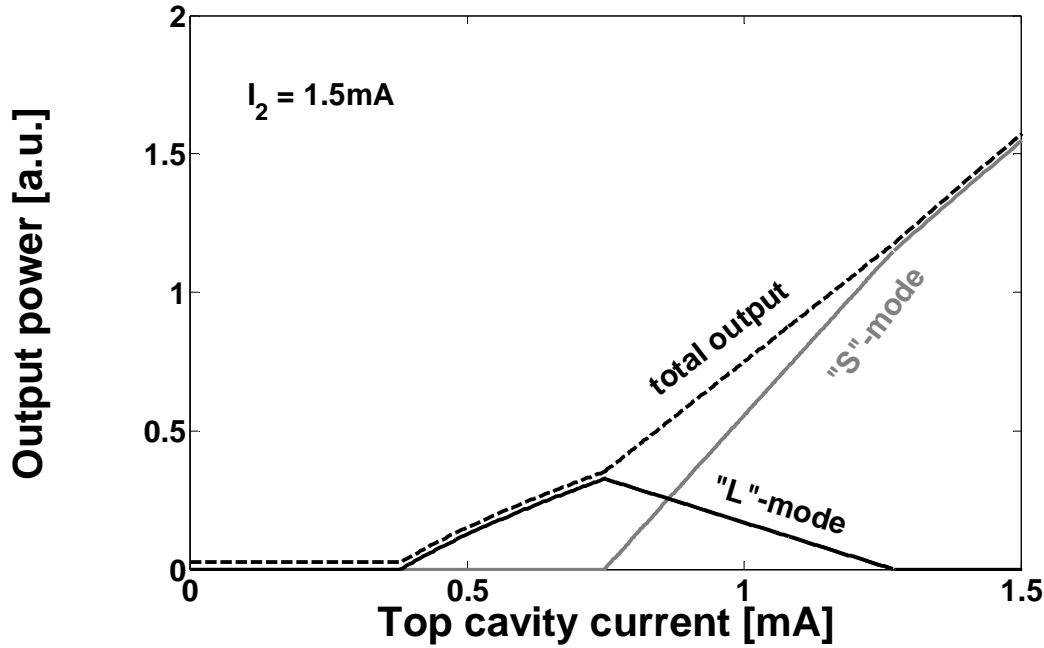


Figure 4.8: Calculated LI curves for a constant value of the current in the bottom cavity $I_2=1.5$ mA.

Figure 4.9 shows the calculated variation of the carrier densities in the active regions of the two cavities as a function of the current in the top cavity, I_1 , for a constant value of the current in the bottom cavity, $I_2=1.5$ mA. According to equation (4.36), the number of carriers in the top cavity varies linearly with the current starting from zero up to the double-threshold point. This dependency remains valid in the one-mode lasing regime as well – equation (4.40). As soon as the device enters the dual-wavelength lasing regime at $I_1 \approx 0.75$ mA, the carrier densities in both cavities are pinned to their double-threshold point values, as both threshold equations are satisfied simultaneously. The value is constant until the long-wavelength mode is quenched. After that, the carrier density in active region “1” continues to increase linearly with the top current, I_1 . The number of carriers in the bottom cavity (maintained at a bias current $I_2=1.5$ mA) starts from a constant, non-zero value given by the constant current. When the mode predominantly located in the bottom cavity – the “L”-mode – starts lasing, the number of carriers in the bottom cavity decreases until the value corresponding to the double threshold is reached and then remains constant during the dual-wavelength lasing. The number of carriers in the bottom cavity continues to decrease when I_1 is further increased beyond the switch-off of the long-wavelength mode.

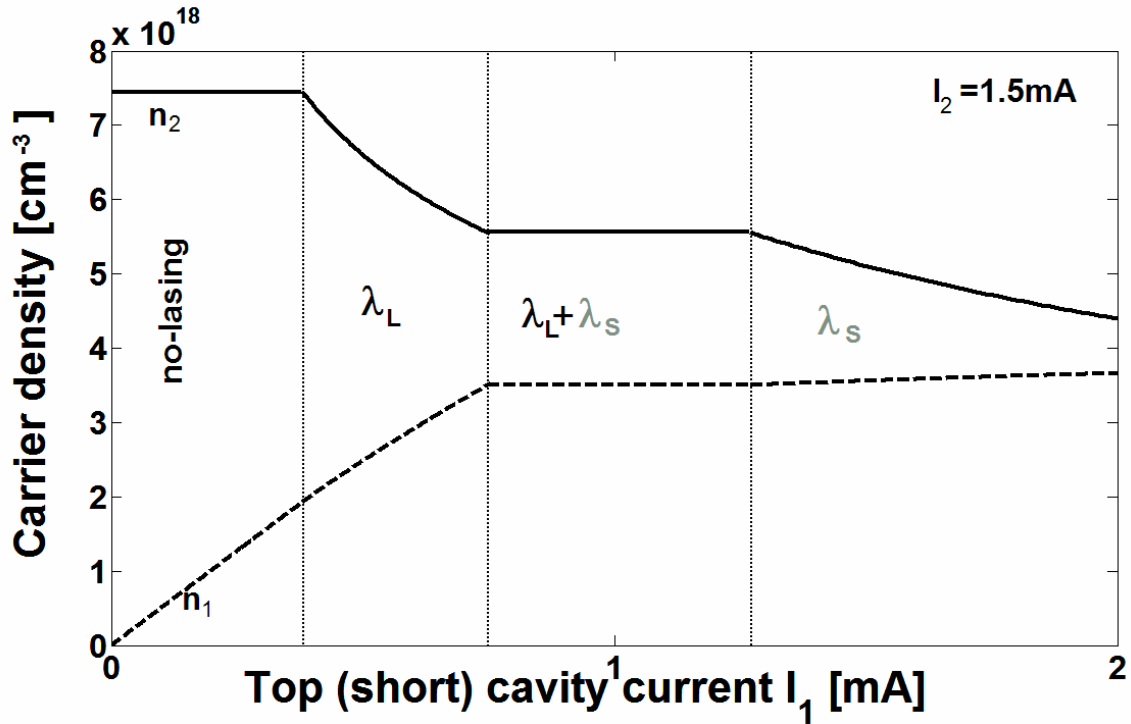


Figure 4.9: Carrier density evolution vs. the bias current of the top cavity for a fixed current in the bottom cavity.

This rate-equation model can be used to simulate different coupled-cavity VCSEL configurations with only the top (short) cavity electrically pumped [5]. In order to obtain simultaneous dual lasing from a device with only one active cavity, some modifications have to be considered in the structure of the device. The operating principle is somehow different in the case of a two-terminal CC-VCSEL. Lasing starts first on the mode localized in the active cavity, in this case the short wavelength mode. The laser output pumps the longer, passive cavity. In order to efficiently pump the passive cavity, the structure is designed so that the short wavelength is absorbed in the passive cavity. This means that the corresponding gain/absorption coefficient has to be negative: $g_2^S < 0$. With increasing injection more power goes into the lasing mode and more power will be absorbed in the passive cavity. With increasing the pump power, the absorption will start to saturate, g_2^S increases towards transparency, and this will decrease the pumping efficiency. But at the same time the gain coefficient corresponding to the long wavelength mode in the passive, longer cavity, g_2^L , will also increase. In order to achieve simultaneous lasing on both modes with a single injection current, one has to design the structure so that $g_2^S < 0 < g_2^L$. If fulfilled this condition insures that the passive cavity transfers energy from the mode that lases initially (“S” mode) to the other mode.

The basic design rule to obtain dual wavelength lasing with only one electrically pumped cavity is to increase the reflectivity of the top mirror, while tuning the bottom mirror reflectivity together with the other device parameters. The mirror parameters used for these calculations are:

transmission of the top mirror: $T_1=0.45\%$, transmission of the bottom mirror: $T_2=1.16\%$ and the loss in the coupling mirror: $A=0.42\%$.

Figure 4.11 and Figure 4.11 demonstrate the dual-wavelength emission from a two terminal CC-VCSEL device, i.e. with only one active cavity. This result theoretically confirms the previously reported experimental data in reference [5] – Figure 4.11.

This case is treated starting from the usual system of equations (4.11-14), imposing $I_2=0$ as well as the previously discussed conditions for different operating regimes.

One can notice in Figure 4.11 a region of bistability close to the threshold current corresponding to the short wavelength mode. While the device is still below threshold, the absorption in the passive cavity is very high (eq. 4.21). As soon as the threshold is reached, the passive cavity is photo-pumped by the radiation on the short wavelength mode, thus approaching the transparency. Therefore a current which is lower than the initial threshold is enough to maintain the laser emission. This result is also similar to what has been experimentally observed in [6] by Fisher et al.: a monolithic coupled-resonator vertical-cavity laser which exhibits bistable behavior in the light output versus injection current. The bistability regions reported in [6] are quite large and are positioned at the peak of the lasing output power. According to our model the width of this bistable region is very sensitive to different design parameters. Smaller detuning between the two cavities is expected to increase the bistability as the optical field of the “S”-mode penetrates more into the passive cavity

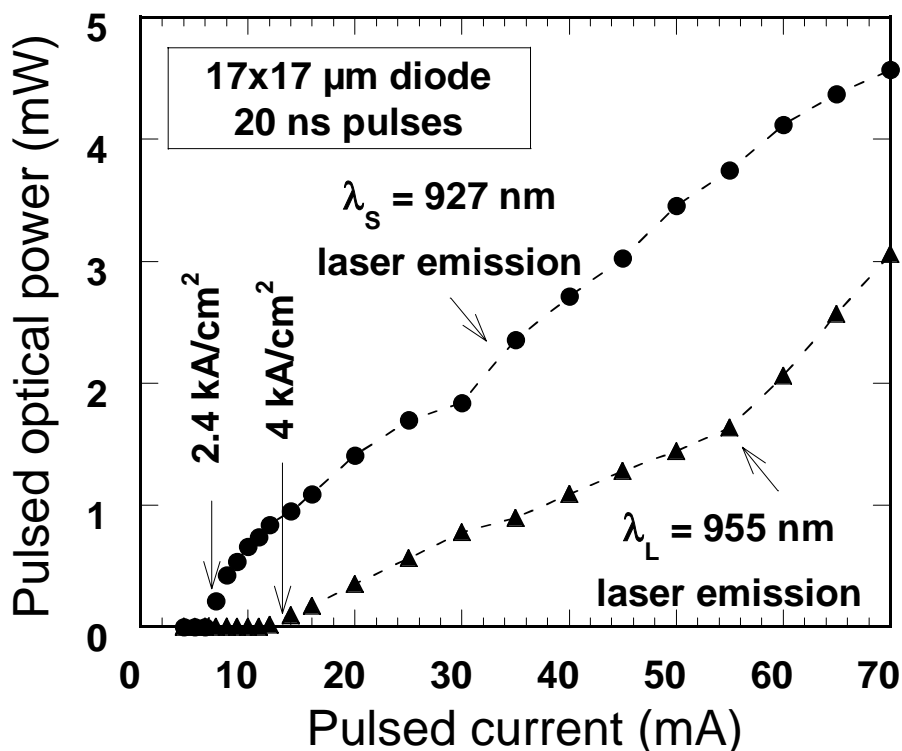


Figure 4.10: Light Output power vs. pulsed current intensity for a single active-cavity CC-VCSEL (experimental) [5].

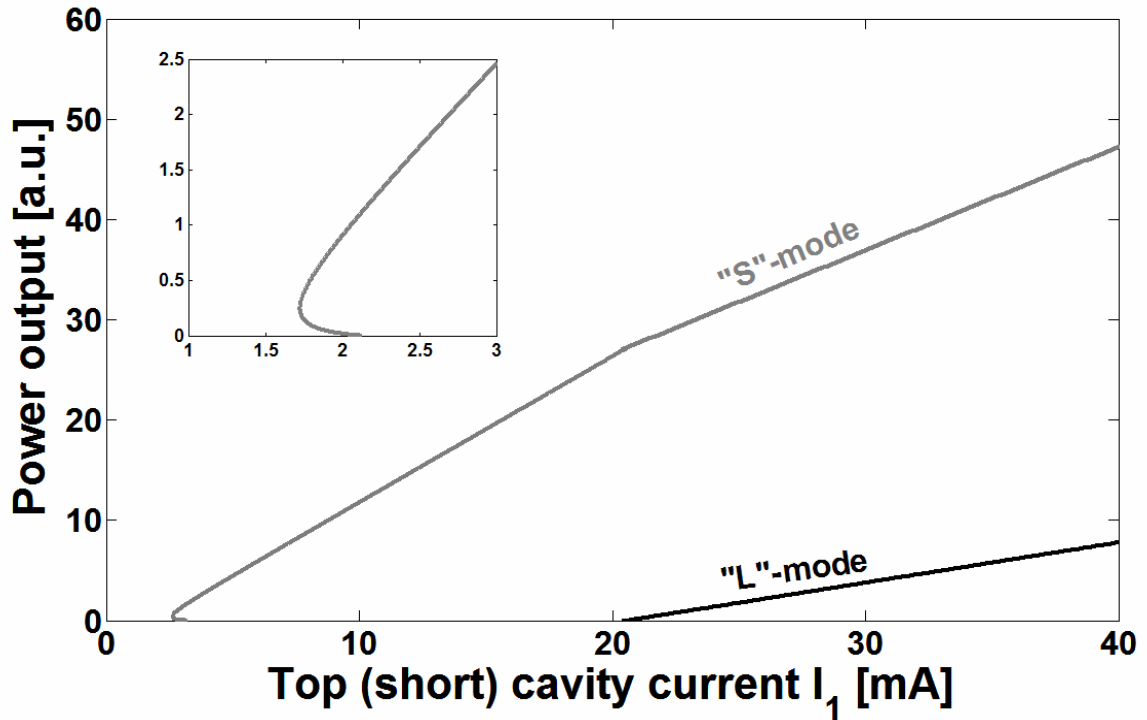


Figure 4.11: Calculated light output power vs. current intensity for a single active cavity CC-VCSEL.

4.4 CC-VCSEL behavior for high injection currents

In order to completely describe the behavior of the coupled-cavity VCSEL device, we have to mention what happens for higher injection currents.

For values of the injection current in the bottom cavity higher than $I_2 = 0.9$ mA, a new mode, called hereafter “the oxide-mode”, appears in the output spectrum of the BiVCSEL device. An extended “phase-diagram” is presented in Figure 4.12 for higher injection currents. The threshold curve that corresponds to the oxide-mode intersects the threshold curve for the long wavelength mode at $I_1 = 2.2$ mA. Beyond this point the long wavelength mode is switched off. This fact suggests a strong competition between the λ_L -mode and the oxide mode. One can see that as soon as the two threshold curves cross each other the λ_L -mode is switched-off. This indicates that the parasitic oxide-mode is localized in the same region as the long-wavelength mode.

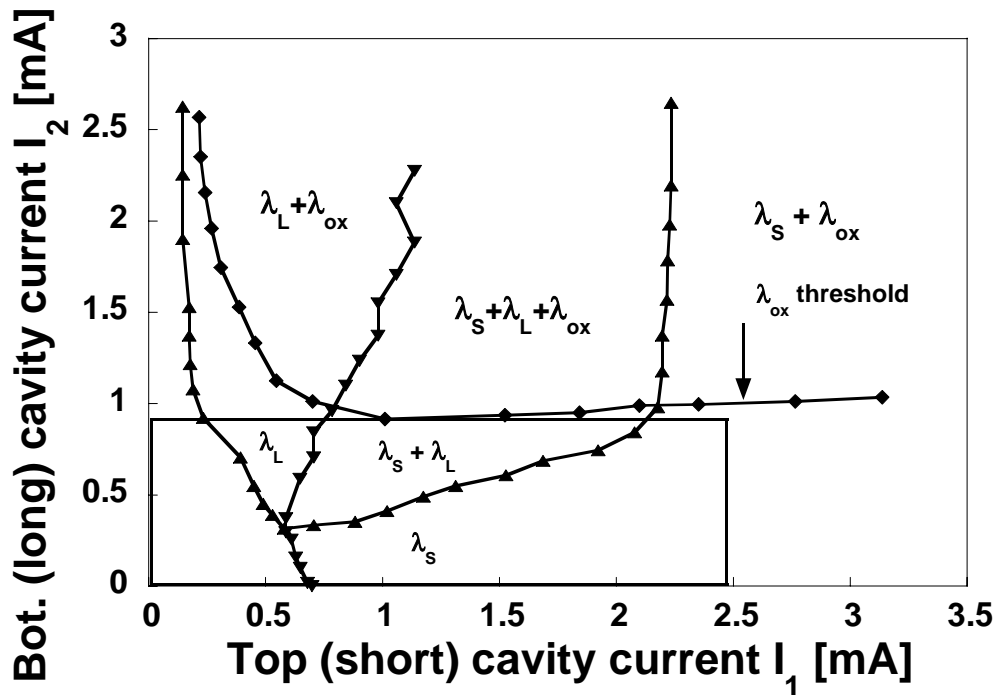


Figure 4.12: Extended “phase-diagram” for the CC-VCSEL device.

Moreover, Figure 4.13 presents the evolution of this mode for different injection currents in the bottom cavity while maintaining the same current in the top cavity. The intensity of the oxide-mode increases with the current in the bottom cavity and as a result of this competition the long-wavelength mode is switched-off.

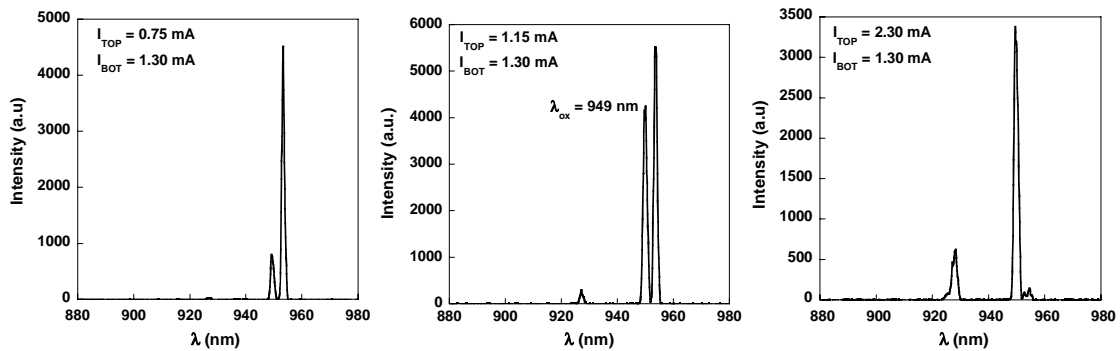


Figure 4.13: Evolution of the oxide-mode vs. current in the top cavity.

4.5 Conclusions

We have developed in this Chapter a rate-equation model which is an engineering toolbox for the coupled-cavity VCSEL device. One can use this model to determine the bias conditions for the different operating regimes, either one-mode lasing, or simultaneous dual-mode lasing. Actually the model provides all the relevant parameters of the device – gain coefficients, number of carriers in each active cavity, power output in each lasing mode – knowing the bias currents. We have shown that one

can also use this model to design a coupled-cavity VCSEL device that is able to lase simultaneously on two wavelengths with one single active cavity, i.e. electrically pumping only one cavity.

Laser emission in two optical modes is possible in the case of a coupled-cavity VCSEL device because there are two active regions, two separate regions that provide optical gain. We have shown in the present rate-equation model that in the one-mode operating regime the gain coefficients and the carrier densities are not pinned as in the case of a classical laser. The threshold equation for only one lasing mode imposes only a dependency between the gain coefficients for the corresponding mode in the two gain/absorption sections, but not clamping of the gains. The two bias currents move the weight of the global gain from one cavity to the other. In this manner, the second resonant mode in the cavity may also reach the threshold, thus achieving simultaneous lasing in two optical modes. We demonstrate that this is the operating regime analogous to a classical laser because it is only in the dual-mode lasing that all the gain coefficients are pinned as well as the carrier densities in both active cavities.

In order to emphasize the physical interpretation it is worth mentioning that other authors (e.g. the group of Choquette and co-workers [7]) have introduced the term of “apparent/effective threshold current” speaking about the bias current in one cavity necessary to achieve lasing while also pumping the other active cavity, suggesting the interplay between the two bias currents in defining the threshold condition. They also suggest the variable QW absorption/gain through the second bias current as a mechanism for the change of the “effective threshold current”.

Bibliography CHAPTER 4

[1] L. A. Coldren and S. W. Corzine, *Diode Lasers and Photonics Integrated Circuits*, J. Wiley N.Y., 1995.

[2] <http://www.mathworks.com/access/helpdesk/help/toolbox/symbolic/lambertw.shtml>.

[3] R. M. Corless, G. H. Gonnet, D. E. G. Hare, and D. J. Jeffrey, “On Lambert's W Function”, *Technical Report*, Dept. of Applied Math., Univ. of Western Ontario, London, Ontario, Canada available by anonymous FTP from cs-archive.uwaterloo.ca.

[4] V. Badilita, J.-F. Carlin, M. Brunner, and M. Ilegems, “Light-current characterization of dual-wavelength VCSELS”, *Proc. SPIE*, **4649**, pp. 87–95 (2002).

[5] J.-F. Carlin, R.P. Stanley, P. Pellandini, U. Oestertle, and M. Ilegems, “The dual wavelength Bi-vertical cavity surface-emitting laser”, *Appl. Phys. Lett.*, **75**, pp. 908-910 (2000).

[6] A.J. Fisher, W.W. Chow, K.D. Choquette, A.A. Allerman, and K.M. Geib, “Q-switched operation of a coupled-resonator vertical-cavity diode”, *Appl. Phys. Lett.*, **76**, pp. 1975-1977 (1999).

[7] D.M. Grasso, K.D. Choquette, *IEEE J. of Quantum Electronics*, **39**, pp. 1526 (2003).

Chapter 5*

Polarisation switching in CC-VCSELs

5.1 Introduction: Experimental data on polarization switching in VCSELs

The polarisation properties of the light emitted by a semiconductor laser are determined by the polarisation properties of the gain, i.e. by the interband optical transition matrix element, and by the polarisation properties of the optical cavity. Because of VCSEL surface emission the transition matrix element is the same for all light polarisation directions in the plane of the active layer. Moreover, the conduction band (CB) – heavy hole (HH) transitions are dominant (the band edge value of the transition matrix element is 1/2 compared to 1/6 for CB – light hole (LH) transitions) implying that mainly CB – HH transitions determine the form of the gain. This is in clear contrast with what happens in EELs, where the transition matrix element is different for light polarised in the plane of the QW and perpendicular to it. Also, mainly CB – HH transitions contribute for the in-plane polarised emission while mainly CB – LH transitions contribute to the out-of-plane polarized emission. The optical confinement is also different in VCSELs and EELs: usually a symmetric cylindrical or rectangular aperture is defined by oxidation, air-post or proton implantation in VCSELs. On the contrary, the different lateral and transverse dimensions of the EEL waveguide give rise to waveguiding and reflectivity anisotropy. In summary, *in contrast with EELs there is no intrinsic polarisation anisotropy mechanism in VCSELs.*

Nevertheless, VCSELs do preferentially emit linearly polarised light along [110] and [1-10] crystallographic directions [1]. This has been attributed to the residual stress after manufacturing and/or to the electro-optic effect [2,3], leading to cavity in-plane birefringence and dichroism [2,3]. As a result, two linearly polarized modes with slightly different gains are supported by the VCSEL cavity. Experimentally, it is found that these two modes do not lase simultaneously and that sometimes when the injection current is increased, switching between them occurs [4,5,6]. A polarisation resolved light versus current (L-I) characteristic of proton implanted GaAs/AlGaAs QW VCSEL emitting around

* Section 5.4 (Control of polarization switching in CC-VCSELs) of this chapter is based on the paper:

- V. Badilita, J.-F. Carlin, M. Ilegems, M. Brunner, G. Verschaffelt, K. Panajotov, "Control of Polarization Switching in Vertical Coupled-Cavities Surface Emitting Lasers", *IEEE Photonics Technology Letters*, **16**, pp. 365-367, 2004.

850nm is shown in Figure 5.1 [5]. Polarisation switching (PS) is observed in the fundamental Gaussian transverse mode when operating with direct current (DC) but not for short pulse current operation. The current at which the PS occurs changes from one laser to another. It also depends on the laser substrate temperature. Looking at the spectrum of the emitted light, we identify the PS to be from higher frequency ν_H mode (thin line) to lower frequency ν_L mode (thick line). We shall refer to such kind of PS as type I PS because it is the first one reported [7] and in order to distinguish from the opposite way of switching, namely from lower to higher frequency polarisation mode which we call type II PS.

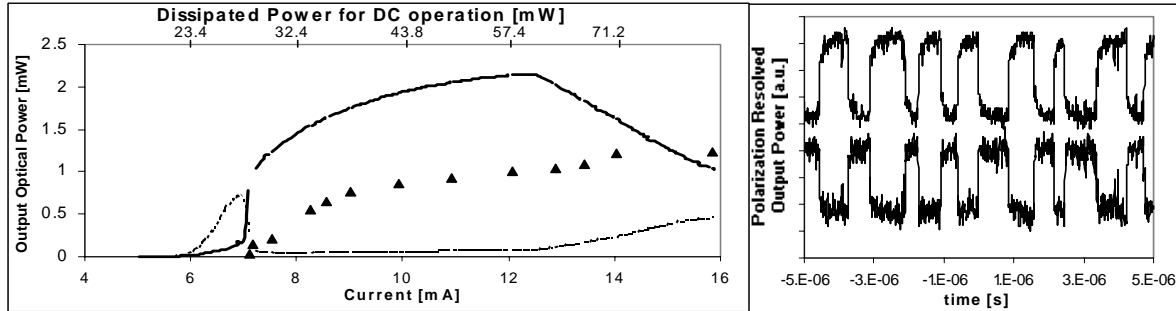


Figure 5.1: (left) L-I curve showing PS between ν_H (thin line) and ν_L (thick line) modes for DC current operation but not for short pulse current (triangles) (right) Time trace of the polarization resolved optical output in the region of PS showing mode hopping behavior [5].

Although one observes an abrupt PS in the steady-state L-I curve, one can notice that the laser continuously jumps between the two well-defined states if the VCSEL is biased in the PS region (Figure 5.1 – right). The time traces of the two polarization modes as observed with fast detectors are shifted vertically for clarity. One can see the perfect anti-correlation between the two polarization-resolved intensities [5]. The time that the laser stays in one mode changes randomly with a mean value called *dwelt time*. If the current where the PS occurs is changed, the dwell time changes in the range of several orders of magnitude. Experimentally, dwell times have been observed scaling with the current of PS from tens of nanoseconds to seconds [8].

If the VCSEL is biased in the region of mode hopping and modulated with a small electrical signal, PS by current modulation is obtained (Figure 5.2). For a frequency of 30MHz, perfect PS is observed (Figure 5.2 left), while at 50 MHz the laser starts to miss the PS from time to time being only intensity modulated at these events (Figure 5.2 right). In such a way, one can define a minimum small signal modulation frequency for PS which in this case is around 30 MHz. Together with the dwell time, which exponentially increases with the PS current [8], the maximum modulation frequency for a given amplitude of the modulation signal scales in a similar but reverse way (Figure 5.3). This behavior is quite similar to the mode hopping between two longitudinal modes in edge emitting lasers [9]. This similarity suggests that the polarization mode hopping is related to the spontaneous emission

noise driven dynamic of a VCSEL working in two longitudinal mode regime rather than to the fact that these two modes have orthogonal polarization.

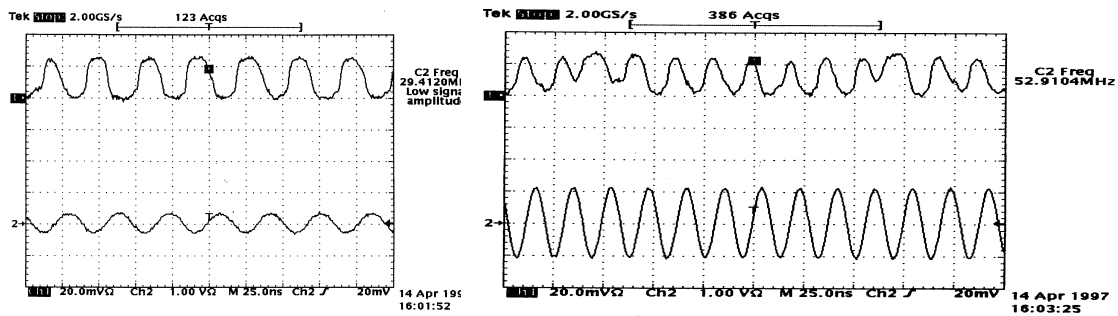


Figure 5.2: Small signal modulation around the PS current: the modulation signal is the bottom trace and the polarization resolved optical signal is the top trace [8].

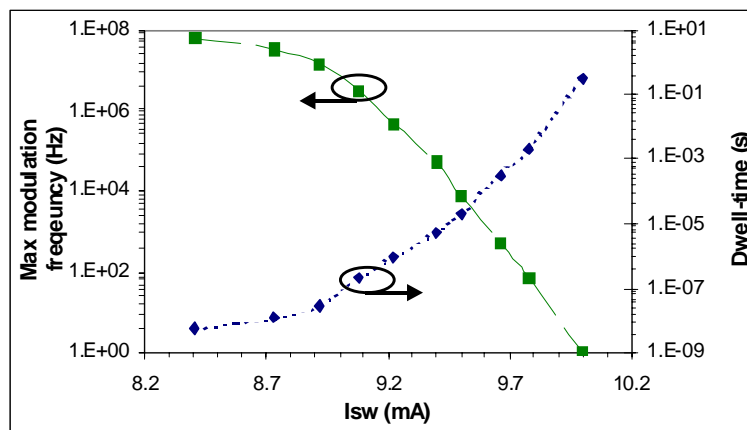


Figure 5.3: Scaling of the dwell time and maximum modulation frequency with the current of PS [8].

A typical feature for VCSELs is that the L-I curve is not linear: the slope of the L-I curve saturates as seen in Figure 5.1. Moreover, if the current is further increased the slope of the L-I curve becomes negative and the lasing action ceases. This behavior is due to the current self-heating combined with the single longitudinal mode operation. As the gain curve red-shifts much faster with temperature than the cavity mode, the increasing misalignment between the gain maximum wavelength and the cavity wavelength increases the lasing threshold current and finally prevents lasing.

The influence of the laser substrate temperature on the VCSELs' polarization behavior has also been investigated [10]. Figure 5.4 shows three typical L-I curves for DC operation at fixed substrate temperatures of 10°C, 15°C and 55°C. It is seen that at low substrate temperature (10°C) only type I PS takes place (Figure 5.4a). For 15°C substrate temperatures (Figure 5.4b) two types of PS occur: from v_H mode to v_L mode (type I PS) followed by a second one in the opposite direction (type II PS). At higher substrate temperatures, between 25 and 55°C only type II PS takes place (Figure 5.4c). The frequency splitting between the two modes of orthogonal linear polarization is 12GHz and remains constant in the range of substrate temperatures for which these measurements are taken.

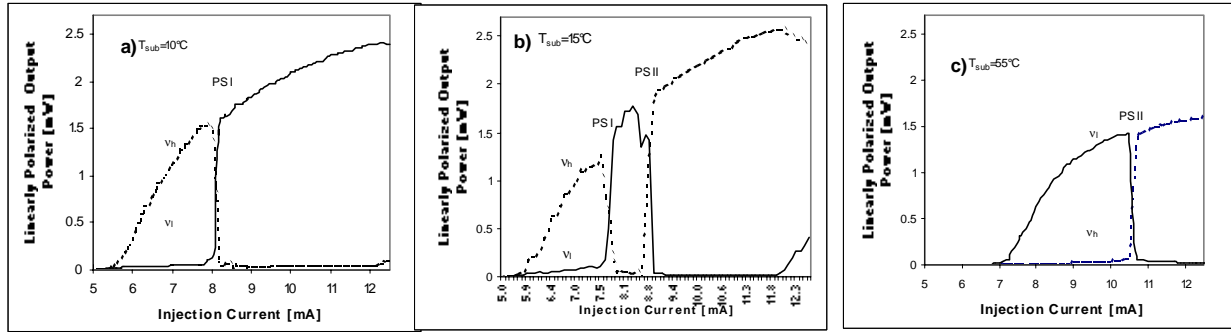


Figure 5.4: Polarization resolved optical output power versus DC injection current characteristic at different substrate temperature: a) 10°C ; b) 15°C ; c) 55°C . Lower (higher) energy mode is shown as full (dashed) line [10].

Although one could expect the PS to be influenced by the thermal waveguiding effect in the proton implanted VCSELs investigated above, quite similar PS behavior has been observed for index-guiding VCSELs, namely the air-post VCSELs fabricated at CSEM, Zürich [11]. The lasers have three 8 nm thick InGaAs QWs emitting around 980 nm with a threshold current of about 2.5 mA. The polarization resolved L-I curves and the optical spectrum are shown in Figure 5.5. Again, PS of type I happens through a region of mode hopping with a similar scaling of the dwell time with the current [8,11].

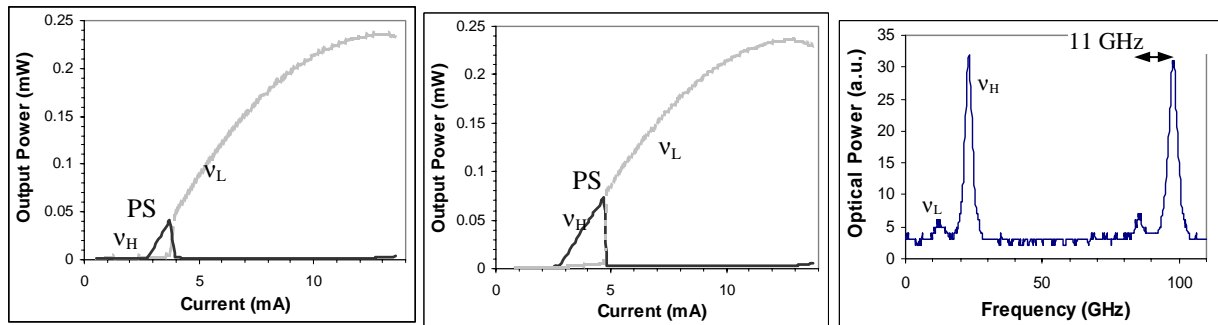


Figure 5.5: PS through mode hopping in air post VCSELs (right). The Fabry-Perot optical spectrum (left) [8].

In oxide confined VCSELs quite different behavior has been observed [11]. Investigations have been performed for a device with InGaAs QWs emitting around 960 nm, with a very small oxide aperture (3-4 μm). The VCSELs are single transverse mode up to the thermal roll-over point at about five times the threshold current. A polarization switch of type I is observed between the two fundamental modes along [110] and [1-10] directions. In this case the PS takes place through a large region of hysteresis (Figure 5.6a). This hysteresis region is also believed to exist in proton implanted and in the air-post VCSELs, but it appears to be masked by the mode hopping behavior. Actually, the spontaneous emission noise drives the VCSEL from one polarization state to the orthogonal one due to the presence of bistability. Another difference in this oxide confined VCSELs is the strong tuning of

the PS current with the substrate temperature. When the oxide aperture is larger, VCSELs with the same structure operate in multiple transverse modes. In this case, the upward PS is in the region where the first higher order transverse mode is already lasing while the downward PS is in the region of the fundamental mode (Figure 5.6b). Still, the PS is of type I between the fundamental modes with orthogonal polarization.

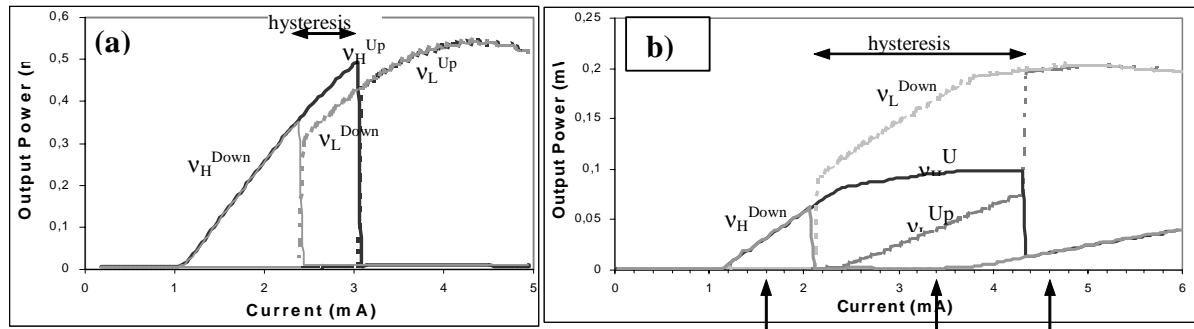


Figure 5.6: PS through hysteresis in oxide-confined VCSELs: (a) small aperture; (b) large aperture [11].

One way to control the PS in VCSELs is the anisotropic in-plane strain. Figure 5.7 shows the results of a series of experiments on VCSELs under an externally applied in-plane anisotropic strain [12]. For uniaxial tensile strain along [1-10] direction of the laser wafer the laser is initially (at small external stress) emitting in the low frequency mode (v_L state). The direction of this linearly polarized state is at about 20° away from the [1-10] direction (Figure 5.7A-a). Increasing the external stress, the direction of this polarization mode is continuously tuned towards the line of the tensile strain and remains in this orientation. Increasing the external stress increases the frequency splitting between the two linearly polarized modes. PS in the fundamental mode is first observed when the strain induced frequency splitting becomes rather large (about 25GHz in Figure 5.7A-b) and appears at quite a high current. This is PS type II [12]. The PS current continuously decreases as the external stress is further increased (Figure 5.7A-c-d). A very broad region of stress – induced PS tuning exists (frequency splitting from 25 GHz to 60 GHz). At about 60 GHz the PS point is moved to threshold (Figure 5.7A-f) and for larger frequency splitting the laser is emitting in the higher frequency mode only, with linear polarization oriented perpendicular to [1-10] direction of the laser wafer.

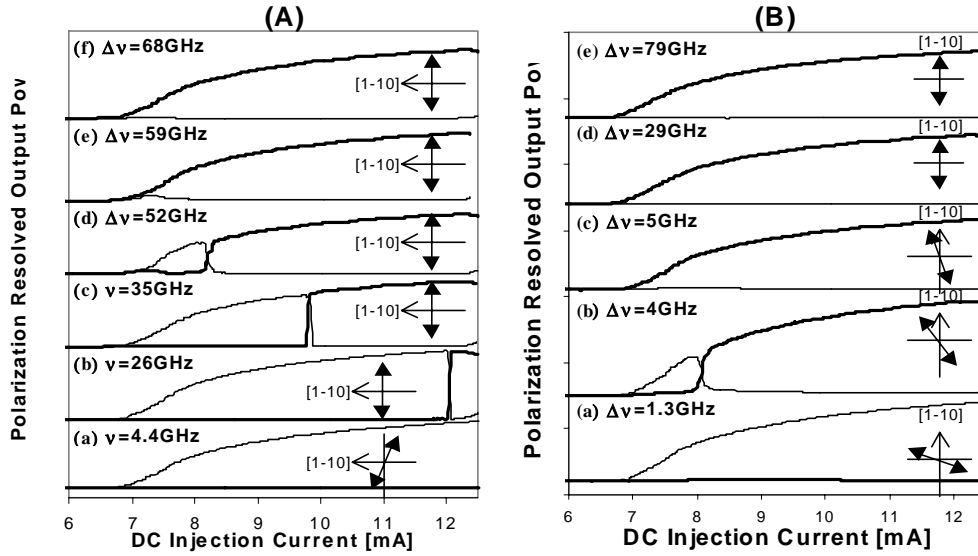


Figure 5.7: Polarization resolved optical output power versus DC injection current for increasing tensile strain along [1-10] (A) and [110] (B) crystallographic directions. The higher (lower) frequency mode is shown by thick (thin) solid line. The orientation of the higher frequency linearly polarized mode is schematically shown [12].

5.2 Different approaches to explain PS in VCSELs

There is no consensus regarding the physics behind the phenomenon of PS in VCSELs and mainly three different explanations have been suggested: a) the first one takes into account the finite spin-flip in semiconductor active material – the so-called spin-flip model (SFM); b) the second one takes into account the modification of net gain with the injection current. This modification can be for the modal gain, determined by the overlap of the optical field with the carrier distribution in the QW: thermal lensing [5] and spatial hole burning effects [13] contribute to such modification; c) the third group relies on the birefringence and the gain anisotropy induced by strain; d) we will also present a quite different point of view on the polarization behavior of VCSELs: the polarization fluctuations are driven by the spontaneous emission noise.

a) The spin-flip model (SFM) [14] starts from the fact that the polarization of the laser light is of quantum nature and it originates in the spin sublevels of the lasing transition between the conduction and the valence bands of the semiconductor. Actually, the rate-equations used in basic modeling of semiconductor laser dynamics take for granted a fixed direction of polarization. A possible explanation for this is a two level model approximation for the semiconductor laser transition. But the semiconductor laser is inhomogeneously broadened with different transitions from the conduction to the valence bands. The two-level approximation can be understood by replacing this transition by a homogeneously broadened transition at the center of the bandgap. Thus, the well-known α -factor of semiconductor lasers is a common way of summarizing in one single parameter a

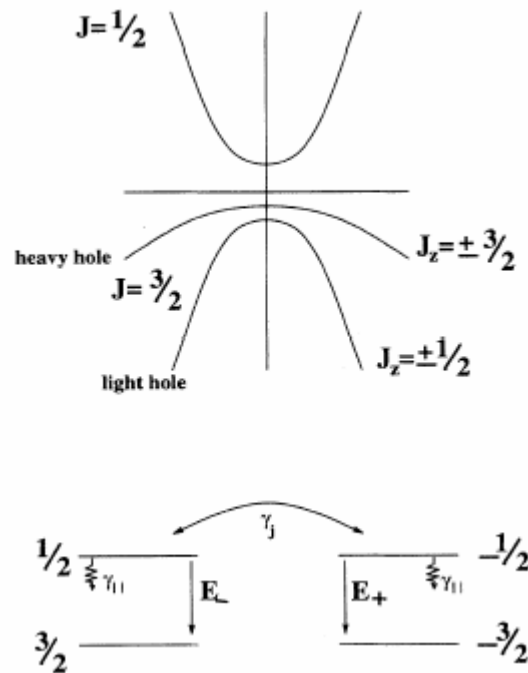


Figure 5.8: Schematic representation of the VCSEL carrier reservoirs (conduction band and HH valence band) divided into two-level subsystems of different spin orientation [14].

series of microscopic processes and in particular the inhomogeneously broadened character of the lasing transition. A main effect of the α -factor is to produce phase sensitive dynamics. Beside the α -factor, the SFM consider 4 levels in order to account for the spin sublevels of the conduction and the valence bands. For bulk material, the heavy-hole (hh) and the light-hole (lh) bands are degenerate at the center of the bandgap with a total angular momentum $J = 3/2$. For QWs, the quantum confinement removes this degeneracy. In the case of unstrained QWs, the hh band which is associated with $J_z = 3/2$ has a higher energy (fig.). For a VCSEL, considering the z-axis the propagation direction, the electric field is in the x-y plane, so that two independent TE polarization modes are available for the laser field. For such a transverse electric field the allowed dipole transitions are those in which $\Delta J_z = \pm 1$. Right circularly polarized light corresponds to $\Delta J_z = -1$ and left circularly polarized light corresponds to $\Delta J_z = +1$. Because of the lower energy of the lh band, the model doesn't consider transitions from the conduction band to the lh band. Therefore, there are only two allowed transitions between the conduction and the hh band: the transition from $J_z = -1/2$ to $J_z = -3/2$ associated with right circularly polarized light, and the transition from $J_z = 1/2$ to $J_z = 3/2$ associated with left circularly polarized light. In Figure 5.8, $\gamma_{||}$ is the decay rate of the total population difference between the conduction and the valence bands. The coefficient γ_j accounts for the mixing of the populations with opposite values of J_z . If an excess of carriers is present in one of the two subsystems, their spin flips to the opposite orientation with a rate γ_j .

From this four-level model one obtains generalized rate-equations that include the polarization degrees of freedom. It accounts for the vector nature of the laser emission field by allowing for both

states of circular polarization through dipole-allowed transitions between independent pairs of levels. Coupling between both transitions is assumed to occur via spin-flip relaxation processes. The rate equations of the coupled system are analyzed adiabatically eliminating the polarization dynamics. This analysis shows that the relative time scales of the spontaneous emission and the spin-flip relaxation processes are of critical importance in determining the nature of the polarization dynamics and the stability of the linearly polarized laser light field. The SFM model [14] predicts that linearly polarized light should always be emitted by the VCSELs. By taking into account the cavity anisotropy (birefringence and dichroism), PS is also predicted through a region of dynamical instabilities and/or hysteresis [15,16]. The SFM model can explain PS even for a very small dichroism and birefringence. It predicts reversible PS occurs from lower to higher frequency (type II PS). The two types of switching can only be obtained if the SFM is combined with gain equalization model [17].

b) The modification of the net gain with current can also explain PS in VCSELs. Indeed, the specific features of VCSELs - single longitudinal mode operation and current heating due to flow of the current through DBRs - lead to pronounced redshift of the gain curve. This shift is faster than those of the two cavity modes of different polarization. As a result, the laser will operate in higher frequency mode at the lower frequency side of the gain maximum and vice versa [4] (see Figure 5.9 left), i.e. the higher frequency mode is selected when the gain derivative with respect to the photon energy is positive and vice versa. This model explains why type I PS takes place when transiting the gain maximum [4].

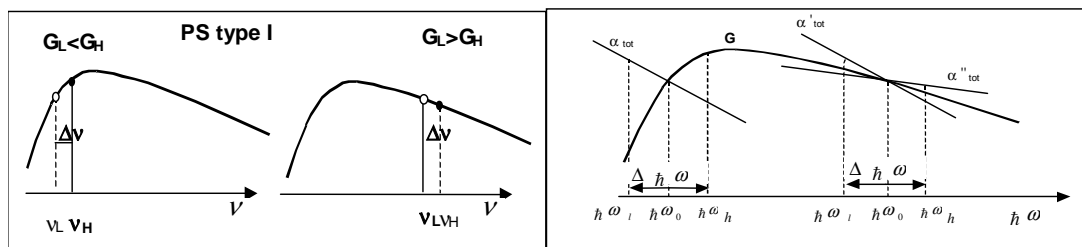


Figure 5.9: Schematic representation of the material gain and two cavity modes: (left) gain curve redshift with current heating giving rise to PS type I; (right) the cavity losses are also shown as a function of photon energy [10].

If one considers the photon energy dependence of the cavity losses this picture, is modified [10]. Here the gain and loss derivatives with respect to the photon energy have to be compared to determine which mode is lasing (see Figure 5.9 right). The intervalence band absorption in the heavily p-doped DBRs decreases when the photon energy increases, so at the low photon energy side of the gain maximum the higher frequency (photon energy) mode is lasing. If the working point is at the high photon energy side of the gain maximum, either the lower or the higher frequency mode can be lasing. The behavior of the gain and loss derivatives is shown in Figure 5.10 as a function of the temperature rise of the VCSEL. The gain derivative is plotted for different initial positions on the gain curve, corresponding to different substrate temperatures (solid curves 1-8). If the loss derivative also depends

on the temperature, its initial value also changes with substrate temperature as illustrated by the two solid lines in Figure 5.10. PS switching now takes place at the crossing of the gain and loss derivatives. Depending on the laser temperature, gain offset, etc. different situations are possible: PS type I at the higher frequency side of the gain maximum or PS type I followed by PS type II as experimentally observed (see section II). Fast PS at constant lattice temperature can also be explained by carrier heating [18].

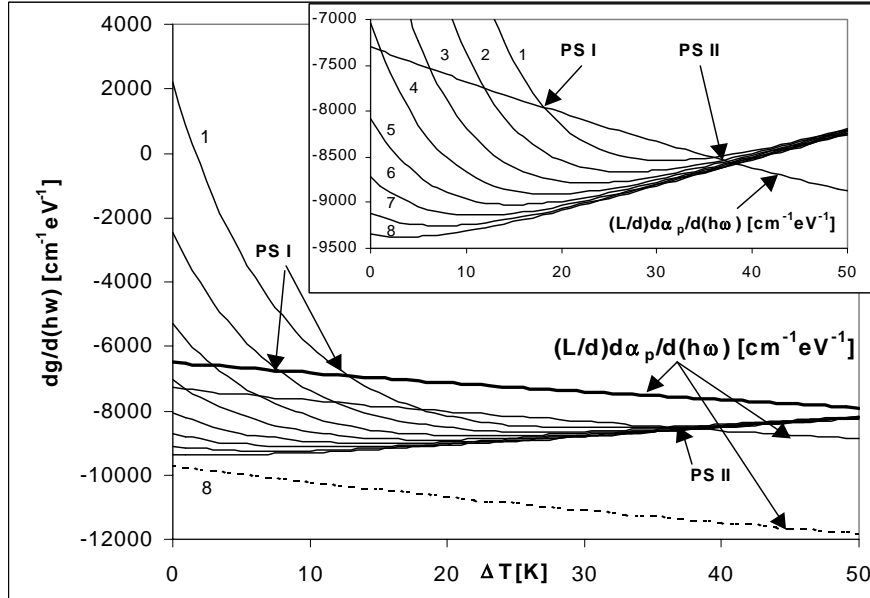


Figure 5.10: The dependence of the gain derivative with respect to the photon energy on ΔT , difference between the active region temperature at a certain current and the one at threshold (solid curves 1-8). For curve 1, $\hbar\omega_0$ is close to the gain maximum and $T_{\text{sub}}=300\text{K}$. Each of the curves 2-8 corresponds to a relative increase of the substrate temperature of 4.5 K. The dependence of the loss derivative on the active region temperature rise above threshold is shown by the nearly straight lines. The initial points of thick and thin solid lines are taken at $(\alpha_p/\alpha_{ol})g \approx 2000 \text{ cm}^{-1}$ and $T_{\text{sub}}=300\text{K}$ and 350K , correspondingly. The inset shows an enlargement [10].

c) The birefringence and the gain anisotropy induced by strain can explain some experimental results showing the strong dependence of PS on the external stress applied to the laser that are not explained by the latter gain-shift related models. To account for the effect of the anisotropic in-plane strain one should consider that it not only leads to birefringence via the elasto-optic effect but that it also results in a *different gain* for each of these modes. The effect of in-plane uniaxial strain can be illustrated by considering the Luttinger - Kohn Hamiltonian for the QW HH and LH bands and introduce the strain contribution according to the Bir-Pikus theory [19]. Valence band mixing takes place due to the existence of nondiagonal terms in the Hamiltonian [19].

Due to the anisotropy in the valence band energy dispersion relations, the gain will be different for different polarizations in the plane of the QW [20]. Because the maximum splitting is

along the [110] and [1-10] crystallographic directions, the gain anisotropy will also be maximum along these two directions. Due to the strain induced gain anisotropy, each linearly polarized state has its own gain curve on which it moves, as any relevant parameter is changed [12] (lattice and carrier temperature, carrier density, etc). In addition to the strain induced gain anisotropy, we have the gain difference due to the frequency splitting between the linearly polarized cavity modes which is also a result of the strain via the elasto-optic effect induced birefringence [12]. As the DC current is increased, the active region heats up and the gain will redshift faster than the cavity modes. Therefore, when working on the higher frequency side of the gain maximum, the carrier density should increase in order to keep the gain equal to the losses. To explain type II PS occurring on the higher frequency side of the gain maximum, two conditions should be met: 1) the linearly polarized mode with higher frequency has to show the larger gain (solid line in Figure 5.11 a) and 2) the two gain curves should move apart from each other with increasing current (Figure 5.11 b). In such a case the initial gain of the lower frequency mode is larger (Figure 5.11 a), but when the two gains move apart when the current is increased, they become equal (Figure 5.11 b) and, eventually, the higher frequency mode will have the larger gain (Figure 5.11 c). It should be mentioned that in this picture, type II PS can be preceded by type I PS around the gain maximum. Such double PS has been experimentally demonstrated [10]. If instead the condition 1) the lower frequency mode has the larger gain, PS would not happen on the higher frequency side of the gain maximum. If instead of condition 2), the two gain curves move closer to each other with increasing current, type I PS can still occur on the higher frequency side of the gain maximum [5].

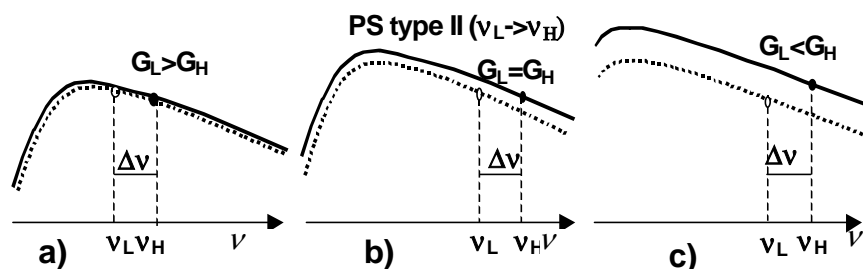


Figure 5.11: scheme of the gain spectrum when a separate gain curve for each linearly polarized eigenstate is considered. Type II PS occurs on the higher frequency side of the gain maxima as the current is increased from (a) to (c) [12].

In practice, one has to consider not only the material gain, but also the overlap of the optical field and the carrier density radial distributions, i.e. the modal gain. The modal gain can be changed due to change in the optical field pattern (by thermal lensing [5]) or the carrier distribution (by spatial hole burning [13]). Equalization of the modal gains for the two polarization modes with slightly different wavelengths can also occur in such way.

d) Polarization modes and stochastic resonance: a great deal of theoretical work has been performed on polarization fluctuations which are present in all lasers but prove to be exceptionally

strong in VCSELs. The reason for this is twofold. On the one hand, the spontaneous emission noise, which drives the polarization fluctuations, is relatively strong due to the limited size of the device. On the other hand, the deterministic forces, being the optical anisotropies in the device, are relatively small due to the nominal cylindrical symmetry of a VCSEL. The combination of strong stochastic noise and weak restoring forces creates relatively large polarization fluctuations.

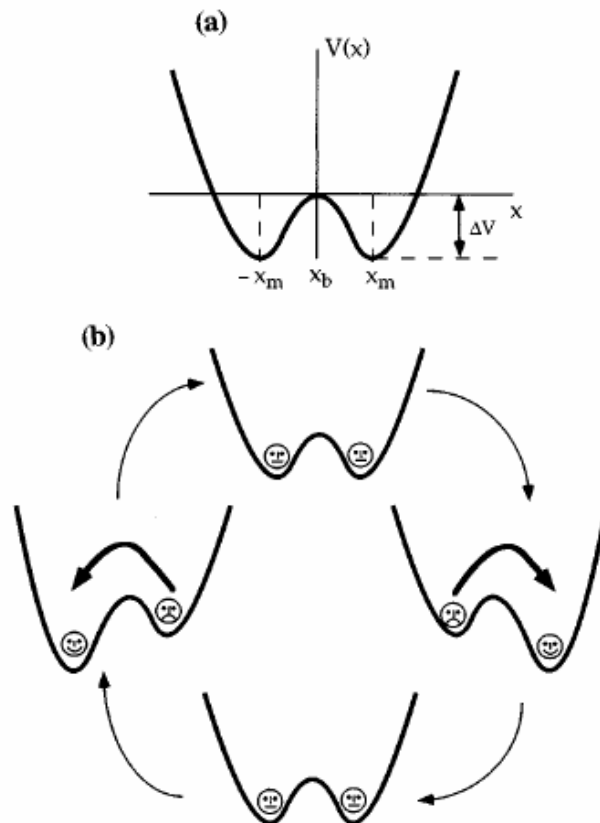


Figure 5.12: Stochastic resonance in a symmetric double well. (a) Sketch of the double-

well potential $V(x) = \frac{1}{4}bx^4 - \frac{1}{2}ax^2$. The minima are located at $\pm x_m$, where $\pm x_m = \left(\frac{a}{b}\right)^{\frac{1}{2}}$. These

are separated by a potential barrier with the height given by $\Delta V = \frac{a^2}{4b}$. The barrier top is

located at $x_b = 0$. In the presence of periodic driving, the double-well potential

$V(x, t) = V(x) - A_0 x \cos(\Omega t)$ is tilted back and forth, thereby raising and lowering successively the potential barriers of the right and the left well, respectively, in an antisymmetric manner.

This cyclic variation is shown in the cartoon above (b). A suitable dose of noise (i.e., when the period of the driving approximately equals twice the noise-induced escape time) will make the

“sad face” happy by allowing synchronized hopping to the globally stable state (strictly speaking, this holds true only in the statistical average).

It was demonstrated before that when a VCSEL is driven with a constant current in the vicinity of its polarization switching point, it makes random jumps between its two linear polarization states. This mode-hopping phenomenon has been intensively studied. It has been shown that, for a particular value of the pump current, the laser is bistable and the polarized intensity is characterized by noise-induced jumps between two levels, with a Kramers statistics [21]. With a suitable Langevin model of the local dynamics a correct description of the statistics of the jumps is given.

The term of stochastic resonance (SR) describes a particular behavior of the response of a bistable system when a weak coherent signal is superimposed to stochastic fluctuations as an input. One commonly expects that an increase of the noise level leads to a deterioration of the performance. In such systems, however, the noise can induce synchronized jumps between the two stable states, producing a strong output signal. Hence, the response of the bistable system shows a resonance-like behavior versus the input noise level, which is the main signature of SR. Many evidences of this kind of noise-induced ordering have been given in different fields, ranging from biology (neurophysiology – in the neuronal processes) and geology, to information theory and physics. Actually this idea was first introduced in 1981 by Benzi et al. [22,23] and by Nicolis and Nicolis [24] to explain the periodicity of the ice ages in the quaternary climate. There, the small periodic input is represented by the modulation of the earth's orbital eccentricity, while the fluctuations are due to the year-to-year variations of the solar activity.

The mechanism of stochastic resonance is simple to explain. Consider a heavily damped particle of mass m and viscous friction γ , moving in a symmetric double well potential $V(x)$. The particle is subject to fluctuational forces. The fluctuational forces cause transitions between the neighboring potential wells with a rate given by the famous Kramers rate, i.e.:

$$r_K = \frac{\omega_o \cdot \omega_b}{2 \cdot \pi \cdot \gamma} \cdot \exp\left(-\frac{\Delta V}{D}\right) \quad (5.1)$$

with $\omega_o^2 = V''(x_m)/m$ being the squared angular frequency of the potential in the potential minima at $\pm x_m$, and $\omega_b^2 = |V''(x_b)/m|$ the squared angular frequency at the top of the barrier, located at x_b ; ΔV is the height of the potential barrier separating the two minima. The noise strength $D=k_B T$ is related to the temperature T . If we apply a weak periodic forcing to the particle, the double well potential is tilted asymmetrically up and down, periodically raising and lowering the potential barrier. Although the periodic forcing is too weak to let the particle roll periodically from one potential well into the other one, noise-induced hopping between the potential wells can become synchronized with the weak periodic forcing. This statistical synchronization takes place when the average waiting time $T_K(D)=1/r_K$ between two noise-induced interwell transitions is comparable with half the period T_Ω of the periodic forcing. This yields the time-scale matching condition for stochastic resonance, i.e.:

$$2 T_K(D)=T_\Omega \quad (5.2)$$

In short, stochastic resonance in a symmetric double-well potential manifests itself by a synchronization of the activated hopping events between the potential minima with the weak periodic forcing. For a given period of the forcing, T_{Ω} , the time-scale matching condition can be fulfilled by tuning the noise level D_{max} to the value determined by the previous equation.

One can see that polarization switching is not abrupt, but rather extends over a certain switching region with respect to the pump current. The effect of mode-hopping between the two levels clearly appears while observing the histograms of the polarized intensity fluctuations: while a normal behavior is characterized by a Gaussian distribution, in the switching region the histogram has a distorted shape and exhibits two peaks corresponding to the above-mentioned levels (Figure 5.13). But it is important to notice that the total output intensity remains constant, which means that the fluctuations in the two polarizations are strongly anti-correlated.

Investigating the statistics of the residence times in the two levels involved in the dynamics of the system, one finds an exponential distribution of van't Hoff-Arrhenius type (Figure 5.14).

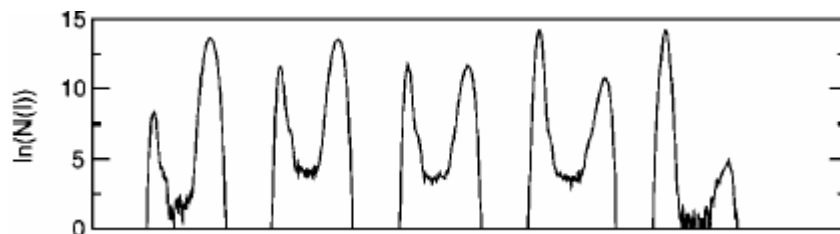


Figure 5.13: Histograms $N(I)$ of the polarized laser intensity $I(t)$ for different pump currents (increasing from left to right) across the investigated transition [21].

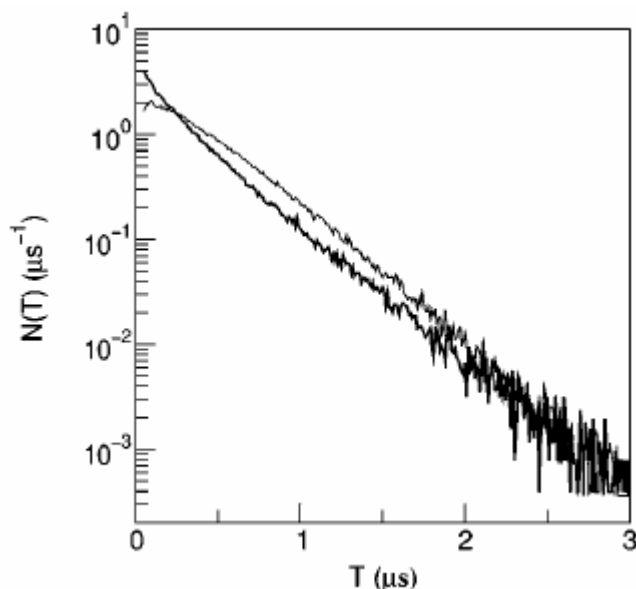


Figure 5.14: Normalized histograms $N(T)$ of the residence times T in the upper (thin line) and lower (thick line) state [21].

The observed behavior can be reproduced using a simple phenomenological model. A Markoffian process described with a Langevin model [25] which assumes that the temporal evolution of the intensity q in one polarization is determined by a quasi-potential $V(q)$ and a stochastic term, a Langevin noise source, $F(t)$:

$$\dot{q} = -\frac{\partial V(q)}{\partial q} + F(t) \quad (5.3)$$

One of the defining characteristics of the Langevin noise source, $F(t)$, is its completely random nature. Actually, the best analogy to $F(t)$ is a random number generator that generates a new number between $\pm\infty$ every interval Δt in the limit of $\Delta t \rightarrow 0$. Mathematically, this characteristic is described as a memoryless process which means that the value of $F(t)$ at time t has absolutely no correlation with any previous value $F(t-\tau)$.

In the switching region, $V(q)$ has a two-well shape, with the abscissa of the minima corresponding to the two intensity levels (upper and lower). Jumps between the two wells are driven by the Langevin term. In such a system, the probability distribution $P(q)$ is given in general by:

$$P(q) = P_0 \cdot \exp\left(-\frac{V(q)}{D}\right) \quad (5.4)$$

where P_0 is a normalization constant and D is the diffusion coefficient defined by:

$$\langle F(t')F(t'') \rangle = 2D \cdot \delta(t' - t'') \quad (5.5)$$

Increasing the pump current across the switching region, a transition from a situation where the polarized laser intensity is most of the time in the upper level to one with the intensity mostly in the lower level can be observed. The histograms of the intensity fluctuations change accordingly, namely, from a two-peak shape where the larger peak is on the right to one where it is on the left. In Figure 5.13 these histograms are reported on a semilogarithmic scale. According to Eq. (5.2), these probability distributions can be directly interpreted as quasipotentials by simply inverting the vertical axis. Following this interpretation, in the absence of noise-driven jumps the bistable region would correspond to the pump current interval where the quasipotentials display two wells, i.e. two local minima. Increasing the current, the system remains in the upper state while its level corresponds to a local minimum; then it jumps to the lower level and vice versa.

5.3 Designs for polarization stabilization and control in VCSELs

The applications of polarization switching in VCSELs for sensing and data communication are only starting to emerge. As the polarization of light gives an additional degree of freedom in information transport and routing, it is mandatory to be able to control the polarization behavior in VCSELs. In the previous section we exposed the different approaches to explain this phenomenon and in this section we will show how these concepts have been applied in practice. Polarization

stabilization means the effect of pinning the polarization into an *a priori* known direction and polarization control means that the polarization of the emitted light can be changed via an externally controllable signal or event. Besides the already mentioned method to stabilize the polarization of the emitted light via an in-plane strain applied to the device [12] we will present some other approaches: 1) polarization stabilization using a special design of intra-cavity contacted VCSELs based on an asymmetric contact layout [26]; 2) polarization stabilization by introduction of loss anisotropy using anisotropic mesa shapes; 3) polarization stabilization in structures grown on misoriented substrates; 4) polarization control exploiting the electro-optic birefringence.

5.3.1. Polarisation selection through asymmetric current injection

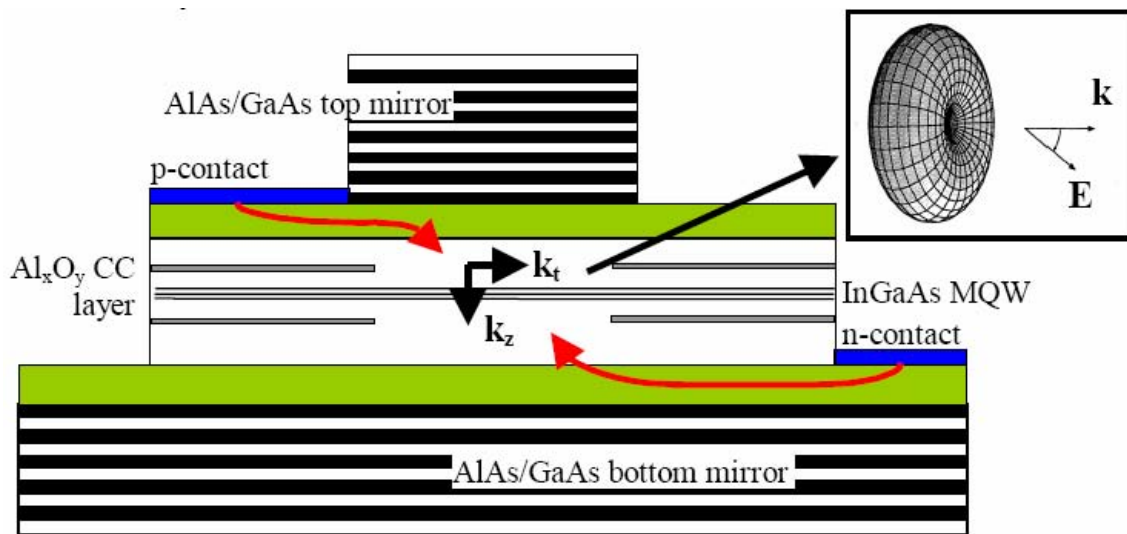


Figure 5.15: Asymmetric current injection results in $k_t \neq 0$. The inset shows the dependence of the transition probability on the orientation between the crystal momentum of the injected carriers (\mathbf{k}) and the electric field of the electromagnetic wave (\mathbf{E}) [26].

In order to explain the effect of the asymmetric current injection on the polarization of the emitted light, one has to look in the anisotropies introduced in the gain and loss. The asymmetric current injection results in an anisotropy in the gain g for the two orthogonally polarized modes. It induces a non-zero transverse component of the crystal momentum (k_t) of the injected carriers in the active layer. Because the active layer consists in compressively strained QWs ($\text{In}_{0.17}\text{Ga}_{0.83}\text{As}$ QWs), it is essentially the transition between the conduction and heavy hole band that will determine the laser output. The polarization dependence of this transition is given by [27]:

$$\text{Transition probability} \sim 1 - \left| \vec{k} \cdot \vec{E} \right|^2 \quad (5.6)$$

As shown in Figure 5.15, this electron-hole transition probability depends on the relative orientation between the crystal momentum of the injected carriers (unity vector \vec{k}) and the electric field of the emitted electromagnetic wave (unity vector \vec{E}) and will be maximal when the optical field

is polarized perpendicularly to the transverse component of the crystal momentum. If one defines g'' (g^\perp) as the gain of the mode polarized parallel (respectively perpendicular) to the current direction, that means that $g'' < g^\perp$.

Also, the asymmetric current injection determines a definite direction of the transverse component of the applied electric field in the plane of the contact layers. This results in a polarization dependence of the optical loss α , which can be used for polarization selection [28]. A first contribution to the polarization dependence of the loss is determined by the electroabsorption effect. The above mentioned experiment showed that $\alpha'' > \alpha^\perp$. Here α'' (α^\perp) is the loss of the VCSEL mode parallel (respectively perpendicular) to the current direction.

These two mechanisms (gain and electro-absorption) predict a polarization of the emitted light perpendicular to the current path.

5.3.2. Polarisation selection through anisotropic transverse geometries

Another technique for removing inherent polarization degeneracy and thereby selecting a specific polarization direction has been demonstrated by Choquette et al. [29]. VCSELs with various cavity shapes but equal cross-section area ($320 \mu\text{m}^2$) were fabricated, including circular ($20 \mu\text{m}$ outer diameter with $8 \mu\text{m}$ diameter aperture), rhombus (two adjacent equilateral triangles with $19 \mu\text{m}$ sides with an $8 \mu\text{m}$ diameter aperture), and dumbbell (two overlapping $12 \mu\text{m}$ diameter circles with center to center spacing of $10 \mu\text{m}$ and a $5 \mu\text{m}$ diameter aperture). The results show that circular VCSELs have competing orthogonal polarizations for fundamental mode lasing, but anisotropic cavity designs can select a single polarization state. With a rhombus-shaped cavity, fundamental mode lasing emission linearly polarized along one specified crystal axis is obtained up to twice the threshold current. A dumbbell cavity geometry is effective not only to promote one fundamental mode polarization state, but also to suppress lasing in the other state, thus maintaining a given polarization state. In this latter case, fundamental mode lasing emission linearly polarized along one specified crystal axis is maintained over the entire operation range of the device producing a maximum orthogonal polarization suppression ratio of 14 dB.

5.3.3. Polarisation selection by growth on misoriented substrates

Strong polarization selectivity was obtained for 780 nm vertical-cavity surface-emitting lasers by growing them on misoriented substrates [30]. All VCSELs grown on 2° off misoriented (001) substrate exhibit a high polarization suppression ratio over a few hundred. The main polarization is always along the [-110] direction over the entire operation range. To obtain the optical gain of a VCSEL below threshold with respect to two polarizations, the spectral linewidth of the spontaneous emission is measured with the increase of current. The subthreshold measurements yield more accuracy and immunity from the thermal effects. The spectral linewidth of the cavity mode is related to the modal gain g by:

$$g = -\alpha_{QW} = (\alpha_i + \alpha_m) - \Delta\lambda_{1/2} \cdot \left(\frac{2 \cdot \pi \cdot n}{\lambda^2} \right) \quad (5.7)$$

where n is the refractive index, α_i , α_m and α_{QW} are internal loss, mirror loss and the loss in QW. In the previous equation, the authors assume that $(\alpha_i + \alpha_m)$ is the same from both polarizations and the difference of linewidth comes from the change of α_{QW} . The cavity loss $(\alpha_i + \alpha_m)$ is obtained from the measurement of the slope efficiency and the theoretical mirror loss and is approximately 80 cm^{-1} . Experimentally, if one takes the difference between the two polarizations in the measured linewidth, only the contribution for $\Delta\alpha_{QW}$ will survive. The results of the subthreshold spectral linewidth measurement show that the modal gain/loss difference between two competing polarization modes in the VCSEL grown on the 2° off misoriented (001) GaAs substrate measures 3.0 cm^{-1} , which is larger than 0.5 cm^{-1} of the VCSLEs grown on the (001) substrate. This, together with the L-I curves, demonstrates the obvious polarization stabilization of the VCSELs grown on a misoriented substrate.

The physical origin of this experimental data is not clear. As these experiments were performed on 780 nm VCSELs, the calculations done for InGaAs lasers (most of the theoretical work performed up to now) do not apply because the AlGaAs system exhibits nearly no lattice mismatch and strain. Considering the optical transition matrix element for the structure grown on 2° off misoriented (001) GaAs substrate, this differs only by 0.017% which is orders of magnitude smaller to account for the previously mentioned experimental results. This large discrepancy shows that existing theoretical approaches cannot explain these experimental data and the possibility of other polarization selection mechanisms should be investigated.

5.3.4. External electrical field applied to the top DBR

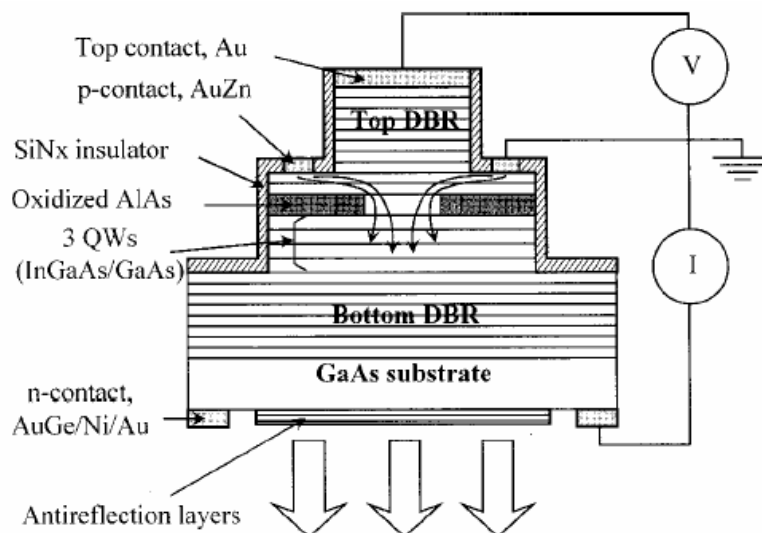


Figure 5. 16: Schematic of a three-contact VCSEL [31].

Several approaches have been investigated to provide the means to achieve polarization control. In order to use the electro-optic birefringence Park et al. [31] proposed a three-contact VCSEL design that allows applying an electric field along the [001] direction in the top distributed Bragg reflector. This makes the refractive index of GaAs and Al As anisotropic and the cavity resonances in the [110] and [1-10] directions are different. When an electric field E is applied along the [001] direction, the refractive indices along [110] and [1-10] directions $n_{[110]}$ and $n_{[1-10]}$ can be calculated from the following relation [32]:

$$\begin{aligned} n_{[110]} &= n_0 - \frac{n_0^3}{2} \cdot r \cdot E \\ n_{[1-10]} &= n_0 + \frac{n_0^3}{2} \cdot r \cdot E \end{aligned} \quad (5.8)$$

where n_0 is the refractive index in the absence of an electric field, and r is the electro-optic coefficient of GaAs or AlAs. When an electric field is applied, the cavity resonance of the polarized light along the [100] or [1-10] direction shifts to a shorter and longer wavelength, depending on the direction of the applied electric field. For a positive electric field, the cavity resonance of the [110] polarization mode (H mode in Figure 5.17) shows a blue shift, while that of the [1-10] polarization mode (V mode in Figure 5.17) shows a red shift. The cavity resonance difference between the two polarization modes linearly increases with increasing the electric field strength. For a negative electric field, the cavity resonances shift to the reverse direction. The reflectivity change of the top DBR by the applied electric field is very small at around the cavity resonance so that the loss change can be ignored for the selection of a dominant polarization mode. The authors expect that the electro-optic birefringence results in the gain difference between H and V modes due to their different cavity resonances, and this is the main factor in changing the polarization properties.

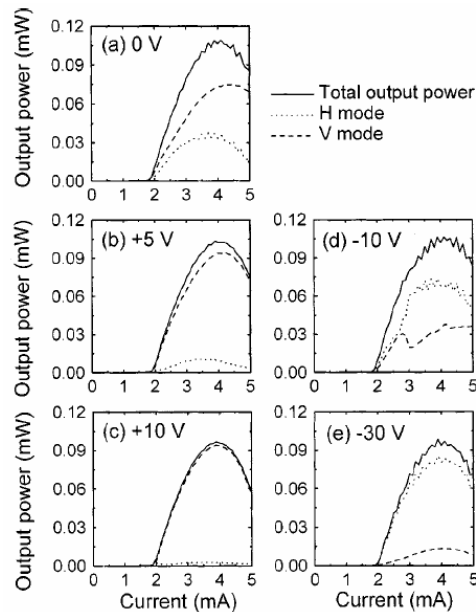


Figure 5.17: Polarization resolved light–current characteristics at various applied voltages [31].

In Figure 5.17 the authors demonstrate active control of the polarization properties of the emitted light. The output powers in the two modes are easily changed by the applied voltage variation. In the absence of the electric field, the power in the mode V is slightly larger than in the mode H. When the applied voltage is positive, the power in the mode H decreases while the power in the mode P increases. The mode H is completely suppressed for an applied voltage of 10 V. On the contrary, if the applied voltage is negative, the H mode becomes the dominant polarization mode. The field strength needed to change the polarization of the VCSELs ranges from 10^4 to 10^5 V for different devices. A slight decrease was observed in the total output power as the electric field increases. Since the gain curve is not changed during the application of the electric field, the thermal effect by the high electric is believed to be responsible for the decrease.

Therefore, this experimental data prove that the polarization of the VCSELs has been successfully controlled by applying the electric field on the top DBR and this polarization state can be actively controlled by varying the direction and the strength of the electric field.

5.4 Control of polarization switching in CC-VCSELs

In this work we propose to use the device described in Chapter 3 in polarization sensitive optical applications. We demonstrate that one can independently choose both the power of the output beam – through the current in the first cavity – and the polarization state—through the bias applied to the second cavity. Actually, this is the very first experimental proof of non-thermal, electrically induced polarization switching in coupled-cavities VCSELs.

As we showed in a previous chapter, the bias of the two cavities can be independently modified therefore achieving different domains of operation. The experimental data of polarization control are obtained in the following experimental conditions: the current injected in the top cavity is constant at 3 mA while the bias of bottom cavity is swept typically in the range -5 to +1 V. In these conditions, only the 927 nm mode lases with a higher threshold current around 1mA. We performed pulsed measurements for both cavities with 1 kHz frequency and 1% duty cycle, which corresponds to a period of 1 ms and a pulse-length of 10 μ s. Two pulse generators (Agilent 8114A 100V/2A Pulse Generator and Hameg HM8310 Programmable Function Generator) have been used for the two cavities, one of them (Agilent) triggering the other one (Hameg) in order to synchronize the electrical pulses for the two active regions. All measurements have been performed at room-temperature. An Edmund Optics polarizer was used in order to distinguish between the two orthogonal polarization states.

The maximum output power under these experimental conditions was about 15 μ W. While sweeping the bottom cavity voltage, a PS between two orthogonal linear polarization states of the laser emission is observed. Hereafter the two polarization states will be called 0 - and 90 -state and they are oriented respectively along the [110] and [1-10] crystalline axes. Figure 5.18 presents the total light

output and the output for one of the two polarization states (0°-state) as well as bistable operation with respect to the bottom cavity bias. The curve in Figure 5.18 is representative for around 30 out of 60–70 tested devices from the same manufacturing run, all of them showing dual lasing. The switch is very abrupt, the transition taking place within a 0.2 V interval. The device exhibits excellent polarization selectivity, the contrast ratio between the output powers of the two polarizations being around 1000 or higher. For positive bias to the bottom cavity the light output has the 90°-state as the dominant polarization state. The inset of Figure 5.18 shows a schematic of the device. The bistable region extends for 1 V and the output power is about 10 μW for 3 mA pump current.

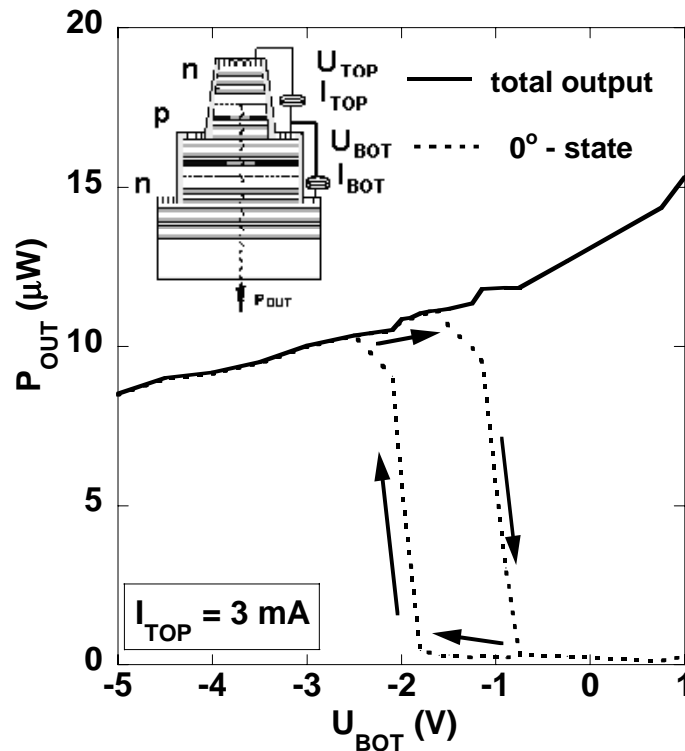


Figure 5.18: Polarization-switch curves and total output power of the device.

Similar results reporting polarization control in a CC-VCSEL structure have been reported by Choquette et al. [33]

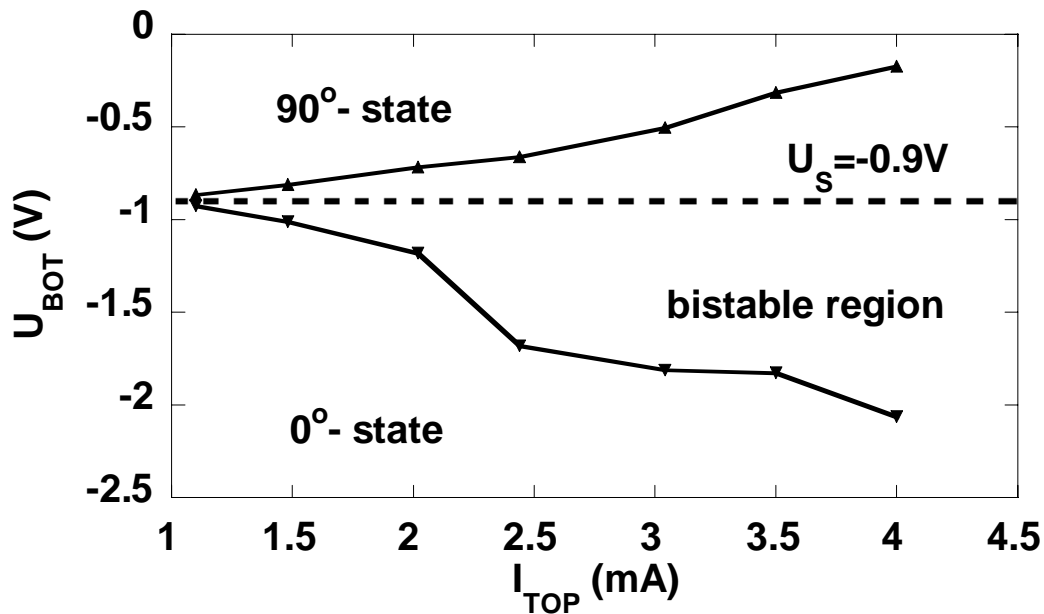


Figure 5.19: Width of the bistable region versus I_{TOP} .

Figure 5.19 shows the evolution of the bistable behavior with the pump current. At threshold (1 mA), PS occurs with no bistability at a reverse switch U_S . At exactly U_S , the polarization state is not stable and a stochastic mode hopping is observed between the two polarization states. When the pump current is further increased, we observe the appearance and development of a bistable region centered on U_S . The width of this bistable control voltage reaches 2 V at four times the threshold current value. The exact value of U_S varies for different tested devices between 0 and 1.3 V.

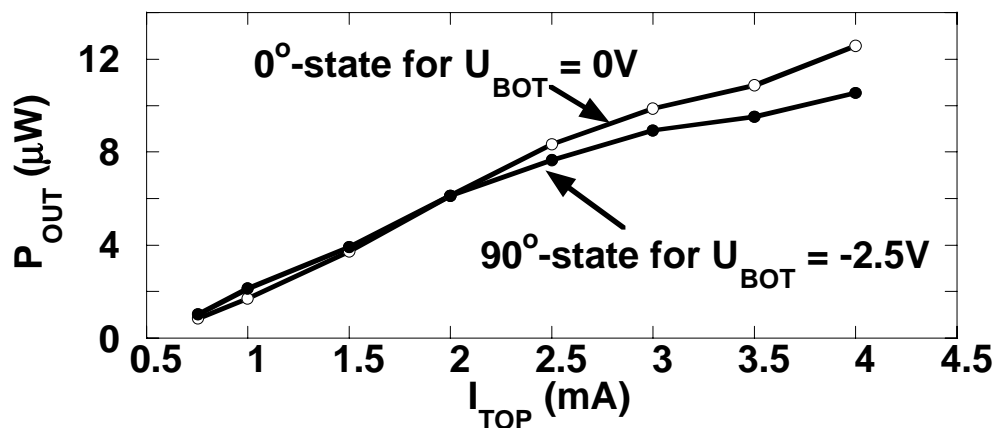


Figure 5.20: Polarization resolved L-I curves.

This method of changing the polarization state using a third electrical contact offers an additional degree of freedom compared to the classic current-driven PS since the output power and the polarization state can be independently modified. In the L-I curves presented in Figure 5.20 we demonstrate that the output power for each of the two states increases monotonically with the I_{TOP} current with nearly equal efficiencies.

Due to this novel three-contact design, the output power and the polarization state can be independently modified. Figure 5.21 and Figure 5.22 show the measured time response of the PS. Figure 5.21 illustrates the triggered-mode operation, where the polarization is directly controlled by U_{BOT} . Figure 5.22 illustrates the bistable-mode operation where the polarization is switched between the 0° - and 90° - states by short pulses, which drive the device outside bistable control voltage. The oscillations in the measured laser response are due to parasitic resonances in the whole circuit. In both cases, the top cavity is direct-biased with a 400 ns pulse for a 1ms-long cycle. In the triggered mode, both the baseline and the pulse of the reverse bias in the bottom cavity are outside the hysteresis region of the device. The 200 ns pulse in the bottom cavity is sent within the pulse in the top cavity. The optical output switches its polarization state to the 0° -state only during this control signal, returning to the original state (90° -state) after the pulse. In the bistable mode, the baseline of the reverse bias of the bottom cavity is placed at U_S , inside the hysteresis region, and the amplitude of the control pulse crosses this region. The optical response switches its polarization state after a control signal as short as 9 ns. The measured switch time of the PS is below 2 ns, limited by our experimental setup. It indicates that the switching is intrinsically fast and not driven by thermal effects. The rise-time of the onset of one polarization state was measured with a fast detector – Silicon Avalanche Photodiode Module Hamamatsu C5658 with a cut-off frequency of 1 GHz. The laser beam was focused using a lens on the active area of 0.5 mm of the detector.

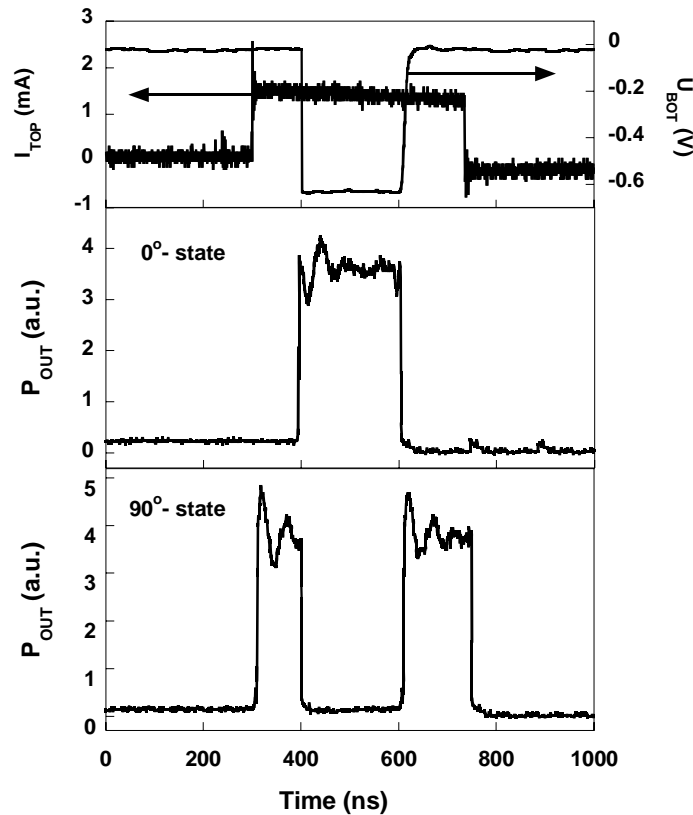


Figure 5.21: Triggered-mode: Polarization resolved output power in response to a stepwise variation of U_{BOT} .

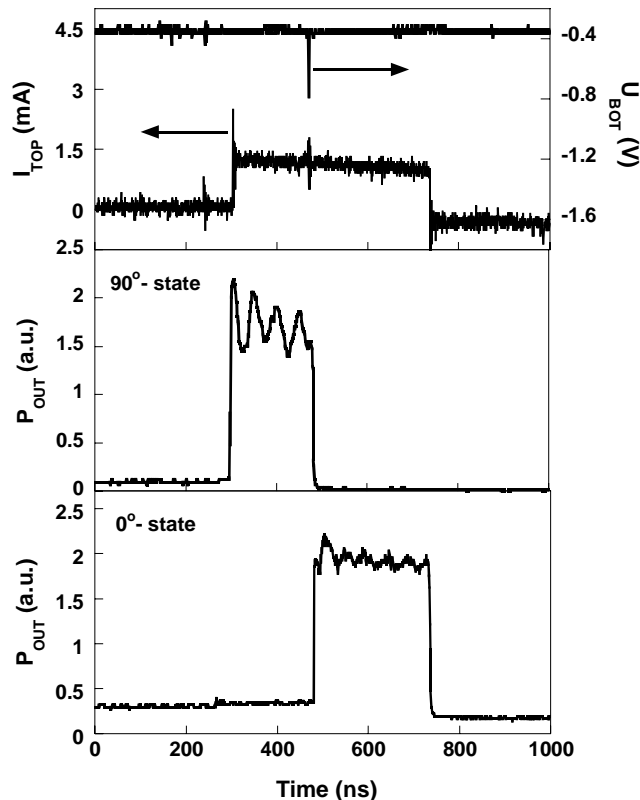


Figure 5.22: Bistable-mode: Polarization resolved output power in response to a 20-ns pulse of U_{BOT} .

Willemsen et al [34] discuss polarization switching in a VCSELs and show that the polarization dynamics is determined by dispersive anisotropies and absorptive anisotropies which create a difference in frequency and gain between the two polarizations. Both anisotropies consist of a linear part which quantifies how much the cylindrical symmetry of the cavity is broken, and a non-linear part which corresponds to a polarization dependent saturation of the gain medium. They found that the polarization switch takes on average a few nanoseconds which is in agreement with the rise time of 2 ns found for our CC-VCSEL devices.

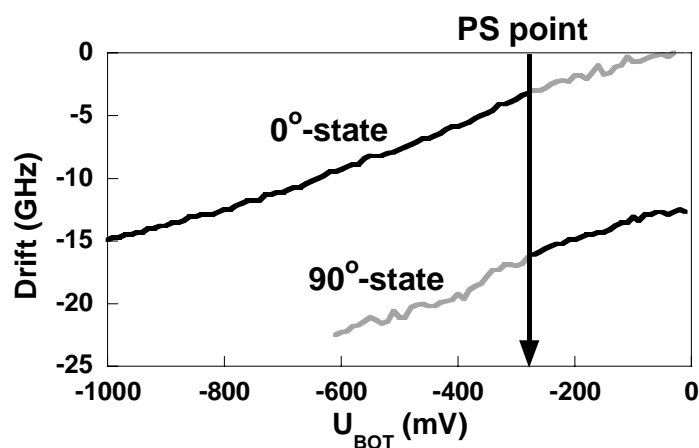


Figure 5.23: Frequency shift of the two polarization modes as a function of the U_{BOT} (and with $I_{TOP}=1.2\text{mA}$). Black (grey) lines correspond to lasing (nonlasing) mode.

We have investigated a few mechanisms that might be responsible for the polarization switching observed in our CC-VCSEL devices. One possible physical mechanism to explain the

observed polarization switch is the (linear) electrooptic birefringence induced by the reverse bias, as was reported by other groups [28,31]. In this case, the frequency splitting induced by the electric field along changes its sign and, consequently, leads to a change of the gain-preferred mode and, hence, to polarization switching. To test whether this effect is responsible for polarization switching in our coupled-cavity VCSELs, we have measured the frequency shift of both modes as a function of the reverse bias voltage with a high-resolution spectrum analyzer (Burleigh) – see Figure 5.23). The measurement was performed very close to threshold. Therefore, bistable behavior is not observable (see Figure 5.19). In Figure 5.23, it can be seen that both modes red shift with increasing magnitude of the reverse bias voltage, but that their frequency difference essentially remains constant at about 13GHz which is equivalent to a wavelength splitting of about 0.4 \AA . As the measured electro-optic birefringence does not change with voltage, this mechanism cannot explain the occurrence of polarization switching in our VCSELs. So the physics beyond this polarization switching is qualitatively different as that in the paper of Park et al.

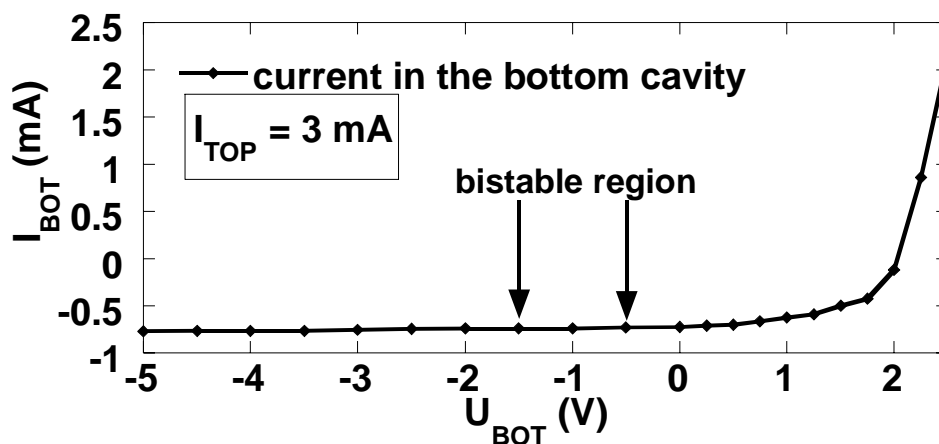


Figure 5.24: I-V curve of the bottom cavity.

The bottom cavity acts as an integrated photodetector for the output power. One can notice in Figure 5.24 that the photocurrent in the bottom cavity remains constant within the experimental precision when the PS occurs indicating that there is no significant change in the absorption in the bottom QWs. However, it does not exclude that interplay between the electric field modified absorption (below % range) in the bottom cavity (through the quantum confined Stark effect) and the optical gain in the top cavity in the presence of two polarization modes with slightly different wavelengths could be a possible reason for PS.

Therefore, a field enhanced electro-absorption change in the QWs could, in principle, lead to an explanation of the observed PS. This effect is known in literature as the Quantum Confined Stark Effect (QCSE). The quantum confined Stark effect consists of two components: one is the red-shift of the absorption band-edge with the applied electrical field and the second is the shift of the excitonic peaks in the absorption spectrum and their evolution (red-shift and broadening) with the applied electrical field. Many groups have performed detailed experimental measurements of the absorption

near the band-edge as electric fields are applied. Figure 5.25 [35] shows such measurements and one can notice the shift and broadening of the absorption edge with the applied bias. As a result, large field effects are possible over a very narrow wavelength range. Qualitatively, this could explain the polarization switch as in our case the wavelength splitting between the two modes is very small.

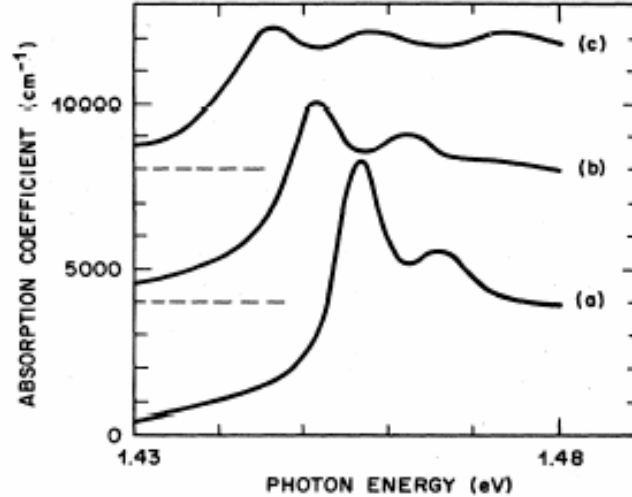


Figure 5.25: Absorption spectra at various electrical fields: (a) $\approx 1 \cdot 10^4$ V/cm; (b) $\approx 4.7 \cdot 10^4$ V/cm; (c) $\approx 7.3 \cdot 10^4$ V/cm [35].

In order to investigate if the QCSE is responsible for the PS in the CC-VCSEL structures, in Appendix B a detailed study of this effect is presented. This is a part of an on-going work which aims to express the QW absorption as a function of the applied electrical field. The total absorption consists of the interband optical contribution and the contribution of the exciton. This absorption coefficient is to be inserted in a system of rate-equations written for the two polarization modes.

At this stage of this work, we have calculated the part of the QCSE that consists in the dependency on the reverse applied electrical field of the interband optical contribution to the absorption coefficient, without considering the excitonic effect. The corresponding result of these calculations is presented in Appendix B, Figure B.1. In order to make our approach consistent with the discussion in the previous Chapter 4, we approximate the so calculated absorption in the InGaAs QWs using expressions like equations (4.17)-(4.20). This approximation is also presented in Appendix B for an $\text{In}_{0.2}\text{Ga}_{0.8}\text{As}$ QW with a thickness of 11 nm and helps us to implement in a straightforward way the reverse bias conditions in the rate equation model. Figure 5.26 presents qualitatively a consequence of the QCSE in the coupled-cavity VCSEL structure, i.e. an increase in the lasing threshold current in the top cavity in parallel with a decrease of the output power for higher reverse electrical fields.

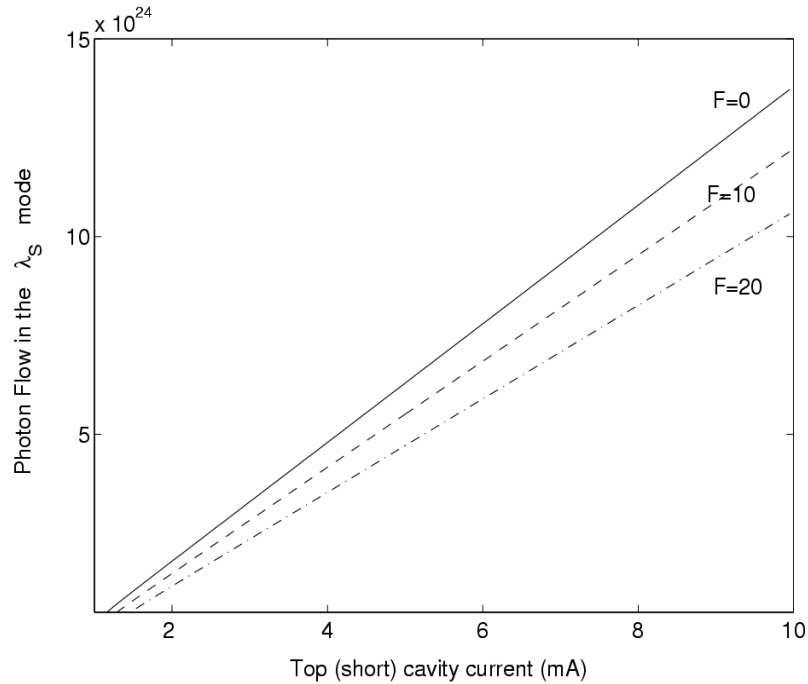


Figure 5.26: Photon Flow for the short-wavelength mode as a function of the top (short) cavity injection current and for different reverse bias in the bottom (long) cavity: $F=0$, $F=10$ and $F=20$ kV/cm and for $I_2=0$ mA.

5.5 Conclusions

In this Chapter we demonstrate active control of the polarization state of the coupled-cavity VCSEL by the voltage applied to the bottom-passive cavity while injecting current in the top-lasing cavity. The polarization switch occurs with a high contrast ratio and exhibits hysteresis.

We show that the device operates in two different regimes: 1) direct control of the polarization state by a command voltage outside the hysteresis; 2) bistable-mode operation when the polarization switching is controlled with short pulses. Of special interest is the fact that the electro-optical effect has been experimentally ruled out as one possible mechanism for electrical-field-induced polarization switching in coupled-cavity VCSELs. The quantum confined Stark effect in the QWs of the bottom cavity may be the reason for the observed reverse-bias polarization switching. A detailed study of this effect, applied to the actual CC-VCSEL structures, is intended to clarify its influence on the polarization switching in these VCSELs is in progress.

Bibliography CHAPTER 5

-
- [1] Chang-Hasnain, C.J., Harbison, J.P., Hasnain, G., Von Lehmen, A.C., Florez, L.T. and Stoffel, N.G., *IEEE J. Quant. Electr.* **27**, 1402-1408 (1991).

- [2] Jansen van Doornen, A.K., van Exter, M.P., and J.P.Woerdman, *Appl. Phys. Lett.* **69**, 1041-1043 (1996).
- [3] van Exter, M.P., Jansen van Doorn, A.K. and Woerdman, J.P., *Phys. Rev. A.*, **56**, 845-583 (1997).
- [4] Choquette, K.D., Richie D.A., and Leibenguth, R.E., *Appl. Phys. Letters* **64**, 2062-2064 (1994).
- [5] Panajotov, K., Ryvkin, B., Danckaert, J., Peeters, M., Thienpont, H., and Veretennicoff I., *IEEE Phot. Techn. Lett.* **10**, 6-8 (1998).
- [6] Martin-Regalado, J., Chilla, J.L.A., Rocca, J.J and Brusenbach, P., *Appl. Phys. Lett.* **70**, 3350-3352 (1997).
- [7] Choquette, K.D., Lear, K.L., Schneider, Jr., and Geib, K.M., *Electron. Lett.* **30**, 2043-2044 (1994).
- [8] Verschaffelt, G., Albert, J., Peeters, M., Panajotov, K., Danckaert, J., Veretennicoff, I., Thienpont, H., Monti di Sopra, F., Eitel, S., Hoevel, R., Moser, M., Zappe, H.P., and Gulden, K., "Polarization switching and modulation dynamics in gain and index-guided VCSELs" in *Vertical-Cavity surface-Emitting Lasers IV*, edited by Choquette, K. and Lei, C., Proceedings of SPIE 3946, SPIE, Washington, 2000, pp.246-256.
- [9] Ohtsu, M., Teramachi, Y., Otsuka, Y., and Osaki, A., *IEEE J. Quant. Electr.* **22**, 535-543 (1986).
- [10] Ryvkin, B., Panajotov, K., Georgievski, A., Danckaert, J., Peeters, M., Verschaffelt, G., Thienpont, H., and Veretennicoff, I., *Journ. Opt. Soc. Am. B*, **16**, 2106-2113, (1999).
- [11] Verschaffelt, G., *Vertical-Cavity Surface-Emitting Lasers for parallel optical Data communication: polarization switching components and intra-MCM interconnects*, PhD Thesis, Vrije Universiteit Brussels, Brussels, 2000.
- [12] Panajotov, K., Nagler, B., Verschaffelt, G., Georgievski, A., Thienpont, H., Danckaert, J., and Veretennicoff, I., *Appl. Phys. Letters* **77**, 1590-1592 (2000).
- [13] Valle, A., Pesquera L., and Shore, K.S., *IEEE Photon. Technol. Lett.* **9**, 557-559 (1997).
- [14] San Miguel, M., Feng, O., and Moloney, J.M., *Phys.Rev.* **A52**, 1728-1739 (1996).
- [15] Martin-Regalado, J., San Miguel, M., Abraham, N.B., and Prati, F., *Opt.Lett.* **21**, 351-353 (1996).
- [16] Martin-Regalado, Balle, S., J., San Miguel, Valle, A., Pesquera, L., *Quantum Semiclass. Opt.* **9**, 713-736 (1997).
- [17] Balle, S., Tolkachova, E., San Miguel, M., Tredicce, J.R., Martin-Regalado J., and Gahl, A., *Opt.Lett.*, **24**, 1121-1123, (1999).
- [18] B.Ryvkin and A. Georgievskii, *Semiconductors* **33**, 813-819 (1999).
- [19] Coldren, L.A., Corzine, S.W., *Diode Lasers and Photonic Integrated Circuits*, J.Wiley & Sons, 1995, pp.488-536.
- [20] Burak, D., Moloney, J.V., and Binder, R., *Phys.Rev. A*, **61**, 053809, (2000).
- [21] S. Barbay, G. Giacomelli, and F. Marin, "Stochastic resonance in vertical cavity surface emitting lasers", *Phys. Rev. E*, **61**, pp. 157-166 (2000).
- [22] R. Benzi, A. Sutera, and A. Vulpiani, *J. Phys. A* **14**, 453 (1981).
- [23] R. Benzi, G. Parisi, A. Sutera, and A. Vulpiani, *Tellus* **34**, 10 (1982).
- [24] C. Nicolis and G. Nicolis, *Tellus* **33**, 225 (1981).
- [25] G. Giacomelli and F. Marin, *Quantum Semiclassic. Opt.* **10**, 469 (1998).
- [26] G. Verschaffelt, W. van der Vleuten, M. Creusen, E. Smalbrugge, T. G. van de Roer, F. Karouta, R. C. Strijbos, J. Danckaert, I. Veretennicoff, B. Ryvkin, H. Thienpont, and G. A. Acket, "Polarization Stabilization in Vertical-Cavity Surface-Emitting Lasers Through Asymmetric Current Injection", *IEEE Phot. Techn. Lett.*, **12**, pp. 945-947 (2000).

- [27] S.W. Corzine, R.-H. Yan, and L. A. Coldren, "Optical gain in III-V bulk and quantum well semiconductors," in *QuantumWell Lasers*, P. S. Zory, Ed. Boston, MA: Academic, 1993, ch. 1.
- [28] B. Ryvkin, K. Panajatov, J. Danckaert, H. Thienpont, and I. Veretennicoff, "Intracavity electroabsorptive and electrorefractive control of the polarization in VCSEL's," in *Proc. 1998 Symp. IEEE/LEOS Benelux Chapter*, 1998, pp. 181-184.
- [29] K.D. Choquette and R.E. Leibenguth, "Control of Vertical-Cavity Laser Polarization with Anisotropic Transverse Geometries", *IEEE Photon. Tech. Letters*, **6**, pp. 40-42 (1994).
- [30] Y.-G. Ju, Y.-H. Lee, H.-K. Shin, and I. Kim, "Strong polarization selectivity in 780-nm vertical-cavity surface-emitting lasers grown on misoriented substrates", *Appl. Phys. Lett.*, **71**, pp. 741-743 (1997).
- [31] M.S. Park, B.T. Ahn, B.-S. Yoo, H.Y. Chu, H.-H. Park, and C.J. Chang-Hasnain, "Polarisation control of vertical-cavity surface-emitting lasers by electro-optic birefringence", *Appl. Phys. Lett.*, **76**, pp. 813-815 (2000).
- [32] A. Yariv, *Optical Electronics*, 4th ed. (Sanders College, Philadelphia, 1991), Chap. 9.
- [33] D. M. Grasso and K. D. Choquette, "Polarization switching in composite-resonator vertical-cavity lasers", *Appl. Phys. Lett.*, **83**, pp. 5148-5150, 2003.
- [34] M.B. Willemsen, M.P. van Exter, and J.P. Woerdman, *Phys. Rev. Lett.*, **84**, pp. 4337 (2000).
- [35] D.A.B. Miller, D.S. Chemla, T.C. Damen, A.G. Gossard, W. Wiegmann, T.H. Wood, C.A. Burrus, "Electric field dependence of optical absorption near the band gap of quantum well structures", *Phys. Rev. B*, **32**, pp. 1043-1060 (1985).

Chapter 6

Conclusions

This thesis is concerned with the study of coupled-cavity VCSEL structures. We first introduce in Chapter 3 the CC-VCSEL strictly from the optical point of view and we explain the operation of the CC-VCSEL in the frame of the lumped-mirror model. This model assumes a very simplified structure taking into account the optical parameters of the structure: three hard-mirrors, i.e. two end-mirrors and the middle mirror assuring the optical coupling between the cavities, and the lengths of the cavities, considering a detuning between them. Starting from the time dependent expressions for the field in the cavities and imposing the boundary conditions for the end-mirrors as well as the continuity conditions for the coupling mirror, one obtains a solution that describes the main peculiarities of the CC-VCSEL. The lumped-mirror model provides a solution for the two resonant modes of the CC-VCSEL structure as well as the splitting between them. This is expressed as a function of the structural parameters of the device: the detuning and the optical coupling strength between the cavities. The detuning is given by the lengths of the cavities and the optical coupling strength is determined by the reflectivity of the coupling mirror. The mode-spacing becomes smaller as the detuning is decreased. Another useful parameters introduced by the lumped mirror model are the confinement factors that describe the localization of the each mode in each cavity, respectively. These confinement factors are also presented as a function of the detuning between the cavities and the strength of the optical coupling. As the detuning between the cavities is increased, the short wavelength mode becomes more localized in the short cavity, while the long wavelength mode becomes more localized in the long cavity. Thus, the lumped-mirror model provides a useful design tool for the CC-VCSELs. One can choose the desired wavelengths of the resonant modes in the structure and then design it with the corresponding cavity detuning and reflectivity of the coupling mirror. The last section of Chapter 3 presents graphs with the calculated results of the light intensity inside the asymmetric CC-VCSEL structures and the corresponding splitting between the modes. The results provided by the lumped-mirror model are in very good agreement with the results given by the well-established transfer matrix method. The development of the lumped-mirror model together with

the results provided by the model were submitted for publication in IEEE Journal of Lightwave Technology.

Chapter 4 completes the previous discussion in Chapter 3 with the electrical characteristics of the CC-VCSEL structure. In addition to the optical characteristics of the device, we add the electrical injection. The rate-equation model presented in Chapter 2 for a classical laser is extended to the coupled-cavity device. We show that the three contacts design of the CC-VCSEL introduces an additional degree of freedom as one can independently control the two modes through the injection currents. The rate-equation model yields four equations, two for the number of carriers and two for the number of photons. These equations are solved under steady state conditions. The two rate-equations for photons become the threshold equations for each mode, respectively. These four equations are solved using a logarithmic parameterization of the dependence gain – carrier density. This model allows the identification of the different operating regimes of the device. We introduce the notion of the “double-threshold”, i.e. the point characterized by the couple of the injection currents necessary to reach the threshold for the two resonant modes of the structure, simultaneously. One can identify four different operating regimes of the device: the region where neither of the modes is lasing, the region where only the short wavelength mode is lasing, the region where only the long wavelength mode is lasing, and, the peculiarity of this device, a region where both modes are lasing simultaneously. It is this region that has an analogous with classical laser, because only in this operating regime the carrier densities in both cavities are clamped at values that correspond to the double-threshold point, the threshold equations for both modes being satisfied simultaneously. The results obtained with the rate-equation model are in good agreement with the experimental results on such a device. The model and the overlap between the theory and the experimental data are presented in a paper accepted for publication in IEEE Journal of Quantum Electronics.

Chapter 5 deals with the polarization aspects in VCSELs in general and in CC-VCSELs in particular. We present the previous work focused on the polarization behavior of VCSELs, experimental results and different theoretical approaches to explain polarization instabilities, polarization switching, polarization control and stabilization. We demonstrate the possibility to use the CC-VCSEL device in polarization sensitive optical applications. We show that one can independently choose both the power of the output beam – through the current in the first cavity – and the polarization state – through the bias applied to the second cavity. Actually, this is the very first experimental proof of non-thermal, electrically induced polarization switching in coupled-cavities VCSELs, reported in IEEE Photonics Technology Letters. The experimental data shows a polarization switching of the light emitted in the short wavelength mode. The switching takes place through a region of bistability, at a constant injection current in the short cavity, while sweeping the reverse bias voltage applied to the bottom cavity. We show that the bistable region can be used in order to operate the device in two modes: the triggered mode, i.e. the mode where the polarization state of the device changes during a control signal pulse, returning to the original state after the pulse, and the bistable

mode, i.e. the mode where the polarization state is changed after the control pulse, but it does not return to the original state. The switching time was measured to be as short as 2ns, limited by the experimental setup, which proves that that the switching is intrinsically fast and not driven by thermal effects.

Different mechanisms that might be responsible for the polarization switching have been investigated. One of them is the (linear) electro-optic birefringence induced by the applied reverse bias as similar results had already been published by other groups. But we ruled out this explanation in our case because the frequency splitting between the two polarization modes should cross each other with the increase of the reverse bias, i.e. the increase of the applied electric field, while in our case this difference remains constant during the switch.

An interesting intrinsic characteristic of the CC-VCSEL is demonstrated in Chapter 5 in a special bias regime. If one cavity (top) is forward biased, the bottom cavity acts as a built-in photodetector for the radiation emitted in the other cavity. The absorption in the bottom cavity depends on the applied reverse bias and influences the optical gain in the top cavity in the presence of the two optical modes. This drives us to investigate the quantum confined Stark effect in the QWs of the bottom cavity as a possible reason for the polarization switch. We implement the classical approach developed by Miller et al., which although approximate gives a very good physical insight in the mechanism of electro-absorption. We consider variationally the effect of electrical field in a quantum well assuming infinitely deep QW with an effective width matched to give the proper confining energy levels. We show that we can implement in a straightforward way the reverse bias condition into the rate equation model and we demonstrate the effect of the applied reverse bias on the output characteristic of the light emitted from the top cavity.

Briefly, a vertical-cavity surface-emitting laser of a special design, i.e. with two vertical cavities optically coupled and independently electrically biased, has been investigated. A detailed characterization of the output light has been performed for different bias regimes and a rate-equation model has been developed to explain the experimental data. One can see a very good agreement between the theory and the experiment. The model is a powerful toolbox in the design and characterization of different operating regimes of the coupled-cavity VCSEL. The polarization characteristics of the light emitted from one cavity (direct biased) are also presented and the effect of the reverse bias applied to the other cavity is analyzed. The quantum confined Stark effect is investigated and through this effect, the result of the reverse bias applied to one cavity on the output characteristics of the direct bias cavity.

Appendix A

Derivation of the rate-equations

This model studies the rate equations for carriers and photons in steady-state. So we start the derivation separately for carriers and photons, setting the time derivatives in equations (4.1)-(4.4) to zero. We start with equations (4.1) and (4.2) under steady-state conditions:

$$\frac{\eta_1 I_1}{q} = \left(\frac{2\xi_1^S v_g^S}{V_{ph,1}} N_{ph,1}^S g_1^S + \frac{2\xi_1^L v_g^L}{V_{ph,1}} N_{ph,1}^L g_1^L \right) \cdot V_1 + (R_{sp,1} + R_{nr,1}) \cdot V_1 \quad (\text{A.1})$$

$$\frac{\eta_2 I_2}{q} = \left(\frac{2\xi_2^S v_g^S}{V_{ph,2}} N_{ph,2}^S g_2^S + \frac{2\xi_2^L v_g^L}{V_{ph,2}} N_{ph,2}^L g_2^L \right) \cdot V_2 + (R_{sp,2} + R_{nr,2}) \cdot V_2 \quad (\text{A.2})$$

The fraction of the number of photons in the mode “S” or “L” existing in the cavity i is given by the confinement factors $\Gamma_i^{S,L}$ introduced by the lumped mirror model (presented in Chapter 3) or calculated by the transfer matrix method. These coefficients satisfy a normalization condition for each mode respectively:

$$\begin{aligned} \Gamma_1^S + \Gamma_2^S &= 1 \\ \Gamma_1^L + \Gamma_2^L &= 1 \end{aligned} \quad (\text{A.3})$$

and by design:

$$\Gamma_i^S = \Gamma_j^L \quad \text{for } i \neq j \quad (\text{A.4})$$

In order to visualize better this confinement coefficient, we show in Figure A.1 a schematic of the field distribution of the two modes inside the coupled-cavity VCSEL, reproduced from Ref. [1].

So the confinement of the short mode in the cavity 1 (top) and respectively of the long mode in the cavity 2 (bottom) are described by a single independent confinement coefficient. We introduce the four coefficients explicitly in equations (A.1) and (A.2):

$$\frac{\eta_1 I_1}{q} = \left(\frac{2\xi_1^S v_g^S}{V_{ph,1}} \Gamma_1^S N_{ph}^S g_1^S + \frac{2\xi_1^L v_g^L}{V_{ph,1}} \Gamma_1^L N_{ph}^L g_1^L \right) \cdot V_1 + (R_{sp,1} + R_{nr,1}) \cdot V_1 \quad (\text{A.5})$$

$$\frac{\eta_2 I_2}{q} = \left(\frac{2\xi_2^S v_g^S}{V_{ph,2}} \Gamma_2^S N_{ph}^S g_2^S + \frac{2\xi_2^L v_g^L}{V_{ph,2}} \Gamma_2^L N_{ph}^L g_2^L \right) \cdot V_2 + (R_{sp,2} + R_{nr,2}) \cdot V_2 \quad (\text{A.6})$$

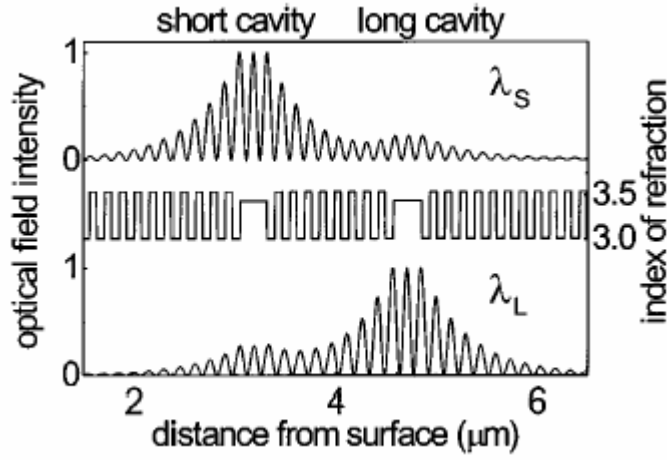


Figure A.1: Schematic of the field distribution for the “S” and “L” modes inside the CC-VCSEL [1].

The spontaneous emission rate together with the non-radiative recombination rate in cavity i are proportional to the total carrier density in cavity $i - \frac{N_i}{V_i}$, the proportionality factor being the carrier lifetime τ_e assumed to be the same in both cavities:

$$R_{sp,i} + R_{nr,i} = \frac{N_i}{V_i \tau_e} \quad (\text{A.7})$$

valid for $i = 1, 2$

The two rate equations for carriers become:

$$\frac{\eta_1 I_1}{q} = \left(\frac{2\xi_1^S v_g^S}{V_{ph,1}} \Gamma_1^S N_{ph}^S g_1^S + \frac{2\xi_1^L v_g^L}{V_{ph,1}} \Gamma_1^L N_{ph}^L g_1^L \right) \cdot V_1 + \frac{N_1}{\tau_e} \quad (\text{A.8})$$

$$\frac{\eta_2 I_2}{q} = \left(\frac{2\xi_2^S v_g^S}{V_{ph,2}} \Gamma_2^S N_{ph}^S g_2^S + \frac{2\xi_2^L v_g^L}{V_{ph,2}} \Gamma_2^L N_{ph}^L g_2^L \right) \cdot V_2 + \frac{N_2}{\tau_e} \quad (\text{A.9})$$

We explicitly write the volume of the active region i : $V_i = S_i l_i$, where S_i is the section of the device and l_i is the width of the active region; $l_i = p_i e$, with n_i – the number of QWs in the cavity i and e – the width of one QW. The cross-section area of the device is assumed constant, i.e. $S_1 = S_2 = S$. The volume of the optical mode in cavity i is given by $V_{ph,i} = S \cdot L_i$, but the effective cavity lengths $L_1 = L_2 = L$ may be considered equal for the two cavities taken into account the relatively small detuning – typically a few percent – as well as the penetration depths in the mirrors. Equations (A.8-9) become:

$$\frac{\eta_1 I_1}{q} = 2\xi_1^S v_g^S \cdot \Gamma_1^S \cdot \frac{l_1}{L} N_{ph}^S \cdot g_1^S + 2\xi_1^L v_g^L \cdot \Gamma_1^L \cdot \frac{l_1}{L} N_{ph}^L \cdot g_1^L + \frac{N_1}{\tau_e} \quad (\text{A.10})$$

$$\frac{\eta_2 I_2}{q} = 2\xi_2^S v_g^S \cdot \Gamma_2^S \cdot \frac{l_2}{L} N_{ph}^S \cdot g_2^S + 2\xi_2^L v_g^L \cdot \Gamma_2^L \cdot \frac{l_2}{L} N_{ph}^L \cdot g_2^L + \frac{N_2}{\tau_e} \quad (\text{A.11})$$

The rate equations for photons in the mode ‘‘S’’ and ‘‘L’’, respectively equations (4.3-4), are re-written using equation (4.5) and neglecting the contribution of the spontaneous emission in the mode of interest (the terms weighted by $\beta_{sp,i}^{S,L}$):

$$\left(\frac{2\xi_1^S v_g^S}{V_{ph,1}} N_{ph,1}^S g_1^S V_1 + \frac{2\xi_2^S v_g^S}{V_{ph,2}} N_{ph,2}^S g_2^S V_2 \right) - \frac{N_{ph}^S}{\tau_{ph}^S} = 0 \quad (\text{A.12})$$

$$\left(\frac{2\xi_1^L v_g^L}{V_{ph,1}} N_{ph,1}^L g_1^L V_1 + \frac{2\xi_2^L v_g^L}{V_{ph,2}} N_{ph,2}^L g_2^L V_2 \right) - \frac{N_{ph}^L}{\tau_{ph}^L} = 0 \quad (\text{A.13})$$

Introducing again explicitly the volume of the active region V_i and the volume of the optical mode $V_{ph,i}$ we get:

$$\left(2\xi_1^S v_g^S \cdot \Gamma_1^S \cdot \frac{l_1}{L} N_{ph}^S \cdot g_1^S + 2\xi_2^S v_g^S \cdot \Gamma_2^S \cdot \frac{l_2}{L} N_{ph}^S \cdot g_2^S \right) - \frac{N_{ph}^S}{\tau_{ph}^S} = 0 \quad (\text{A.14})$$

$$\left(2\xi_1^L v_g^L \cdot \Gamma_1^L \cdot \frac{l_1}{L} N_{ph}^L \cdot g_1^L + 2\xi_2^L v_g^L \cdot \Gamma_2^L \cdot \frac{l_2}{L} N_{ph}^L \cdot g_2^L \right) - \frac{N_{ph}^L}{\tau_{ph}^L} = 0 \quad (\text{A.15})$$

The rate-equations for carriers and photons (i.e. threshold equations for the two optical modes) are re-written in the compact form below:

$$\frac{\eta_1 I_1}{q} = 2\xi_1^S v_g^S \cdot \frac{l_1}{L} \cdot \Gamma_1^S N_{ph}^S \cdot g_1^S + 2\xi_1^L v_g^L \cdot \frac{l_1}{L} \cdot \Gamma_1^L N_{ph}^L \cdot g_1^L + \frac{N_1}{\tau_e} \quad (\text{A.16})$$

$$\frac{\eta_2 I_2}{q} = 2\xi_2^S v_g^S \cdot \frac{l_2}{L} \cdot \Gamma_2^S N_{ph}^S \cdot g_2^S + 2\xi_2^L v_g^L \cdot \frac{l_2}{L} \cdot \Gamma_2^L N_{ph}^L \cdot g_2^L + \frac{N_2}{\tau_e} \quad (\text{A.17})$$

$$N_{ph}^S \cdot \left(2\xi_1^S v_g^S \cdot \frac{l_1}{L} \cdot \Gamma_1^S \cdot g_1^S + 2\xi_2^S v_g^S \cdot \frac{l_2}{L} \cdot \Gamma_2^S \cdot g_2^S - \frac{1}{\tau_{ph}^S} \right) = 0 \quad (\text{A.18})$$

$$N_{ph}^L \cdot \left(2\xi_1^L v_g^L \cdot \frac{l_1}{L} \cdot \Gamma_1^L \cdot g_1^L + 2\xi_2^L v_g^L \cdot \frac{l_2}{L} \cdot \Gamma_2^L \cdot g_2^L - \frac{1}{\tau_{ph}^L} \right) = 0 \quad (\text{A.19})$$

Bibliography Appendix A

-
- [1] M. Brunner, K. Gulden, R. Hovel, M. Moser, J.-F. Carlin, R. P. Stanley, and M. Illegems, ‘‘Continuous-Wave Dual-Wavelength Lasing in a Two-Section Vertical-Cavity Laser’’, *IEEE Phot. Techn. Lett.*, **12**, pp. 1316-1318, 2000.

Appendix B

Quantum confined Stark effect

When semiconductors are fabricated in very thin layers (e.g., $\sim 100 \text{ \AA}$), the optical absorption spectrum changes radically as a result of the quantum confinement of the carriers in the resulting one-dimensional potential wells [1]. The confinement increases the binding energy of excitons. As a result, exceptionally clear exciton resonances at room temperature have been demonstrated in GaAs/AlGaAs QWs [2].

In GaAs/AlGaAs QW structures, Miller et al. observed large shifts in band-edge absorption for electric fields perpendicular to the layers [3]. The shifts can exceed the exciton binding energy and yet the exciton resonances remain well resolved. Extended room temperature measurements confirm the existence of exciton resonances up to 50 times the classical ionization field $E_i (=E_B/8ea$, where E_B is the zero field binding energy and a is the Bohr radius) which gives the order of magnitude of $\sim 10^5 \text{ V/cm}$. This effect has been named Quantum-Confined Stark Effect (QCSE) in analogy to the shift of energy levels in isolated atoms caused by electric field.

The mechanism of QCSE derives essentially from the quantum confinement in the thin semiconductor layers. Large effects are to be expected with moderate fields because the particle-in-a-box envelope functions and the exciton envelope functions are large ($\sim 100 \text{ \AA}$), have low associated energies ($\sim 10 \text{ meV}$), and hence are significantly perturbed by moderate fields (10 meV across 100 \AA corresponds to 10^4 V/cm).

Electrical fields perpendicular to the QW pull the electrons and holes towards opposite sides of the layers resulting in an overall net reduction in energy of an electron-hole pair and a corresponding Stark shift in the exciton absorption. The walls of the QW impede the electron and hole from tunneling out of the well in rapid field ionization. Because the well is narrow (e.g., $\sim 100 \text{ \AA}$) compared to the three dimensional exciton size (e.g., $\sim 300 \text{ \AA}$), the electron-hole interaction, although slightly weakened by the separation of electron and hole, is still strong, and well defined excitonic states can still exist. Thus exciton resonances can remain to much higher fields than would be possible in the absence of this confinement, and large absorption shifts can be seen without excessive broadening.

This effect whose mechanism was succinctly presented above has attracted a lot interest since more than 20 years from theoretical point of view [4,5], as well as a mean for a high speed optical modulation and switching [6]. QCSE has been theoretically considered in many works with different degrees of complexity. Here we implement the classical approach developed by Miller et al. [4,5,6], which although approximate gives a very good physical insight in the mechanism of electro-absorption. We consider variationally the effect of electrical field in a quantum well [7] assuming an infinitely deep QW with an effective width matched to give the proper confining energy levels [4].

The theory will be discussed within the effective-mass approximation. As we are considering the optical transition which creates an electron and a hole, the interaction between them should be included. The effective mass electron-hole Hamiltonian in the presence of electric fields can be written as:

$$H = H_{KEz_e} + V_e(z_e) - eF_{perp}z_e + H_{KEz_h} + V_h(z_h) + eF_{perp}z_h + H_{KEz_{rh}} + V_{e-h}(z_{e-h}) + e\vec{r} \cdot \vec{F}_{par} \quad (\text{B.1})$$

where we have the following:

(i) z_e and z_h are the coordinates perpendicular to the plane of the layer of electron and hole, respectively;

(ii) \vec{r} is the relative position of the electron and hole in the plane of the layer;

(iii) $H_{KEz_e} = \frac{-\hbar^2}{2m_{e,perp}^*} \cdot \frac{\partial^2}{\partial z_e^2}$; $H_{KEz_h} = \frac{-\hbar^2}{2m_{h,perp}^*} \cdot \frac{\partial^2}{\partial z_h^2}$ are the kinetic energy operators for

electron and hole, respectively, in the z direction (perpendicular to the layers) with $m_{e,perp}^*$ and $m_{h,perp}^*$ being the effective masses of electron and hole, respectively, in the z direction.

(iv) $V_e(z_e)$ and $V_h(z_h)$ are the built-in rectangular QW potentials for electron and hole.

(v) F_{perp} is the electric-field component perpendicular to the plane of the layers and F_{par} is the field in the plane of the layers.

(vi) $H_{KEz_{rh}} = \frac{-\hbar^2}{2\mu} \cdot \frac{\partial^2}{\partial r^2}$ is the kinetic energy operator of the relative motion of the electron

and hole with μ being the reduced effective mass in the plane of the layers.

(vii) $eV_{e-h}(z_{e-h}) = \frac{-e^2}{\epsilon \cdot (|z_e - z_h|^2 + r^2)^{1/2}}$ is the Coulomb potential energy of the electron-hole

interaction.

The experimental results show that a strong effect of the electric field perpendicular to the QW layers on the optical absorption near the band-gap is to shift the absorption to longer wavelengths (lower photon energies). Although there may be some broadening of the absorption, the peaks are resolvable up to $\approx 10^5$ V/cm.

Various parts of the Hamiltonian written above have already been treated separately. First we consider the zero-field parts. $H_{KEz_e} + eV_e(z_e)$ (and the equivalent for holes) is just the Hamiltonian of a particle in a one-dimensional rectangular potential well and the solutions for this are well-known.

Let us consider the effects of the electron-hole interaction described by $H_{KEr_{rh}} + eV_{e-h}(\vec{r}, z_e, z_h) + H_{KEz_e} + eV_e(z_e) + H_{KEz_h} + eV_h(z_h)$ which is the Hamiltonian of the electron-hole system with no field in a rectangular potential well. By solving for the eigenvalues of this Hamiltonian and subtracting the one-dimensional particle-in-a-box energies, the zero-field binding energy of the exciton can be calculated. Following the procedure of Miller et al. [4] we will attempt to evaluate all the terms in H simultaneously. There is one obvious physical effect that is contained in H : as the field is applied, electrons and holes move to the opposite sides of the QWs and as a consequence the Coulomb attraction between electron and hole is reduced, reducing the binding energy of the exciton and thereby acting to increase the energy of the exciton resonance. For a full solution we will use a variational method with a separable trial function:

$$\Psi(\vec{r}, z_e, z_h) = \psi_e(z_e) \cdot \psi_h(z_h) \cdot \phi_{e-h}(\vec{r}) \quad (\text{B.2})$$

where $\psi_e(z_e)$ and $\psi_h(z_h)$ are the “exact” wave functions of the individual electrons and holes in the one-dimensional QWs with an applied field, and:

$$\phi_{e-h}(\vec{r}) = \left(\frac{2}{\pi}\right)^{1/2} \cdot \frac{1}{\lambda} \cdot \exp\left(-\frac{r}{\lambda}\right) \quad (\text{B.3})$$

(i.e., we choose a simple 1S-like orbital for the in-plane radial motion) with λ , the amplitude radius of the exciton orbit, as an adjustable parameter. This wave function is probably about the simplest that can be chosen but it is not valid for a well comparable to or thicker than the three-dimensional exciton diameter (~ 300 Å) as it does not tend to the three-dimensional wave function in the limit. However it is a good approximation for the thin wells (~ 100 Å) used here.

The wave function for electrons and holes is given by [7]:

$$\psi(z) = N(\beta) \cdot \cos\left(\frac{\pi \cdot z}{L}\right) \cdot \exp\left[-\beta \cdot \left(\frac{z}{L} + \frac{1}{2}\right)\right], \quad \frac{|z|}{L} < \frac{1}{2} \quad (\text{B.4})$$

where β is a variational parameter, $N(\beta)$ a normalization constant, L is the width of the infinite QW. Solving the Hamiltonian of a one-particle system with the above mentioned wave function, one obtains the following expression for the energy whose value is to be minimized (different from the expression given in [7] as it proved to be wrong):

$$E(\beta) = E_1^{(0)} \cdot \left[1 + \frac{\beta^2}{\pi^2} + \varphi \cdot \left(\frac{1}{2 \cdot \beta} + \frac{\beta}{\pi^2 + \beta^2} - \frac{1}{2} \cdot \coth \beta \right) \right] \quad (\text{B.5})$$

where $E_1^{(0)}$ is the ground state energy at zero field, knowing that the spectrum of the Hamiltonian without the electric field is discrete and given by:

$$E_n^{(0)} = \frac{\hbar^2 \pi^2}{2 \cdot m^* \cdot L^2} \cdot n^2, n=1,2, \dots \quad (\text{B.6})$$

with m^* being the effective mass of the electron or hole. $\varphi = \frac{|e| \cdot F \cdot L}{E_1^{(0)}}$ is the dimensionless electrostatic energy. Minimizing $E(\beta)$ with respect to β one finds the parameter β to be used in the wave function, as a function of φ , i.e. as a function of the applied electric field.

Formally evaluating the expectation value of H one obtains:

$$\langle \Psi | H | \Psi \rangle = E_e + E_h + E_B \quad (\text{B.7})$$

where E_e and E_h are the energies of the individual electrons and holes already evaluated and E_B , which will refer to here as the exciton binding energy, is given by:

$$E_B = E_{KE_r} + E_{PE_r} \quad (\text{B.8})$$

where E_{KE_r} , the kinetic energy of the relative electron-hole motion in the layer plane is given by:

$$E_{KE_r} = \langle \phi_{e-h} | H_{KErh} | \phi_{e-h} \rangle = \frac{\hbar^2}{2 \cdot \mu \cdot \lambda^2} \quad (\text{B.9})$$

and E_{PE_r} , the Coulomb potential energy of the electron-hole relative motion, given by:

$$E_{PE_r} = \langle \Psi | V_{e-h} | \Psi \rangle \quad (\text{B.10})$$

E_{PE_r} is also dependent on the variational parameter λ . The evaluation of the integrals in the last expression is not straightforward. The fact that the variables in the wave function Ψ are separable is of less use here because the potential V_{e-h} couples all the variables. However it can be integrated partly analytically, partly numerically. Written explicitly the potential energy E_{PE_r} is:

$$E_{PE_r} = -\frac{2e^2}{\pi \epsilon \lambda^2} \cdot N^2(\beta_e) \cdot N^2(\beta_h) \cdot \int_{\theta=0}^{\pi} \int_{r=0}^{\infty} \int_{z_e=-L_e/2}^{+L_e/2} \int_{z_h=-L_h/2}^{L_h/2} \cos^2\left(\frac{\pi \cdot z_e}{L_e}\right) \cdot \exp\left[-2\beta_e \cdot \left(\frac{z_e}{L_e} + \frac{1}{2}\right)\right] \times \\ \times \cos^2\left(\frac{\pi \cdot z_h}{L_h}\right) \cdot \exp\left[-2\beta_h \cdot \left(\frac{z_h}{L_h} + \frac{1}{2}\right)\right] \times \frac{r \cdot \exp(-2r/\lambda)}{[(z_e - z_h)^2 + r^2]^{1/2}} \cdot d\theta \cdot dr \cdot dz_e \cdot dz_h \quad (\text{B.11})$$

where we have used the variational wave functions for electron and hole as discussed before because they are analytically simple and give the correct energies for electron and hole states provided we use the effective-well widths (L_e and L_h) appropriate for the wells. The normalization factors for the electron and hole wave functions are:

$$N^2(\beta) = \frac{4\beta}{L \cdot [1 - \exp(-2\beta)]} \cdot \frac{\beta^2 + \pi^2}{\pi^2} \quad (\text{B.12})$$

where L is the appropriate effective-well width.

The integral over θ above is trivial and the integral over r can be performed, yielding:

$$G(\gamma) \equiv \frac{2}{\lambda} \cdot \int_{r=0}^{\infty} \frac{r \cdot \exp(-2r/\lambda) \cdot dr}{\sqrt{\gamma^2 + r^2}} = \frac{2 \cdot |\gamma|}{\lambda} \cdot \left\{ \frac{\pi}{2} \left[H_1\left(\frac{2 \cdot |\gamma|}{\lambda}\right) - N_1\left(\frac{2 \cdot |\gamma|}{\lambda}\right) \right] - 1 \right\} \quad (\text{B.13})$$

where $H_1(u)$ is the first order Struve function and N_1 is the first order Neumann function or Bessel function of the second kind. The final result for E_{PE_r} is evaluated by numerical double integration over z_e and z_h for given β_e and β_h .

The above result for E_{PE_r} together with the value for E_{KE_r} gives the exciton binding energy E_B which is to be minimized with respect to λ .

To resume, our procedure for calculating the binding energy for a given field was first to deduce β_e and β_h for that field from a separate variational calculation then to evaluate E_{PE_r} and E_{KE_r} , adjusting λ variationally to minimize E_B . The value of the binding energy is used to calculate the excitonic contribution of the absorption coefficient. According to Ahn (Ref. [9]), the exciton absorption coefficient can be written as:

$$\alpha^{ex}(\omega) = \frac{\omega \cdot \mu \cdot c}{n_r} \cdot M^2 \cdot N_{ex} \cdot \frac{\frac{\hbar}{\tau_x}}{(E_B + E_G - \hbar\omega)^2 + \left(\frac{\hbar}{\tau_x}\right)^2} \quad (\text{B.14})$$

where N_{ex} is the exciton density, τ_x is the relaxation time for the exciton, and E_B is the exciton binding energy, μ is the permeability, n_r the refractive index, c the speed of light in the free space and M^2 is the matrix element for the electronic transition being considered.

The total absorption coefficient is given by the interband optical absorption coefficient $\alpha(\omega)$ as defined for instance in Ref. [8] added to the absorption due to the exciton [9] calculated as shown above.

The quantum confined Stark effect consists of two components: one is the red-shift of the absorption band-edge with the applied electrical field and the second is the apparition of the excitonic peaks in the absorption spectrum and their evolution (red-shift and broadening) with the applied electrical field. To illustrate the first effect, we present the Figure B.1 which clearly shows the shift in the absorption coefficient (without taking into account the exciton) for different strengths of the applied electric fields.

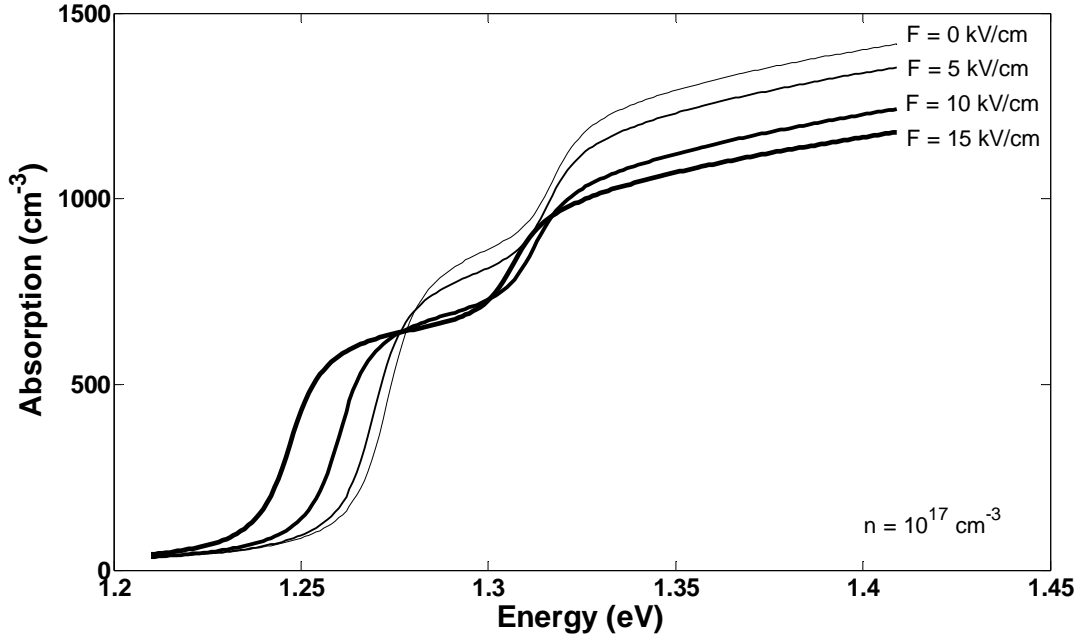


Figure B.1: Red-shift of the absorption band-edge for different reverse electric fields

In order to make our approach consistent with the discussion in the previous Chapter 4, we approximate the so calculated absorption in the InGaAs QWs using expressions like equations (4.17)-(4.20). In Figure B.2 the plain curves represent the dependence of the absorption coefficient with the carrier density calculated according to the description above. The dashed curves represent the fit with expressions like equations (4.17)-(4.20). In this discussion we considered only the band edge shift due to the QCSE, and not the excitonic effects. The constants in the logarithmic absorption dependence are now dependent on the strength of the electric field. The following linear dependence is obtained for In_{0.2}Ga_{0.8}As QW with a thickness of 11 nm:

$$N_{tr}^S = (1.566 + 0.0178 \cdot F) \cdot 10^{18} \quad (\text{B.15})$$

$$G_0^S = 1900 - 20 \cdot F \quad (\text{B.16})$$

$$N_{tr}^L = (1.566 + 0.0146 \cdot F) \cdot 10^{18} \quad (\text{B.17})$$

$$G_0^L = 1500 - 30 \cdot F \quad (\text{B.18})$$

with $N_0^S = 10^{17}$ and $N_0^L = 10^{16}$, respectively. Exciton effects are not included when making this approximation. In Figure B.2 we justify the logarithmic approximation we made by plotting the variationally calculated dependence of the QW absorption/gain on the carrier density for two values of the electric field of $F=0$ and 10 kV/cm, as well as the ones calculated according to equations (4.17)-(4.20) and (37)-(40). Making such an approximation, i.e. a linear dependence of the coefficients in the logarithmic dependence of the absorption and gain in a single QW on the reverse bias, helps us to implement in a straightforward way the reverse bias conditions into our rate equation model for CC-VCSEL. In Figure 5.26 we present the calculated in such a way the output power in the short-

wavelength mode (only this mode is lasing at the conditions of Figure 5.26) as a function of the top (short) cavity injection current and for different reverse bias in the bottom (long) cavity: $F=0$, $F=10$ and $F=20$ kV/cm and for $I_2=0$ mA. As it can be seen from this figure, increasing the reverse bias leads to decreasing the number of photons and the slope of the LI curves in the conditions of open circuit ($I_2=0$) for the bottom cavity.

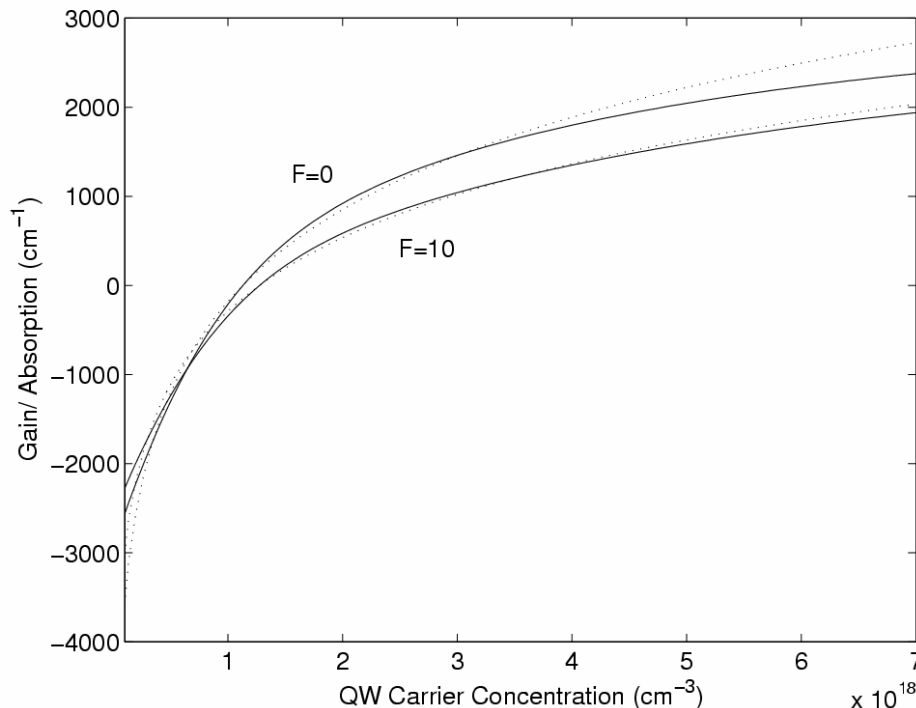


Figure B.2: Optical Absorption/Gain of 11nm thick $\text{In}_{0.2}\text{Ga}_{0.8}\text{As}$ QW as a function of the carrier density for two values of the QW electric field: $F=0$ and $F=10$ kV/cm. The dashed curves are analytical logarithmic gain dependences with parameters specified in the text.

Bibliography Appendix B

- [1] R. Dingle, W. Wiegmann, and C.H. Henry, *Phys. Rev. Lett.*, **33**, 827 (1974).
- [2] D.A.B. Miller, D.S. Chemla, D.J. Eilenberger, P.W. Smith, A.C. Gossard, and W.T. Tsang, *Appl. Phys. Lett.*, **41**, 679 (1982).
- [3] T.H. Hood, C.A. Burrus, D.A.B. Miller, D.S. Chemla, T.C. Damen, A.C. Gossard, and W. Wiegmann, *Appl. Phys. Lett.*, **44**, 16 (1984).
- [4] D.A.B. Miller, D.S. Chemla, T.C. Damen, A.G. Gossard, W. Wiegmann, T.H. Wood, C.A. Burrus, "Electric field dependence of optical absorption near the band gap of quantum well structures", *Phys. Rev. B*, **32**, pp. 1043-1060 (1985).
- [5] D.S. Chemla, D.A. Miller, P.W. Smith, A.G. Gossard, W. Wiegmann, "Room temperature Excitonic Nonlinear Absorption and Refraction in GaAs/AlGaAs Multiple Quantum Well Structures", *IEEE J. Quant. Electr.*, **20**, pp. 265-275 (1984).
- [6] D.A. Miller, D.S. Chemla, T.C. Damen, T.H. Wood, C.A. Burrus, A.G. Gossard, W. Wiegmann, "The Quantum Well Self-electrooptic Effect Devices: Optoelectronic Bistability and Oscillations, and Self-Linearized Modulation", *IEEE J. Quant. Electr.*, **21**, pp. 1462-1476 (1985).

- [7] G. Bastard, E.E. Mendez, L.L. Chang, L. Esaki, "Variational calculations on a quantum well in an electric field", *Phys. Rev. B*, **28**, pp. 3241-3245 (1983).
- [8] D. Ahn and S.L. Chuang, "Calculation of linear and non-linear intersubband optical absorptions in a quantum well model with an applied electric field", *IEEE J. Quantum Electron.*, **23**, pp. 2196-2204 (1987).
- [9] D. Ahn, "Enhancement of the Stark Effect in Coupled Quantum Wells for Optical Switching Devices", *IEEE J. Quantum Electron.*, **25**, pp. 2260-2265 (1989).

Acknowledgements

I would like to thank my advisor, Prof. Marc Ilegems, for the great opportunity he offered me 4 years ago, to pursue my PhD studies under his guidance in the IMO/IPEQ at EPFL. Marc's knowledge and support as well as the open door I found whenever I needed were invaluable at all stages of my PhD. His intuition and vision put my efforts on the right track when I was a freshman, and the incredibly broad knowledge that he shares, along with his advice, have led my steps all the way to the completion of this thesis.

My gratitude goes also to Jean-François Carlin whose help was essential during the thesis. I thank him for having started working with me on this very exciting and original doctoral project, for the deep understanding in the field and the extraordinary experience that he shared with me both in the lab and in the clean-room. And even if it is quite often that one can hear him in the lab "*ZUT, ça marche PAS!*", I can certainly say that, finally, it works!

My gratitude to Prof. Krassimir Panajotov for the continuous, intense collaboration we have had, for his precious help during the thesis, for making light in some places in the field that were, up to a certain moment, quite "dark" for me. I also wish to thank Krassimir for warmly integrating me in his group at Vrije Universiteit Brussels during my visits there. I would like to thank Prof. Irina Veretennicoff and Prof. Hugo Thienpont from VUB for the warm welcome each time I was there, and Guy Verschaffelt and Jan Danckaert for the good collaboration we had.

I wish to thank all the people that helped me during this thesis. To Ross Stanley for sharing with me his previous experience with CC-VCSELs, to Christoph Zellweger that helped me with the first steps in the IMO/IPEQ clean-room, to Nicolas Leiser for his continuous, highly professional care that he takes so that everything in the clean-room works at its best, to Alexei Syrbu, Reto Joray and Hans-Jörg Bühlmann for many fruitful suggestions, to Roger Rochat for the fact that each time "I went to him with a problem, I left with a solution".

I was lucky to have all the colleagues I had, to share all the sunny or cloudy days of these 4 years with Reto, Christoph (I still "see" his figure just in front of me in our office), Julien, David, Barbara, Volker, Alexander, Benoit, Romuald, Rolando, Andrea, Jerome, Denis. Special thanks for

my temporary colleagues in Brussels: Andrzej Tabaka and Tomasz Nasilowski (who kindly shared their office with me), Mikel Arizaleta, Miren Camarena, Marc Sciamanna.

I will never forget these years also owing to all the other friends I have here, sharing the same skiing slopes in the winter, the same boat, the same swimming pool or the same beach-volley field in the summer, sometimes the same bottle of wine ☺ during the “bridge-evenings”. My thoughts go to Nicu, Ion, Costin, Raul and Melanie, Nicoleta, Cristina and Vlad, Diana, Emi, Simona and Dani, Cristi, Nicoleta and Adi, Carla and Radu, Oana, Dan, and Razvan.

I am grateful to my wife, Ilinca, for warmly supporting me continuously, all the time and especially during these 4 years.

My deepest gratitude for my family and most of all to my parents for their never-ending love and support during these ... 29 years now!

Professional address: EPFL-FSB-IPEQ
CE (Ecublens) CH-1015
Lausanne, Switzerland

Mobile: +41-(0)76.423.71.24
Phone (professional): +41-(0)21-693.45.30
Fax (professional): +41-(0)21-693.43.43
E-mail: vlad.badilita@epfl.ch

Vlad Bădilită

Personal data:

- Date of birth: 29.05.1975.
- Place of birth: Iasi, Romania.
- Civil status: married.

Education:

- **Sept. 2000 – December 2004:** PhD student, Institute of Quantum Electronics and Photonics, Swiss Federal Institute of Technology (EPFL – IPEQ), Lausanne, Switzerland (<http://imowww.epfl.ch>);
- **Oct. 1997 – March 1999:** Post-grad. studies in Solid State Physics, Univ. of Bucharest – GPA: 10.00 out of 10.00;
- **Oct. 1993 – Sept. 1997:** Dipl. Physicist, Solid State Physics Dept., Univ. of Bucharest – GPA: 9.66 out of 10.00.

Internships:

- **Nov. 2001:** Vrije Universiteit Brussel, Department of Applied Physics and Photonics (<http://www.alna.vub.ac.be>), within VISTA European Project;
- **Nov. – Dec. 1999:** Ångström Lab., Dept. of Material Sciences, Uppsala Univ. (Sweden) (<http://www.angstrom.uu.se/research.html>), within MEMSWAVE European Project;
- **Oct. – Nov. 1999:** Consiglio Nazionale delle Ricerche – Microwave Microsystems Technology Lab. (CNR – M²T) (<http://m2t.psm.rm.cnr.it>) and Tor Vergata Univ. Rome, within MEMSWAVE European Project;
- **Dec. 1998:** Research Institute for Technical Physics and Material Science, Hungarian Academy of Sciences (HAS) Budapest (www.kfki.hu/mfahp), within an interacademic bilateral cooperation.

Work experience:

- **Sept. 2000 – present:** researcher, teaching assistant at Institute of Quantum Electronics and Photonics in EPFL;
- **Dec. 1997 – Sept. 2000:** research assistant in Laboratory for Micromachined Structures, Microwave Devices and Circuits, National Institute for R&D in Microtechnologies (IMT – Bucharest), Romania (www.imt.ro).

Research experience and projects:

- **VISTA European Project “VCSELs for Information Society Technology Applications”** (<http://www.physics.ucc.ie/vista2/intro.html>):
 - Design and modelling of coupled-cavity VCSELs: dual-wavelength output, stochastic resonance in polarization behaviour;
 - Growth and processing;
 - Investigation on coupled-cavity VCSELs: polarization instabilities and control, pattern complexity, modulation and feedback effects;
- **MEMSWAVE European Project No. 977131 “Micromachined Circuits for Microwave and Millimeter-Wave Applications” - IMT Bucharest coordinator:**
 - Design, modelling, processing and characterisation of micromachined microwave circuits: microwave elements for 38 and 77 GHz: S- and meander-inductors, interdigitated capacitors, filters and antennas on thin semiconductor (SiO₂/Si₃N₄/SiO₂ – 10µm) and dielectric (GaAs/AlGaAs – 1.5µm) membranes;
- **“Development of Micromachined Structures on Si and GaAs for Sensors and Microwave Applications”** – intergovernmental bilateral cooperation between IMT Bucharest and CNR-M²T Rome:
 - thin (10µm) dielectric (SiO₂/Si₃N₄/SiO₂) membranes manufacturing on high resistivity <100> Si substrate as support for microwave elements to decrease losses and improve resonance frequencies;
 - design and processing of micromachined microwave elements: S- and meander-inductors, interdigitated capacitors, filters.
- **“Micromachined Structures on A_{III}-B_V Semiconductor Compounds for High Temperature Sensor Applications”** – intergovernmental bilateral cooperation between IMT Bucharest and FORTH-IESL Heraklion, Greece (<http://www.iesl.forth.gr>):
 - design and processing of micromachined pressure sensors on heteroepitaxial structures obtained by selective and non-selective etching techniques.
- **“Microwave Circuits and Devices on A_{III}-B_V Semiconductor Compounds”**, interacademic bilateral cooperation between Romanian Academy (IMT Bucharest) and Hungarian Academy of Sciences (HAS).
- Diploma thesis: **“Structural characterization of Al_{85-x}Si₁₅RE_x metastable alloys”**
 - Structural characterisation of rapidly solidified Al-based alloys by means of X-ray diffraction (XRD) and differential thermal analysis (DTA).

Publications:

- **V. Badilita**, J.-F. Carlin, and M. Ilegems, “Lumped-mirror model for CC-VCSELs”, submitted for IEEE Journal of Lightwave Technology.
- **V. Badilita**, J.-F. Carlin, K. Panajotov, and M. Ilegems, “Rate-Equation Model for Coupled-Cavity Surface-Emitting Laser”, accepted for publication in IEEE Journal of Quantum Electronics;
- K. Panajotov, **V. Badilita**, J.-F. Carlin, H. Thienpont, and I. Veretennicoff, “Quantum Confined Stark Effect in Coupled – Cavity VCSEL”, presented at SPIE “Photonics Europe”, April 2004, Strasbourg, France.
- **V. Badilita**, J.-F. Carlin, M. Ilegems, M. Brunner, K. Panajotov, G. Verschaffelt, “Control of polarization switching in vertical coupled-cavities surface emitting lasers”, IEEE Photonics Technology Letters, vol. 16 (2), pp. 365-367 (2003);
- **V. Badilita**, J.-F. Carlin, M. Ilegems, M. Brunner, G. Verschaffelt, K. Panajotov, “Investigation of polarization behaviour in a vertical coupled-cavities surface-emitting laser”, presented at SPIE “Photonics Fabrication Europe” 28 Oct. – 1 Nov. 2002, Brugge, Belgium, published in *Proc. SPIE*, vol. 4942, pp. 363 (2002);
- **V. Badilita**, J.-F. Carlin, M. Brunner, M. Ilegems, “Light-current characterization of dual-wavelength VCSELs”, presented at SPIE “Photonics West”, Febr. 2002, San Jose, CA, USA, published in *Proc. of SPIE*, vol. 4649, pp. 87-95 (2002);
- A. Muller, S. Iordanescu et al., **V. Badilita**, “Polyimide Based GaAs Micromachined Millimeter Wave Structures”, paper presented at Micromechanics Europe MME '99, Sept. 27-28, Gif-sur-Yvette, France;
- A. Muller, S. Iordanescu et al., **V. Badilita**, “Polyimide Based GaAs Micromachined Millimeter Wave Structures”, Journal of Micromechanics and Microengineering, 10 (2000), pp. 130-135;
- A. Müller, I. Petrini, V. Avramescu, S. Iordanescu, D. Vasilache, G. Simion, N. Nitescu, **V. Badilita**, D. Dascalu, G. Konstantinidis, R. Marcelli, G. Bartolucci, “Polyimide membranes as support for microwave circuit elements and pressure sensing”, MRS'99, Boston, SUA;
- Viorel Badilita, **Vlad Badilita**, “Structure and Thermal Stability of Rapidly Solidified Al-RE-Si Alloys” –, accepted paper for the 2nd Turkish National Powder Metallurgy Conference, Ankara, Sept. 1999;
- **V. Badilita**, D. Vasilache, G. Simion, N. Nitescu, “Polyimide Based 3D Flexible Microstructures for Microwave and Sensing Applications” – MEMSWAVE Workshop, Oct. 1999, Sinaia, Romania (CAS'99);
- G. Simion, N. Nitescu, **V. Badilita**, D. Vasilache, A. Ion – “Non-silicon Materials for Micromachined Pressure Sensing Structures”, presented at MEMSWAVE WORKSHOP, oct.1999, Sinaia, Romania;
- A. Muller, I. Petrini et al., **V. Badilita**, “Dielectric Membranes Manufactured by Isotropic Etching of <111> Oriented Silicon for Microwave Applications”, Proc. of CAS'98, vol. 2, pp. 341–344;
- Post-graduate dissertation (1999): “Three-dimensional structures obtained by means of Si micromachining;
- Diploma thesis (1997): “Structural characterization of $Al_{85-x}Si_{15}RE_x$ metastable alloys”;

Computer knowledge:

- OS: MS Windows, Mac OS;
- LabView; Microwave Office;
- Matlab, Mathematica;
- Latex, MS Office.

Foreign languages:

- English, French – fluent;
- German – conversational level;
- Russian – basic knowledge;
- Romanian – native language.

Other skills:

- B-class driving licence.